Effects of Sand Ingestion on the Film-Cooling of Turbine Blades

William Scott Walsh

Thesis submitted to the Faculty of the
Virginia Polytechnic Institute and State University
in partial fulfillment of the requirements for the degree of

Master of Science
in
Mechanical Engineering

Dr. K. A. Thole, Chair
Dr. W.F. O'Brien
Dr. W. F. Ng

September 6, 2005
Blacksburg, VA

Keywords: sand ingestion, gas turbine,
film-cooling

Effects of Sand Ingestion on Film-Cooling of Turbine Blades

William Scott Walsh

Abstract

Gas turbine engines for propulsion operate under harsh conditions including gas temperatures that exceed the melting point of the metal, high mechanical stresses, and particulate ingestion such as sand. To maintain a low and uniform metal temperature to extend the life of a turbine component, a complex scheme of internal convective cooling and external film-cooling is required. Gas turbine engines operated in sandy or dusty environments can ingest a large quantity of sand into the mainstream and, more importantly, into the cooling system. Sand ingested into the coolant system has the potential to reduce or block off the flow intended to cool the turbine blades or vanes. If the source of coolant air to a critical region of a turbine blade were partially blocked, it would result in a substantial reduction in component life.

This study includes establishing a methodology for testing sand ingestion characteristics on a simulated turbine component with film-cooling holes at room temperature and engine temperatures. The study evaluates a simple array of laser drilled film-cooling holes, similar to a showerhead on the leading edge of an airfoil. The blocking characteristics of this design indicate that increasing the airflow or decreasing the sand amount results in a decreased blockage. It was also determined that as the metal temperature increases, the blockage from a given amount of sand increases.

The methodology used in the primary portion of this thesis was modified to test sand ingestion characteristics on actual turbine blades with film-cooling holes at room temperature and engine temperatures. The study evaluated the blockage performance of several different turbine blades including the F-100-229-full, F-100-229-TE, and the F-119 with a new trailing edge cooling methodology know as a microcircuit. It was shown that increasing the airflow or pressure ratio, or decreasing the sand amount would result in decreased blockage. It was also shown that over a certain metal and coolant temperature, the blockage is significantly worsened. However, it was also shown on the F-119 turbine blade that below a given metal temperature, there is no impact of metal or coolant temperature on sand blockage.

Preface

Gas turbine engines for propulsion are susceptible to sand ingestion during take-off and landing conditions. This sand ingestion can cause blockages in the cooling passages of a turbine blade or vane. At this time, there are no other studies on the exact characteristics of sand blockage in the coolant path. To account for sand ingestion in present turbine blade cooling designs, data from field operated blades or whole engine tests were used in this study. The field operated blades have been subjected to sand ingestion, however, the exact operating conditions at the time of the ingestion are unknown. Entire engine tests are conducted on a test stand and are very expensive. In addition, it is difficult to isolate the mechanisms and characteristics of sand blocking during these whole engine tests because there are so many variables involved.

The first section of this thesis is a paper that discusses the factors and characteristics of sand blocking in a simple array of laser drilled film-cooling holes in a test coupon. This first section covers the methodology and parameters necessary to describe and quantify the results of sand ingestion. The first section also presents the results of testing a simple coupon at room temperature and at engine temperatures.

The second section of this thesis is a final report to the sponsor of this work, Pratt & Whitney. The second section covers the methodology and parameters necessary to quantify sand blockage in actual turbine airfoils. The second section also presents the results from testing three actual turbine blades. The blades tested included the F-100-229-full blade, the F-100-229-TE blade, and the F-119 blade with a trailing edge microcircuit, which is a new cooling design. This section also compared the sand blocking characteristics of the F-100-229-TE blade to the F-119 blade so that the blocking of the F-119 in field operation could be estimated.

Table of Contents

List of Tables

List of Figures

Part I. Public Coupon Results:

Blockage from Sand Ingestion in a Public Coupon with Film-Cooling Holes*

ABSTRACT

Gas turbine engines are often times subjected to conditions where dirt and sand are ingested into the engine during takeoffs and landings. Given that only a small number of aero engines have filters or particle separaters, particulate ingestion can be present in both the main gas path and coolant streams. Particulates can block coolant passages and film-cooling holes that can lead to increased airfoil temperatures by reducing the coolant available at a given pressure ratio.

This study investigated the effects of sand blockage on film-cooling holes for a leading edge coupon. The coupon was tested to determine the reduction in flow parameter for a range of pressure ratios, coolant temperatures, metal temperatures, number of cooling holes, sand amounts, and sand diameters.

* To be submitted to the IGTI conference 2006

Co-Authors: Dr. Karen A. Thole, Mechanical Engineering Department , Virginia Tech
Chris Joe, Turbine Durability, Pratt & Whitney

INTRODUCTION

Turbine engines for propulsion operate in a variety of environments that can affect their performance and life of their components. One specific environment of interest is where ingestion of small particles, particularly sand, takes place. While large particles can cause catastrophic damage, small particles of dust and sand in the air can also effect engine performance and service life. During takeoff, the engine is operating at high temperatures as well as at high airflows to the compressor. The high airflows cause an unsteady vortex that forms in front of the nacelle and, if the environment is such, it will entrain small particles of sand into the compressor inlet as shown in a numerical simulation by Moroianu et al. [1]. This vortex is visible in Figure 1.1, where large quantities of sand are being ingested into the engines of a C-17 during takeoff. Typically, gas turbines will receive very short bursts of sand at high concentration levels during takeoff and landing, and will then operate for long periods with almost no particulates being ingested while the aircraft is at cruise altitude.

Under harsh and dusty conditions, the sand-air mixture enters the compressor at moderate concentrations. The air flows through the compressor and increases in density, and because the sand is incompressible, the volume ratio of sand to air increases as a function of air density ratio, as discussed by Kim et al. [2]. In different locations within the compressor, air is bled through the combustor bypass to provide cooling for turbine parts. Some particles, particularly the small ones, will be diverted through the combustor bypass as observed in engine sand tests conducted by Dunn et al. [3]. During the travel through the compressor and combustor bypass, the sand affects many surfaces and can break up into many small particles, as shown by Schneider et al. [4] and also by Batcho et al. [5]. The combustor bypass air feeds coolant to blades and vanes that are in the turbine. This cooling air helps protect engine parts that are subjected to gas temperatures that exceed the melting point of the material. The bleed air is fed to inside passages of vanes and blades for convective cooling, and is then directed through holes in the airfoil surfaces for film-cooling. The design of modern gas turbine engines requires the combination of both internal convection and external film-cooling to ensure adequate part life.

To design an engine with reasonable maintenance intervals, high performance, and high efficiency, it is necessary to optimize the amount of combustor bypass air used for coolant. The more coolant air bled from the compressor, the less efficient an engine is because that air is not producing useful work. If too little air is bled from the compressor for cooling, the metal temperature will be much hotter and components will have a diminished service life. As such, there is a certain range of coolant air that is optimal for a given engine design. If the coolant is reduced below the optimum levels because of blocked film-cooling holes, the engine service life and performance could be adversely affected.

Sand blocking in gas turbine engines is a problem that continues to worsen as more particles are ingested. Particle temperatures increase rapidly, primarily due to radiation from the hot passage surfaces of a vane or blade. The extreme temperature of the metal in the blade can cause melting of the sand particles and increase the probability of the particles to adhere to the coolant passages. When sand blocks a coolant passage or coolant hole it reduces the coolant flow and creates a localized hot region in the blade. The sand on the surface of the coolant passage also acts as an insulating material reducing the heat transfer to the inside the blade thereby further increasing part temperature. The increase in coolant temperature and metal temperature can cause incoming sand to melt and increase the deposition rates. The combination of reduced convection, increased thermal resistance, and decreased mass flow will cause the metal temperature to increase and can result in a reduction in service life similar to that found by Kim et al. [2] from volcanic ash ingestion. Sand ingestion also causes erosion that can result in lower adiabatic efficiency. A study on sand ingestion in an axial fan by Ghenaiet et al. [6] indicated that after a 6 hour sand ingestion test, there was a 7% reduction in adiabatic efficiency.

This paper provides a methodology and test results conducted on a simple test coupon representative of an airfoil leading edge, which is one of the most difficult areas to cool and one of the most susceptible areas to sand blockage as shown in studies on external deposition tests by Tabakoff et al. [7] and Kim et al. [2]. The test coupon contains an array of film-cooling holes with a typical diameter and orientation as seen in a turbine vane leading edge. The coupon was tested for a number of different conditions

by varying the number of coolant holes, the sand amount and character, pressure ratio, coolant temperature, and metal temperature.

NOMENCLATURE

%RFP	percent reduction in flow parameter
D	cooling hole diameter
f	friction factor
FP	flow parameter
k	minor loss coefficient
L	cooling hole length
$\dot{m}$	mass flow
P	pressure
PR	pressure ratio
R	gas constant for air
SCMM	standard cubic meters per minute
T	temperature
V	average cooling hole velocity

Greek

Φ	effectiveness
ρ	coolant density

Subscripts

0C	total property of the coolant
∞	freestream conditions
CC	cold test – cold baseline
HH	hot test – hot baseline
HC	hot test – cold baseline

PAST RELEVANT STUDIES

There have been numerous studies by Schneider et al. [4, 8, 9, 10] and Ghenaiet et al. [6] that show methods of particle separation in combustor bypass air. To the authors' knowledge, however, propulsive turbines do not generally have filtering systems due to many constraints. The separation technology reported by Schneider et al. would reduce the accumulation of large sand particles; however, the small sand particles of interest would be difficult for a momentum separator to remove from the flow. Moreover, filters capable of filtering out this range of particles are generally too heavy to implement in propulsive applications with the added problem of increased pressure losses. With these restrictions on propulsion engines, another method of preventing or dealing with ingestion must be found.

The mechanisms of particle transport and deposition are important to understand so that the relevant conditions can be matched in an experimental environment. In an engine, the friction drag from the high-speed coolant keeps sand particles in an aerosol state. The particles move at nearly the same velocity as the air through the coolant system; however, given their mass they have a higher momentum. This higher momentum causes the particles to not follow the streamlines through turns or bends such as pin fins, ribs, 180° bends and even film cooling holes. Rather than follow the streamlines, particles impact the surfaces. After a particle impacts a surface, there are several forces that will dictate whether the particle will adhere to the surface. The restitution force is generated by the slight deflections in the surfaces of the particle and of the wall at impact. The magnitude of the restitution force is dependent on the coefficient of restitution and impact angle. The higher the velocity and the more normal the particle impacts the surface, the higher the rebound force. The thermophoresis force is generated by the difference in molecular motion in areas of high temperature gradients, as discussed by Friedlander [11]. Thermophoresis causes a force to shift the particles away from areas of high molecular motion, or hot regions. In a film-cooling hole, thermophoresis will force the particle away from the hot wall. The London-van der Waals force is an attractive force generated by atomic dipoles that acts over very short distances. London-van der Waals forces are attractive between the wall and the particle. If the restitution force and the thermophoratic force are higher than the London-van der Waals force, the

particle will rebound. If not, the particle will adhere to the surface. In addition to these forces, surface roughness can enhance the adhesion of small particles.

The combination of extreme temperature and residence time can lead to particle melting inside the turbine component. The residence time for a particle increases every time the particle impacts the wall. Schneider et al. [4, 8, 9, 10] has shown that in areas of relatively high turning particles may have residence times much longer than if the particles had followed the flow streamlines. If a particle's residence time is high enough, simple calculations, similar to those shown by Kim et al. [2] show that the particle temperature rapidly increases. As discussed by Friedlander [11], the melting point can significantly decrease as the grain size decreases. This is similar to the lower than expected melting points of volcanic ash found by Kim et al. [2]. If the particles are melted, the restitution force is drastically reduced, and the particle will most likely adhere to the surface.

When particles adhere to a surface, a chain reaction is started that could have severe effects. When a particle adheres to a surface, it increases the metal temperature by reducing the coolant flow, and increases the thermal resistance between the wall and the coolant air, as discussed by Kim et al. [2]. The higher metal temperature may melt a particle already adhered to the wall, and increase the likelihood that another particle will adhere to the same location due to the increased tackiness of the surface. Studies by Kim et al. [2] indicate that increased metal temperature significantly enhanced deposition rates. Subsequent particle adhesion will only serve to further increase the metal temperature and the likelihood that more particles will attach. Wenglarz et al. [12] and Kim et al. [2] have shown that after the metal temperature reaches a certain value, the adhesion characteristics are very nonlinear and adhesion rates increase rapidly. The increase in adhesion after a threshold temperature is consistent despite the fact that Wenglarz et al. [12] used coal fuel ash and Kim et al. used combinations of volcanic ash and glass. This dramatic increase in adhesion can potentially expand throughout the whole part if there is enough sand in the air to promote such a chain reaction.

With increasing temperatures of gas turbine engines and the development of new cooling designs, it is critical to evaluate the effects of sand particles ingested into the internal cooling passages. The reduction of flow to the coolant passages and film-cooling

holes can quickly cause part temperatures to increase, significantly reducing part life. In addition, the engines are most susceptible to sand ingestion during critical times, such as takeoffs and landings. Given this information, it is necessary to identify and quantify the parameters that most affect sand deposition.

EXPERIMENTAL FACILITY AND METHODOLOGY

There are many different ways to characterize sand blockage in a film-cooling hole. One possibility is to physically locate and characterize the dimensions of the blockage. This method would give good insight to the particular flow characteristics that deposit the particles; however, given the size and geometry of most film-cooling holes this would be a difficult measurement to make. Another method might be to use an overall heat transfer coefficient for the part and directly determine the effect of the blockage on heat transfer. The gas turbine industry generally uses a term called flow parameter (FP) for overall estimates of coolant flow supplied to a particular airfoil. The flow parameter, shown in equation 1.1, is a non-dimensional term that is the ratio of momentum force to pressure force, as discussed by Hill et al. [13].

$$FP = \frac{\dot{m}\sqrt{T_C R}}{P_{oC} D^2} = f(P_{oC} / P_\infty, \text{geometry}, T_{oc}) \tag{1.1}$$

When the flow parameter and temperatures are matched to realistic engine conditions, the residence time of the air in a component will match the residence time in the airfoil component during operating conditions. This is true even if the overall pressure ratio is not matched, as discussed by Kim et al. [2]. For a particular airfoil operating at a given coolant temperature, there is a distinctive relationship between the flow parameter and pressure ratio. This flow parameter will only vary if the coolant temperature and, hence, viscosity significantly changes or if the geometry is significantly changed, as in the case with sand blockage in a film-cooling hole. The flow parameter given in our paper was calculated with the total measured coolant mass flow divided by the total number of cooling holes, coolant pressure and temperature, as well as the diameter of the cooling hole.

Testing Coupon and Apparatus

The test coupon was designed to replicate characteristics of the leading edge of a typical turbine vane. Two coupons were manufactured with identical geometries except for the number of holes so that direct comparisons could be made. The holes were manufactured for the coupon using laser drilling. The 60-hole coupon was designed so that with a given range of pressure ratios, the metal and coolant temperatures could be matched to those found in actual engines. The coolant holes had a 90° compound angle opposing the direction of the internal flow inlet, and were all through the centerline axis of the coupon tube as shown in Figure 1.2. The coupons were made from Inconel 625, which has similar characteristics as airfoil metals used in industry.

The test rig consisted of five main components including the coolant supply, sand delivery, kiln, double-pass heat exchanger, and the instrumentation as shown in Figure 1.3 and 1.4. The coolant was supplied to the coupon by a compressed air supply that was provided by the Virginia Tech Physical Plant. A precision pressure-regulating valve with a sensitivity of 34 Pa and a maximum flow rate of 0.28 SCMM (standard cubic meters per min) was used to insure a controlled constant coolant pressure. Downstream of the pressure regulator, the coolant entered a laminar flow element to measure the coolant mass flow supplied to the coupon. The laminar flow element had a maximum flow rate of 1.1 SCMM and an accuracy of ±0.86% of the actual reading. The flow then passed through an eductor used for sand delivery and then into the coupon as shown in Figure 1.3. A constant effort was made to ensure a hermetic seal throughout the coolant supply system.

The sand delivery system consisted of an eductor, a valve, and the piping necessary to deliver the sand-air mixture to the coupon. The eductor was used to mix the sand into the coolant flow upstream of the coupon. The eductor contained a nozzle designed to entrain the sand and a feed port above the nozzle to feed the sand through the use of gravity. A ball valve was placed on top of the gravity feed port located far enough outside the kiln so that sand could be safely added while the kiln was heating the coupon. The eductor was located as close as possible to the coupon to minimize deposits on the supply tube walls. The location chosen was approximately 40 cm upstream of the coupon, as shown in Figure 1.3.

The ability for the eductor to drive the sand into the coupon was dependent on the pressure ratio across the eductor. The mass flows required for the target pressure ratio ranges in the coupon were somewhat higher than those indicated for this eductor design. Therefore, a bypass line with a control valve was used to set the pressure ratio across the eductor above a minimum threshold pressure required to move the sand. The bypass line allowed adequate mass flow to set the pressure ratio across the coupon.

Since coolant and metal temperatures are important parameters in the sand blockage and flow parameter, these temperatures were matched to realistic engine operating conditions. To match the coupon metal (980-1040°C) and coolant temperatures (650-700°C) to those found in turbine engines, a ceramic kiln with four heater elements was used. The kiln was supplied with 6.9 kW of power, to ensure it could raise the temperature inside the kiln to over 1090°C during testing. The kiln had several ports so that different parts of the test rig could protrude through the 7.6 cm firebrick to the outside air. A programmable electronic controller was used to ramp up and to maintain the kiln temperature within ± 5°C.

Since the coolant air traveled through a tube before it reached the coupon, its temperature depended on the kiln temperature and the heat transfer coefficient inside the supply tube for that particular flow rate. Depending upon the flow rate through the coupon, the temperature of the coolant could vary significantly without some other form of control. A double-pass heat exchanger was constructed around the coolant supply tube, as shown in Figure 1.3. The heat exchanger was designed so that compressed air could be supplied to it and vented to atmosphere, outside of the kiln to reduce the load on the kiln. With the extra control of the heat exchanger, all of the coolant temperatures and metal temperatures were matched for all pressure ratios in the 60-hole coupon.

Instrumentation

A combination of pressure transducers and thermocouples were used to measure several key parameters throughout the test rig including the coolant temperature, pressure ratio, coolant mass flow, and metal temperature of the coupon. The thermocouple and pressure probes used to measure the temperature and pressure inside the coupon were fed through tubes such that the feed through port, illustrated in Figure 1.4, between

atmospheric air and high-pressure air could be located outside the kiln. Feeding the instrumentation into the port in this manner allowed the seal and probes to be protected from the high temperature air in the kiln. The coolant temperature was monitored with a Type K nickel-chrome sheathed thermocouple probe inserted in the flow with the measurement end centered in the coupon. Due to the relatively large area ratio of the plenum to the coolant holes (63:1 for the 60-hole coupon) and the relatively low velocity, the inside of the coupon was treated as a plenum. As such, the orientation of the pressure probe was irrelevant, and a simple static pressure probe was fabricated with small gage (1.6 mm diameter) Inconel 625 tubing. The tube was inserted through the coolant supply tube to protect it from the high kiln temperatures and centered in the coupon. There was a 5% blockage from the pressure probe in the coolant supply tube.

It was not possible to directly measure the metal temperature because a thermocouple could not be directly mounted onto the coupon. As such, the metal temperature was calculated through an effectiveness parameter. Effectiveness is defined in equation 1.2 and is a dimensionless ratio that relates the known temperatures of the kiln air (T_∞) and coolant air (T_{oc}) with the temperature of the metal for different Reynolds numbers.

$$\phi = \frac{T_\infty - T_{metal}}{T_\infty - T_{oc}} \tag{1.2}$$

Effectiveness tests were conducted at temperatures where thermocouples could be attached to the coupon. These effectiveness values were then used for the higher temperature tests to deduce the metal temperatures. Effectiveness tests were conducted for a range of Reynolds numbers. Thermocouples were mounted in two locations along the middle row of cooling holes, spaced 6 mm away from the nearest cooling hole, as shown in Figure 1.4. The kiln air temperature was also monitored with a type K thermocouple located directly above the coupon (away from the cooling). The coolant air was measured with the coolant thermocouple inside the coupon. The coupons were tested at two different kiln temperatures (260°C and 540°C) and several different Reynolds numbers. The results confirmed that the effectiveness was a function of Reynolds number and independent of temperature, as shown in Figure 1.5. The effectiveness levels are lower than expected for a typical turbine airfoil because there were no internal cooling

features in the leading edge geometry as are designed in a turbine component. The dependence on Reynolds number in conjunction with the independence on temperature allowed the effectiveness to be used at all kiln temperatures to deduce the metal temperature of the coupon.

TESTING PROCEDURE AND METHODOLOGY

As was previously stated, the flow parameter can be calculated using equation 1.1 by determining the mass flow of air through a single hole, the upstream total coolant pressure and total coolant temperature, and using the diameter of the hole. A baseline flow parameter (FP) versus pressure ratio (PR) curve was measured, as shown in Figure 1.6, for the 36 and 60-hole coupons. The difference between the flow parameters from the 36 and 60-hole coupons is from uncertainty including manufacturing tolerances. The manufacturing tolerance on the hole diameter was $\pm$ 6.35x10^{-5} m. The baseline flow parameter was curve fit so that it could be approximated for all pressure ratios. This was necessary because when sand was introduced into the coupon the blockage not only reduced the flow parameter but also increased the pressure ratio. In addition, because flow parameter is a function of temperature, another baseline curve was curve fit at engine temperatures, shown in Figure 1.7.

The flow parameter for a film-cooling hole can be approximated by assuming one-dimensional flow. The pressure ratio of the coupon total pressure to the atmospheric pressure can be calculated as shown in equation 1.3.

$$PR = 1 + \left(f\frac{L}{D} + k_{inlet} + k_{exit} \right)\frac{\rho V^2}{2P_\infty} \tag{1.3}$$

The first term is the viscous loss in a smooth pipe using the Blasius correlation for friction factor. The second term is the total pressure loss due to a square-edged entrance condition into the film cooling, using a value for k_{inlet} of 0.4. The third term is the total pressure loss due to a square-edged exit loss, using a value for k_{exit} of 0.6. From this equation, the velocity is calculated and used to determine a mass flow and, hence, flow parameter. For a pressure ratio of 1.4, the Reynolds number was 6875, the friction factor

was 0.0347, and the calculated exit velocity was 202 m/s. The prediction works very well, as shown in Figure 1.6, and compares well with actual data from the 36 and 60-hole coupon.

As shown in Figure 1.7, different flow parameters occur for heated and cold conditions. These differences are due to changes in viscosity as well as slight cooling hole expansion that occurs due to heating (expected to be a 2% increase in flow area). In this study, we are primarily interested in the percent reduction in flow parameter (%RFP). The percent reduction is a useful way to describe how the flow parameter changes as a result of sand blockage. Baseline values are used at either cool or hot conditions as appropriate. The percent reduction in flow parameter can be defined several different ways, as we have done in this paper. One method is to compare the percent reduction in flow parameter under cold conditions whereby the cold baseline is used as a reference and only a cold (room temperature) test is conducted. Determining the percent reduction in flow parameter $\%RFP_{CC}$ (cold sand test – cold baseline), shown in equation 1.4, can then be used to estimate the reduction of part flow for a given sand flow. Under cold conditions, FP_0 is the baseline flow parameter and FP is the flow parameter after sand has clogged the holes.

$$\%RFP = \frac{FP_0 - FP}{FP_0} \tag{1.4}$$

There are two methods to apply equation 1.4 for heated conditions. The first method, which will be called $\%RFP_{HH}$ (heated sand test – heated baseline), uses FP_0 as the baseline flow parameter at heated conditions, and FP as the value at heated conditions just after the sand is released. The second method, which will be called $\%RFP_{HC}$ (heated test – cold baseline), uses the cold baseline value of FP_0 just prior to the test and uses FP as the resulting value after sand has been injected and the coupon returned to room temperature after the heated test was conducted as illustrated in Figure 1.7.

The method of introduction to the test coupon was important because the coupon could have different blocking characteristics based on the release method. For simplicity and repeatability, a slug flow was used to test the blockage characteristics of the coupons. The slug flow was generated by placing a measured sand amount inside an airtight section of pipe connected by a valve to the eductor. When the valve was opened, the sand

fell into the eductor and the high velocity jet entrained the sand into the air as a slug flow. For a room temperature test, there is a step decrease in flow rate and step increase in pressure ratio after the sand was introduced into the component, as shown in Figure 1.8. After the sand blocks the hole, the flow parameter and pressure ratio remains at a steady state value. This ending value of pressure ratio and flow parameter are then used deduce the percent flow reduction (%RFP).

The sand amounts used in the coupon tests were deduced from similar tests with actual engine components. The tests injected sand into new components to simulate the flow parameter of a field run components. In an actual engine, the sand concentration would be a function of density ratio (overall pressure ratio) as discussed by Kim et al. [2]. A range of sand amounts was chosen for the coupon tests so that a range of sand concentrations could be simulated.

As a part of the testing methodology, the moisture content of the sand was minimized. The first reason is that the humidity in the laboratory could not be controlled, and therefore daily variations would have affected the sand adhesion characteristics, as was shown to happen through testing. The second reason is that desert regions where sand ingestion is common have very low humidity. The sand was kept in an oven maintained at 200°C for at least 4 hours prior to testing to maintain the sand at consistent, low moisture levels.

Prior to all tests, the coupon was cleaned until the original baseline flow parameter / pressure ratio relationship was verified. The coupon was cleaned using a combination of compressed air and small drill bits pushed through the cooling holes. For cold sand ingestion tests, the baseline flow parameter was measured at the target pressure ratio, and then dried sand was injected into the system through the use of the eductor. After a few seconds the system stabilized and remained blocked indefinitely, as was previously indicated by Figure 1.8. The final flow parameter and pressure ratio were measured for this steady state condition.

For the heated tests, as was stated, a kiln was used to raise the temperature of the metal and coolant within a realistic range to satisfy the residence time criteria as described by Kim et al. [2]. The target temperature ranges were 1010 ± 30°C for the metal temperature, and 680 ± 30°C for the coolant temperature. For the heated testing

procedures, initially the room temperature baseline flow parameter / pressure ratio was verified. Then the kiln was turned on and allowed to ramp up to the target temperature with the coupon present having its appropriate coolant airflow. After the coolant and metal temperatures were steady and within the desired ranges, dried sand was added to the sand feed port above the eductor and injected into the system. The $\%RFP_{HH}$ was calculated by taking the flow parameter just after sand injection and comparing it to the baseline flow parameter for the same ending pressure ratio. The coupon was then cooled down to room temperature and another measurement was made at the original pressure ratio and compared to the cold baseline in order to get a $\%RFP_{HC}$.

Uncertainty Analysis

An uncertainty analysis was performed on several key parameters using the partial derivative method, shown in Table 1.1. The uncertainty of the pressure ratio was calculated to be $1.1 \pm 6.6 \times 10^{-5}$ and $1.6 \pm 9.6 \times 10^{-5}$. The uncertainty of the flow parameter was calculated to be between 4.6 % and 8.0% dominated by the bias uncertainty of the laminar flow element differential pressure transducer. The uncertainty of the %RFP was a maximum under the heated conditions at a low pressure ratio where the measurement was 8.5 ± 0.85%. Under heated conditions, the accuracy of the metal temperature through the effectiveness method was calculated to be 1010 ± 32°C. The uncertainty in the sand measured for each test was estimated to be 0.5 ± 0.001g.

A repeatability study was conducted to determine how many identical cases were required to achieve a reasonable confidence interval on the experimental average %RFP. To determine how many tests were required a series of 25 cases with matching pressure ratio and sand amount were conducted at room temperature. A 95% confidence interval was calculated from the standard deviation of the averages from each sample size of five samples. It was found that the ideal balance between a small confidence interval and a large number of tests was to conduct three tests at each pressure ratio and sand combination. This resulted in a confidence interval of 6.9%.

SAND CHARACTERIZATION

The sand types tested were standard test sands chosen to have similar properties as the sand found in desert and arid regions. While naturally occurring sand may have

variations in its properties, the test sands were used for consistency. The parameters that were considered important were size distribution, chemical composition, and sand grain density. Each one of these parameters was found to have a significant effect on the results of the testing.

Sand diameter is important because in conjunction with sand grain density, it dictates how well the sand will follow streamlines in curved or obstructed passages. The more surface area a particle has, the more drag it will have and it will tend to be accelerated by the flow easier. Three different sand diameter distributions were tested to get the effect of sand diameter on blockage. The size distribution was measured with a laser diffraction particle size analyzer. The particle analyzer determined the size of the particles in certain ranges, and then reported the percent of particles by volume that fell into each category. The size distributions measured for the two tests dusts shown in Figure 1.9, compare well to the specifications provided by Powder Technology, Inc. The ISO Fine test dust was found to have the lowest average diameter followed by the ISO Coarse test dust and then the VT test dust.

The VT test dust was created by using a sieve shaker and a series of sieves. The sieves were set up to filter out many of the particles less than 75 μm from the ISO Coarse test dust. The sand increased the mean diameter of the original ISO Coarse test dust to 50.0 μm from the original 37.3 μm. The mean diameters for the three test dusts, shown in Figure 1.9, show again that the distributions varied for each of the three dusts, with the smallest mean diameter being the ISO Fine, then the ISO Coarse, then the VT test dust.

The sand grain density is important because it pertains to how well the particles follow the streamlines, and to how much momentum a given particle will have on impact. Small dense particles will not follow streamlines well at all, however, large light particles will follow streamlines better. In addition, the small dense particles will tend to impact with more momentum onto the surface increasing the probability that they will rebound and follow the flow rather than sticking. The sand grain densities were measured with a pycnometer, with a maximum standard deviation of 0.0051 g. A pycnometer takes a known mass of sand and fills a container to different pressures with a known gas while it measures the volume of gas that is required to reach each pressure. Using the ideal gas

law, the volume of the container being taken up by solid particles, and hence the density is determined. The densities for all three sands, shown in Figure 1.9, were very similar.

The sand chemical composition was quantified because at the high temperatures that gas turbines operate, it is possible to melt the sand. The composition was qualitatively analyzed with an SEM EDAX system. The EDAX system reports a bulk power spectrum over the entire sample as well as results for particular grains. While the grains vary over a range of different compounds, the bulk power spectrum, shown in Figure 1.10, indicate that the test dusts are crushed granite. The analysis of each of the samples agree with the manufacturer's specification stating that it contains different phases of quartz (SiO_2) up to approximately 68-76%. The other major constituent is aluminum oxide (Al_2O_3) between 10-15%, with traces of iron oxide (Fe_2O_3), sodium silicate (Na_2O), lime (CaO), magnesium oxide (MgO), titanium dioxide (TiO_2), and potassium oxide (K_2O), in descending concentration.

The melting point is another parameter that is important for tests where the metal temperature and coolant temperature are at engine conditions. It is known that particle size and chemistry affects the melting point of sand made up of a mixture of materials as discussed by Dunn et al. [3]. The crushed granite has many different constituents that, given their size, have a lower melting point than larger samples of the same material. To establish an estimate of the melting temperatures, sand samples were exposed to temperatures ranging from 930°C to 1090°C for thirty minutes, and then removed. Figure 1.11 shows the samples after their tests at a given temperature. The sample at 930°C has a slight coloration change from what is seen at room temperature, indicating that melting had begun; however, no other major changes. The sample at 980°C has begun to form soft bonds with the material in close proximity, showing further signs of melting. While the sample at 980°C formed larger conglomerates than the sand at 1040°C, the sample at 980°C was easily broken apart, and looked much like the sample at 930°C when this is done. The sample at 1040°C has had a significant color change and solid particles much larger than the original sand size had begun to form. These darker particles also could not be broken apart, unlike the samples at lower temperatures. The last sample at 1090°C has melted completely and formed a single conglomerate. This conglomerate is solid and cannot be broken apart. If sand is present in an engine environment in this latter state,

interaction issues may occur. This is especially important since the next generation of engines may be operating at elevated turbine temperatures for increased performance capability.

After determining what temperature the sand begins to conglomerate, it is important to determine how quickly the particle can reach the surface temperature while flowing through the coupon. In this analysis, a simplified approach was taken where it was assumed that all of the energy transferred to the particle was from radiation. Convection was ignored because the temperatures were high enough and the slip velocity was low enough that convection was negligible. In addition, particle impacts with walls or other particles were ignored, although this may have served to heat the particle faster. The residence time in the coupon was estimated to be about 0.01 s assuming a straight path out of the coupon. This is considered a low estimate since it has been shown by Schneider et al. [4, 8, 9, 10], that particles can have a much longer residence time than the air that carries them depending on the path taken and that convection and conduction will also contribute to the temperature. From these approximations it was found that after 0.01 s the sand temperature is already over 820°C from a starting temperature of 675°C for a coupon metal temperature of 1010°C. Thus, the sand particle can quickly approach its melting temperature when it impacts the film-cooling hole walls.

DISCUSSION OF RESULTS

Results from this paper include sensitivity studies on metal temperature, coolant temperature, mean sand diameter, and pressure ratio. Tests were conducted at room temperature at different pressure ratios to determine the effects of sand amounts, sand diameter, and number of cooling holes on the $\%RFP_{CC}$. Heated tests were conducted to determine the combined effect of coolant and metal temperature on the $\%RFP_{HH}$ and $\%RFP_{HC}$. Lastly, the metal temperature and coolant temperature were varied independently to determine its effect on the $\%RFP_{HH}$ and $\%RFP_{HC}$ at a given pressure ratio and sand amount. Nominal operating parameters for cold and heated tests are listed in Table 1.2.

Room Temperature Experimental Results

This section will present the results obtained with the 36 and 60-hole coupon at room temperature with varying pressure ratios, sand amounts, sand diameters, and number of cooling holes.

For the 36-hole coupon, varying amounts of ISO Fine test dust were injected at different pressure ratios at room temperature. It was indicated earlier, that to reduce the uncertainty in the %RFP, three tests were run. Figure 1.12 shows the distribution of the raw test data for a sand amount of 0.3 grams. Figure 1.12 indicates that for a given pressure ratio, more sand resulted in a larger $\%RFP_{CC}$. With increasing sand amounts, the concentration of entrained sand increased, and therefore the number of impacts on the walls increased. With increasing impacts, the total number of grains that adhered to the cooling holes was higher. The results for a constant sand amount over a range of pressure ratios indicates that the $\%RFP_{CC}$ is less for increasing pressure ratios. For example, a given sand amount causes less blockage at a pressure ratio of 1.2 than it does at 1.1. The reason for this was that there was more coolant mass flow for a high pressure than a low pressure ratio. The higher coolant mass flow and air velocity caused the sand particles to travel at a higher velocity than at lower pressure ratios, and hence reduced the residence time in the coupon. The high sand velocity also caused more particles to rebound off surfaces rather than adhere to them. The increased likelihood of rebounding and the lower residence time reduced the probability of a given grain adhering to the wall. Figure 1.12 also indicates that there is a larger relative decrease in $\%RFP_{CC}$ between a pressure ratio of 1.1 and 1.2 than there is between 1.2 and 1.5. There is another sharp decrease in $\%RFP_{CC}$ between a pressure ratio of 1.5 and 1.6. The sharp decreases in these two ranges are from the increase in coolant mass flow, however this response does not appear linear since there are not corresponding reductions between pressure ratios of 1.2 to 1.5.

While the shapes of the curves are not well understood, there is a consistency between tests at different sand amounts. Figure 1.13 shows the same curves of $\%RFP_{CC}$ normalized by the sand amount. Figure 1.13 shows that for a given pressure ratio, the normalized $\%RFP_{CC}$ is nearly the same for all sand amounts. This finding indicates that at room temperature, for a consistent sand type and pressure ratio, $\%RFP_{CC}$ is a nearly

linear function of sand amount. There is one curve in Figure 1.13 that has a slight disagreement with this trend. The lowest sand amount of 0.1 grams has a larger blocking per gram than any other curve. In addition, at a pressure ratio of 1.1, the blocking per gram is 20% higher than the next highest sand amount.

It was important to determine if flow area had an effect on the $\%RFP_{CC}$. This was done by testing a coupon similar to the 36-hole coupon, but with a total of 60 cooling holes. Over a range of pressure ratios, 0.5 grams of ISO Fine test dust was injected into the 60-hole coupon. The 60-hole coupon has 67% more coolant flow area than the 36-hole coupon, and hence approximately 67% more mass flow at a given pressure ratio. Figure 1.14 shows the effect of increased flow area on the $\%RFP_{CC}$ over a range of pressure ratios. The lower level of blocking observed in the 60-hole coupon is observed because of the increased mass flow through the inlet tube. The inlet tube for both the 36 and 60-hole coupons had the same diameter. Therefore, the 60 hole coupon had higher velocity air in the inlet tube, and therefore higher velocity sand particles flowing through it. This higher velocity jet caused the particles to impact the opposite end of the coupon and fall out of the flow. This means that there was less sand available for blocking in the 60-hole coupon than the 36 hole coupon. The combination of these two effects causes a non-linear decrease in the %RFP.

For the 60-hole coupon, the effect of sand diameter was tested. This parameter is important because as the size distributions showed, individual sand grains can be on the order of one percent the size of the hole to around half the hole diameter. It is important to see the effect of different size distributions because different distributions will travel through the holes at different speeds, flow rates, probabilities of blockage, and with different effects on the local flow. The three sands that were tested were the ISO Fine, ISO Coarse, and VT sand that had mean diameters of 18.5, 37.3, and 50.0 μm respectively. Tests indicated that at room temperature the $\%RFP_{CC}$ was directly dependent on average sand diameter, and increased with increasing diameter as shown in Figure 1.15. The increased blockage with increasing sand diameter is due to the increase in the number of larger particles. These larger particles had a lower velocity than the smaller particles and therefore were less likely to rebound off surfaces after impact. In

addition, when the larger particles adhered to a surface they had more of an effect because they blocked more flow area than the smaller particles.

Figure 1.16 shows the same data as in Figure 1.15, but with lines of constant pressure ratio separated by the three sand diameters tested. As the mean diameter increases, the $\%RFP_{CC}$ increases in a non-linear fashion. In Figure 1.16 there is also one series of data that stands out. At the high pressure ratio of 1.6, there is a lower $\%RFP_{CC}$ for all sand types than the other pressure ratios. This is most likely because of the larger mass flow through the cooling holes at a pressure ratio of 1.6.

Heated Experimental Results

Heated tests were conducted using 0.5 grams of ISO Fine test dust to determine the effect of engine-representative temperatures on the sand blocking, as well as determining the sensitivity to varying metal and coolant temperatures. This section reviews the results from testing conducted at temperatures intended to match representative metal and coolant temperatures in propulsion gas turbine engines. The target metal temperature was between 980°C and 1040 °C, and the target coolant temperature was between 650°C and 700°C. While this range of temperatures was obtainable with the use of the heat exchanger, there were some temperature variations between pressure ratios, as shown in Figure 1.17. The tests also isolated the effect of metal temperature and the effect of coolant temperature to determine how important they are relative to each other.

The comparison between the $\%RFP_{HC}$, $\%RFP_{HH}$, and $\%RFP_{CC}$ for the same 0.5 grams of ISO Fine test dust over a range of pressure ratios is shown in Figure 1.18. The elevated metal and coolant temperature caused significantly more %RFP than occurred at room temperature for the entire range of pressure ratios. Also important to note is that the $\%RFP_{HC}$ was always more than the $\%RFP_{HH}$. This difference between $\%RFP_{HH}$ and $\%RFP_{HC}$ tended to be larger at higher pressure ratios and indicated that the blockage increased as the part cooled back down to room temperature. The reason the difference between $\%RFP_{HC}$ and $\%RFP_{HH}$ increased at higher pressure ratios was that the local metal temperature increased rapidly immediately after the sand blockage. The higher pressure ratio tests, having a higher kiln temperature, had local metal temperatures very

close to the kiln temperature after sand injection. This higher local metal temperature melted the sand inside the coolant holes, and increased the blockage. This is consistent with other tests conducted at intermediate coolant and metal temperatures not reported here.

To determine and separate the effects of the coolant temperature and the metal temperature, a series of tests were conducted with a constant metal temperature and a series of tests were conducted with constant coolant temperature. The results from the constant metal temperature of 1010°C and varying coolant temperature are shown in Figure 1.19. Increasing the coolant temperature caused a minimal increase in $\%RFP_{HH}$. However, there is a large increase in $\%RFP_{HC}$ due to a spike in metal temperature after sand was introduced to the system. The sand injection caused the metal temperature to increase rapidly toward the kiln temperature and began to melt the sand already adhered to the cooling holes. This effect, however is a metal temperature effect, not a coolant temperature effect. The increase in coolant temperature has a minimal effect on $\%RFP_{HH}$.

The sensitivity of blockage to metal temperature was determined by maintaining a constant coolant temperature of 675°C and varying the metal temperature. This resulted in a more severe increase in %RFP than the constant metal temperature tests. Figure 1.20 shows that the affect of metal temperature on the %RFP is relatively steady as the metal temperature increased towards 1000°C, however, the trend became non-linear between 1000°C and 1080°C. This was most likely due to the melting of the sand as it contacted the metal in the coolant hole. This contact caused immediate melting of the sand and adhesion to the surface. These melted particles then caused further sand impacts at the same location to adhere because of the increased tackiness of the wall surface.

SUMMARY

Gas turbine engines are being designed to operate with ever increasing turbine inlet temperatures while simultaneously operating in very harsh conditions. Without sufficient cooling, turbine parts will degrade rapidly and cause performance and efficiency loss. Dust and sand from runways are frequently ingested into engines during takeoffs and landings. This ingested sand can block the coolant passages, restricting the flow to hot section turbine components. This reduction of cooling air can contribute to

degradation of the turbine components, and a decrease in the maintenance life. Without heavier land-based filtration sytems, and ever increasing turbine inlet temperatures, engines must have a robust cooling system that can mitigate sand and dust ingestion.

This study determined how a simple array of film-cooling holes reacted to several parameters considered important in sand blocking. Important parameters were determined to be pressure ratio, sand amount, sand distribution, number of holes, and metal temperature.

The pressure ratio affects the sand blocking by controlling the amount and velocity of the coolant driving the sand. A high pressure ratio has more mass flow going through the coupon, and therefore a high coolant velocity in the coupon. This increased coolant velocity increases the particle velocity through the coolant hole making it less likely that it will adhere to the coolant wall, causing blockage. For example, for the 36-hole coupon with 0.5 grams of ISO Fine test dust, the percent reduction in flow parameter is 9.7% at a pressure ratio of 1.1 and is 4.6% for a pressure ratio of 1.6.

The sand amount was determined to affect the blocking by changing the amount of sand per hole that flowed through the coupon. With increasing sand, more sand per hole was injected into the coupon. This increased the probability that more sand would adhere inside the film-cooling hole. For the 36-hole coupon at a pressure ratio of 1.4 and 0.1 grams of ISO Fine test dust caused a 1.7% reduction in flow parameter and 0.5 grams of ISO Fine test dust at the same pressure ratio caused an 8.1% reduction in flow parameter.

The sand size distribution was important in determining the percent reduction in flow parameter. The higher the average size of a sand sample, the higher the percent reduction in flow parameter. If the same number of particles adhere to the cooling holes for both sand sizes, the amount of area blocked per is dictated by the average sand size. The three sands that were tested on the 60-hole coupon had average sizes of 18.5, 37.3, and 50 μm. For a pressure ratio of 1.4, these sands had percent reductions in flow parameter of 2.2%, 2.7%, and 6.6% respectively.

The number of cooling holes had an impact on the percent reduction in flow parameter. Increasing the number of cooling holes decreased the percent reduction in flow parameter. The increased number of cooling holes caused the sand to be divided

over a larger number of holes, causing less of a percent reduction in flow parameter. The increased number of cooling holes also caused more mass flow through the coupon, and through the coupon supply tube. Since the supply tube was the same diameter for both the 36 and 60-hole coupons, the coolant velocity in the 60-hole coupon was greater. The higher velocity cooling air caused more particles to impact the opposite side of the coupon and drop out of the flow prior to entering the cooling holes. This decreased the amount of sand available for blocking, and hence reduced the percent reduction in flow parameter. Both coupons were injected with 0.5 grams of ISO Fine test dust at a pressure ratio of 1.4. The 36-hole coupon had an 8.1% reduction in flow parameter while the 60-hole coupon had a 2.2% reduction in flow parameter.

The metal temperature of the coupon was found to be the most significant parameter in this study. With increasing metal temperature the percent reduction of flow parameter increases steadily until a threshold temperature of about 1000°C. After this temperature, the percent reduction for a set amount of sand increases drastically. When the metal temperature passed about 1000°C, the particle most likely melted on impact or melted shortly after impact. The molten test dust acted as a thermal barrier coating on the inside of the blade. This coating reduced the heat transfer inside the blade, further increasing part temperature. The combination of increased metal temperature from the sand already adhered to the surface, and the increased tackiness of the surface caused subsequent particles to have a higher probability of adhesion. For the 60-hole coupon at a pressure ratio of 1.4 with ISO Fine test, the percent reduction in flow parameter was 5.5%, 5.6%, and 7.7% for temperatures of 882°C, 992°C, and 1028°C respectively.

These parameters are all important to dictating the flow reduction, and hence the life of a gas turbine component. However, in actual engine conditions, it is important to manage metal temperature when under high sand loadings. The coupon tests showed that, other conditions held constant, when the metal temperature exceeds a threshold temperature, the adhesion characteristics can be significantly enhanced and may cause permanent damage. In the engine environment, efforts should be focused to minimize and manage sand ingestion in the secondary flow system. This will result in fewer particles, thus less potential for their adhesion, and a decreased probability of permanent component damage.

REFERENCES

[1] Moroianu, D., Karlsson, A., 2004, "LES of the Flow and Particle Ingestion into an Air Intake of a Jet Engine Running on the Ground," GT2004-53762

[2] Kim, J., Dunn, M.G., Baran, A.K., Wade, D.P., Tremba, E.L., 1993, "Deposition of Volcanic Materials in the Hot Sections of Two Gas Turbine Engines," J of Turbomachinery, vol. 115, pp. 641-651.

[3] Dunn, M.G., Padova, C. and Adams, R.M., 1987a, "Operation of Gas Turbine Engines in Dust-Laden Environments," AGARD-Advanced Technology Aero Engine Components, Paris, France.

[4] Schneider, O., H.J., Benra, F.-K., Dohmen, H. J., and Jarzombek, K., 2005, "A Contribution to the Abrasive Effect of Particles in a Gas Turbine Pre-Swirl Cooling Air System," GT2005-68188

[5] Batcho, P.F., Moller, J.C., Padova, C., and Dunn, M.G., 1987, "Interpretation of Gas Turbine Response Due to Dust Ingestion," 1987-GT-112

[6] Ghenaiet, A., Elder, R.L., and Tan, S.C., 2001, "Particles Trajectories Through an Axial Fan and Performance Degradation due to Sand Ingestion," 2001-GT-0497

[7] Tabakoff, W., and Metwally, M., 1992, "Coating Effect on Particle Trajectories and Turbine Blade Erosion," *J of Turbomachinery*, vol. 114, pp. 250-257.

[8] Schneider, O., Dohmen, H.J., Reichert, A.W., 2002, "Experimental Analysis of Dust Separation in the Internal Cooling Air System of Gas Turbines", GT-2002-30240

[9] Schneider, O., Dohmen, H.J., Benra, F.-K., and Brillert, D., 2004, "Dust Separation in a Gas Turbine Pre-Swirl Cooling Air System, a Parameter Variation," GT2004-53048

[10] Schneider, O., Dohmen, H. J., H.J., Benra, F.-K., and Brillert, D., 2003, "Investigations of Dust Separation in the Internal Cooling Air System of Gas Turbines," GT2003-38293

[11] Friedlander, S.K., 2000, Smoke, Dust, and Haze Fundamentals of Aerosol Dynamics, (Oxford University Press: NY)

[12] Wenglarz, R.A., and Fox, Jr., R.G., 1990, "Physical Aspects of Deposition from Coal-Water Fuels Under Gas Turbine Conditions," *J of Turbomachinery*, vol. 112, pp. 9-14.

[13] Hill, P., Peterson, C., 1992, Mechanics and Thermodynamics of Propulsion, (Addison-Wesley Publishing Company: Reading, Massachusetts)

Table 1.1. Uncertainties of Testing Parameters

	36-Hole Coupon		60-Hole Coupon		60-Hole Coupon (heated)	
PR	1.1	1.6	1.1	1.6	1.1	1.6
Tmetal	-	-	-	-	32°C	32°C
PR	1.1 ± 0.006	1.6 ± 0.006	1.1 ± 0.006	1.6 ± 0.006	1.1 ± 0.006	1.6 ± 0.006
Mass flow	5.76%	7.40%	5.17%	6.38%	6.34%	3.17%
FP	6.68%	8%	6.16%	7.36%	7.18%	4.62%
%RFP	9.74 ± 0.69%	4.58 ± 0.41%	2.74 ± 0.23%	0.42 ± 0.05%	8.46 ± 0.85%	5.2 ± 0.35%
effectiveness	-	-	-	-	0.29 ± 0.0036	0.29 ± 0.0043
Sand amount	5 ± 0.001 g					
Tcoolant	1°C					

Table 1.2. Nominal Testing Parameters

	Units		Cold		Heated
Cooling Holes		Cooling Holes	36	60	60
FP		FP	0.31 - 0.57	0.35 - 0.62	0.29 - 0.55
P_{oc}	kPa	P_{oc}	105-152	105-152	105-152
P_{oc}/P_{∞}		P_{oc}/P_{∞}	1.1-1.6	1.1-1.6	1.1-1.6
T_{oc}	°C	T_{oc}	23	23	654-693
T_{metal}	°C	T_{metal}	23	23	993-1004
T_{∞}	°C	T_{∞}	23	23	1065-1175
Φ		Φ	-	-	0.35
Sand Amounts	g	Sand Amounts	0.1-0.5	0.5	0.5
Sand Types		Sand Types	Fine	Fine, Coarse, VT	Fine

Figure 1.1. Sand is being ingested into the engines of a C-17 during a desert takeoff.

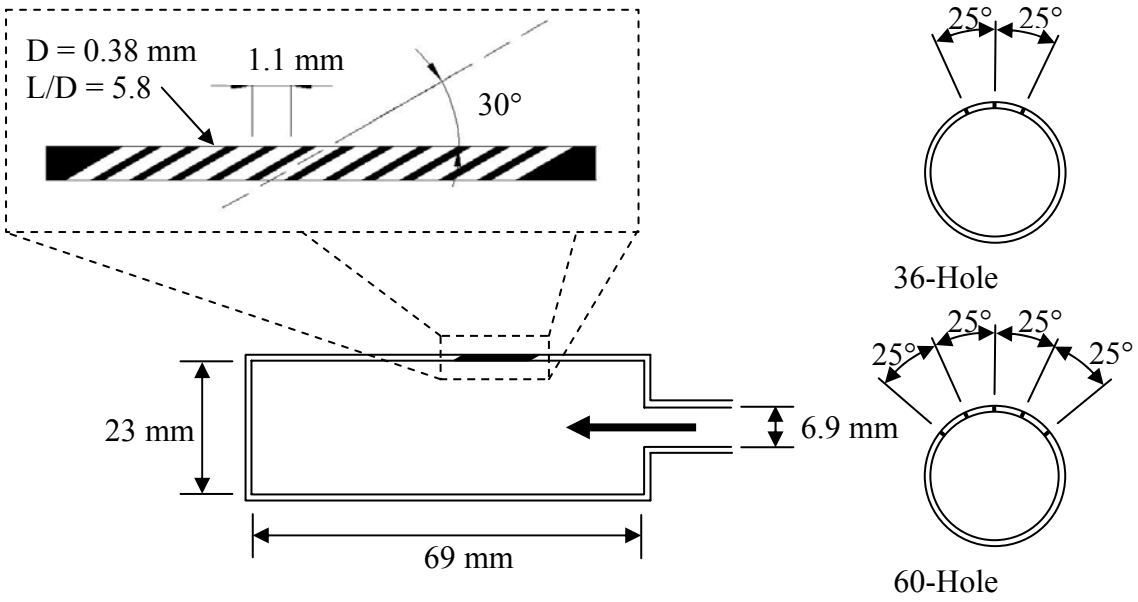

Figure 1.2. The coupon was designed to simulate the leading edge showerhead of a typical turbine blade or vane.

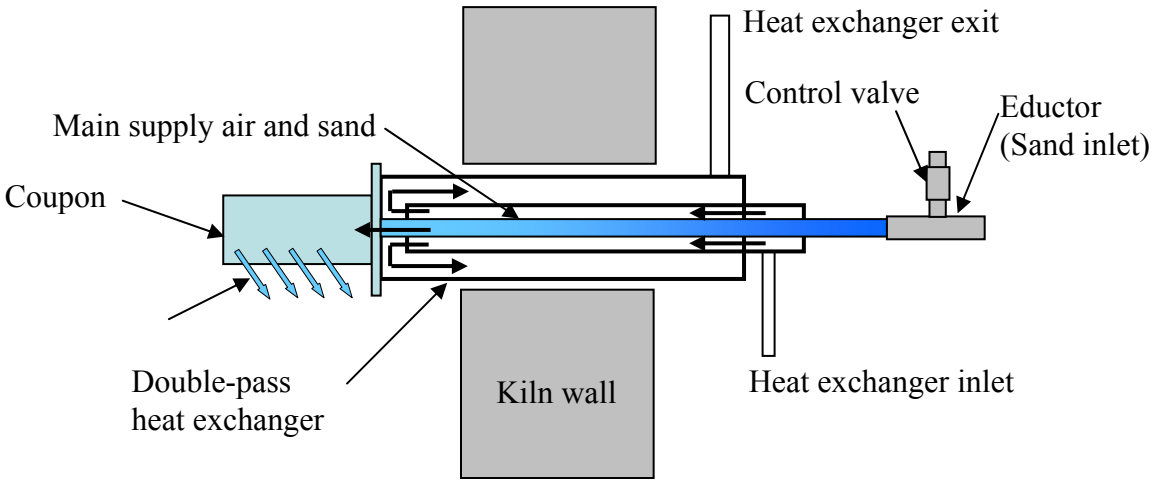

Figure 1.3. The coolant temperature was controlled by adjusting the heat exchanger flow rate.

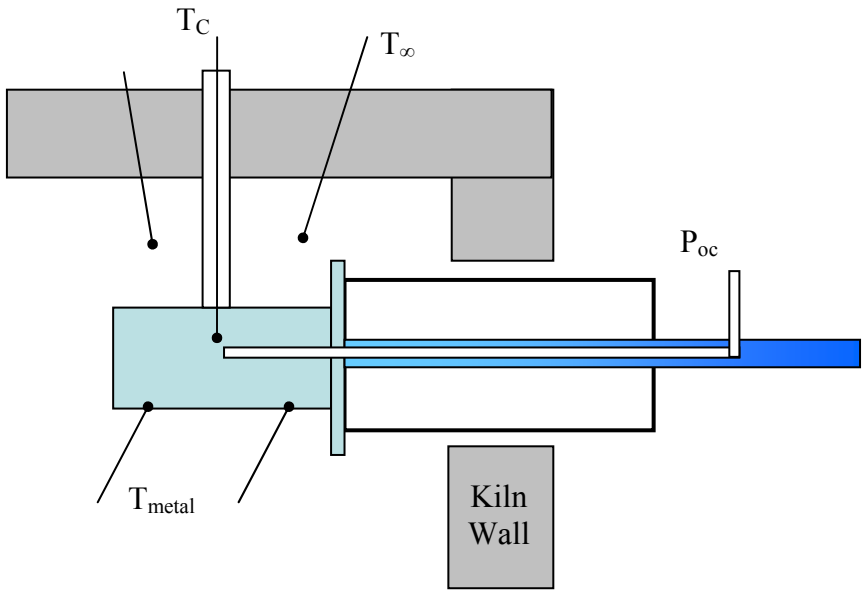

Figure 1.4. The effectiveness was determined so that the metal temperature could be determined at engine temperatures.

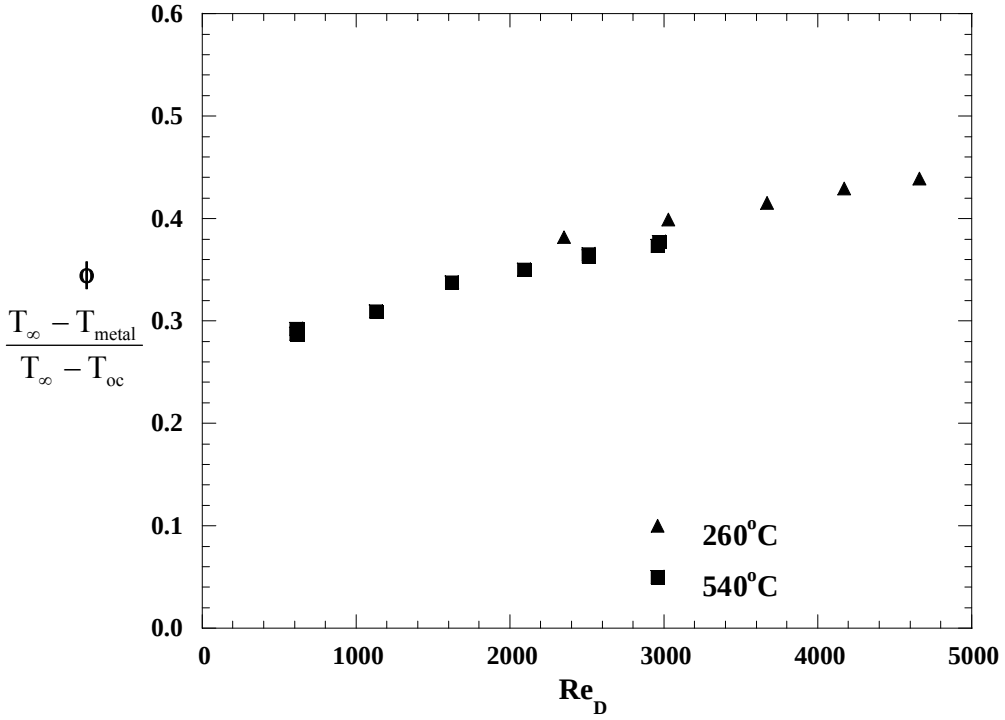

Figure 1.5. The effectiveness of the 60 hole coupon was a linear function of Reynolds number and independent of temperature.

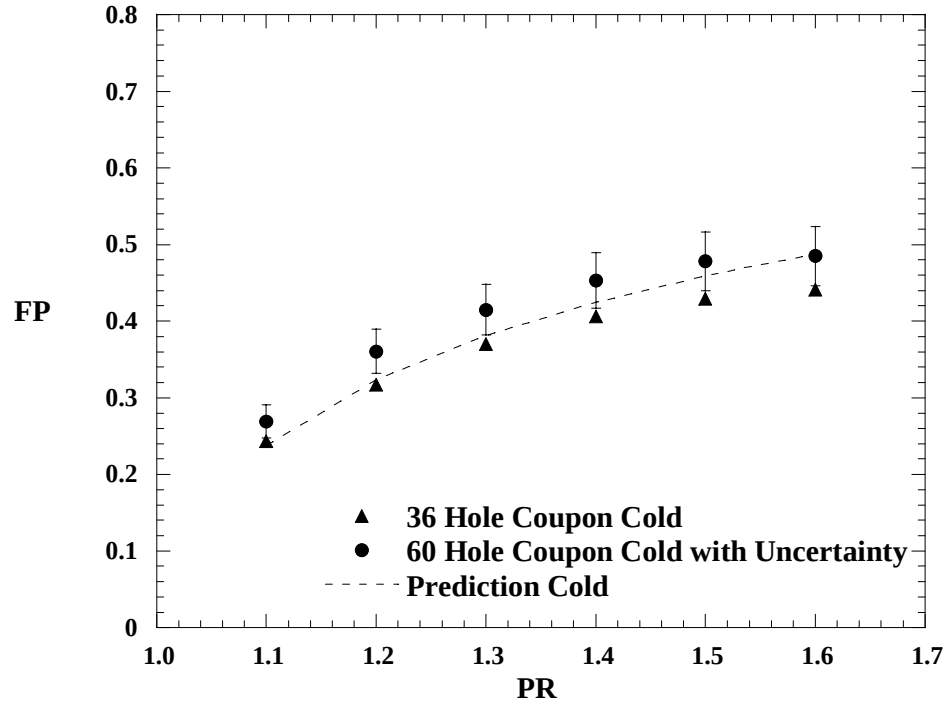

Figure 1.6. Baseline flow parameters were measured for both coupons and compared to a prediction of the flow parameter.

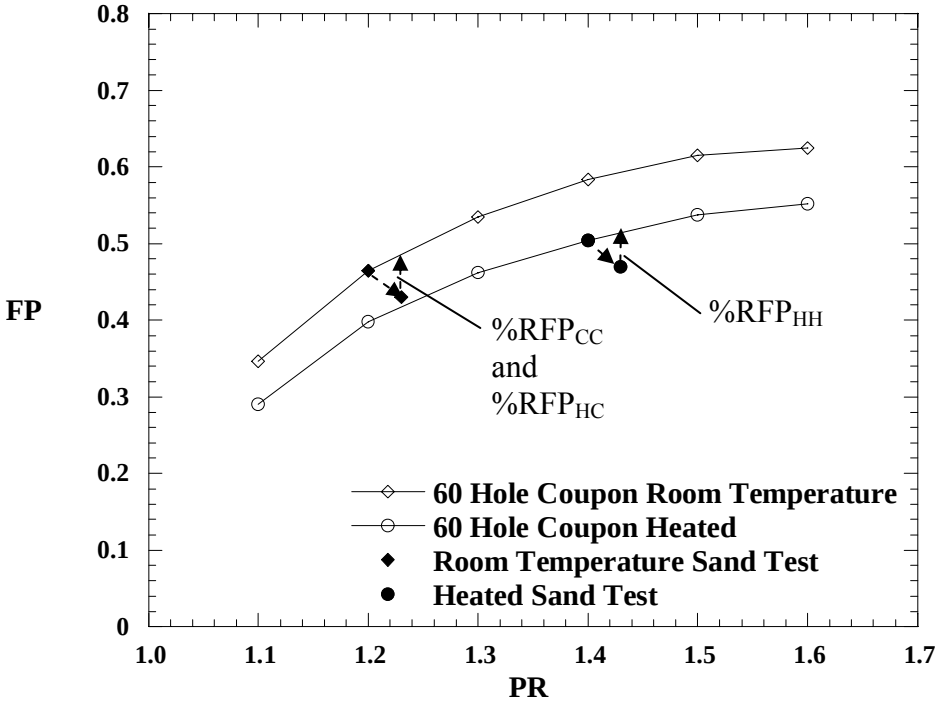

Figure 1.7. Flow parameters for cold and heated tests resulted in different flow parameters due to viscosity. This meant that there are two ways to measure %RFP for a heated test.

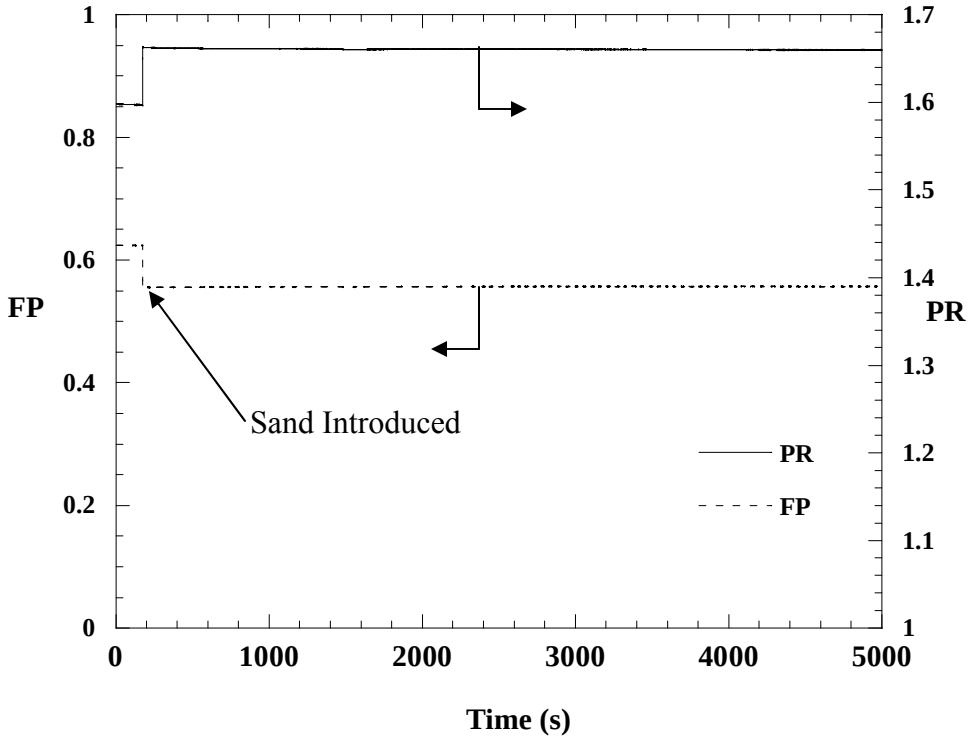

Figure 1.8. The flow parameter and pressure ratio stabilize a few seconds after sand is introduced in a cold test.

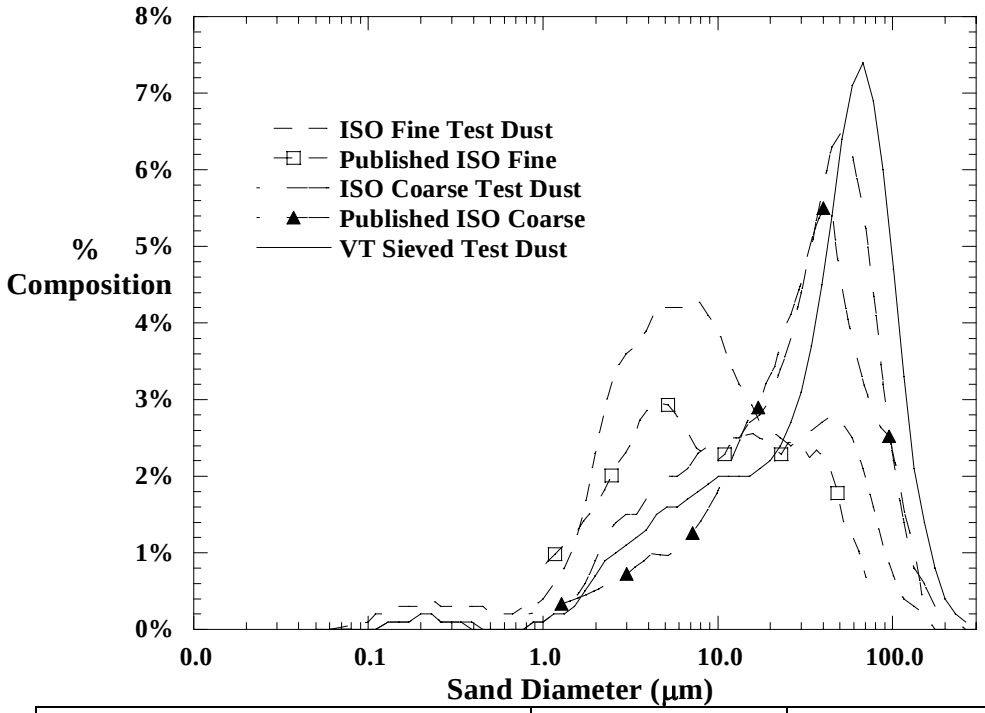

Sample	Density (g/cm^3)	Mean Diameter (μm)
Test Dust ISO 12103-1, A2 Fine	2.71	18.5
Test Dust ISO 12103-1, A4 Coarse	2.68	37.3
VT Sieved Test Dust	2.68	50

Figure 1.9 The particle size distributions were found to have a major impact on the %RFP for all cases.

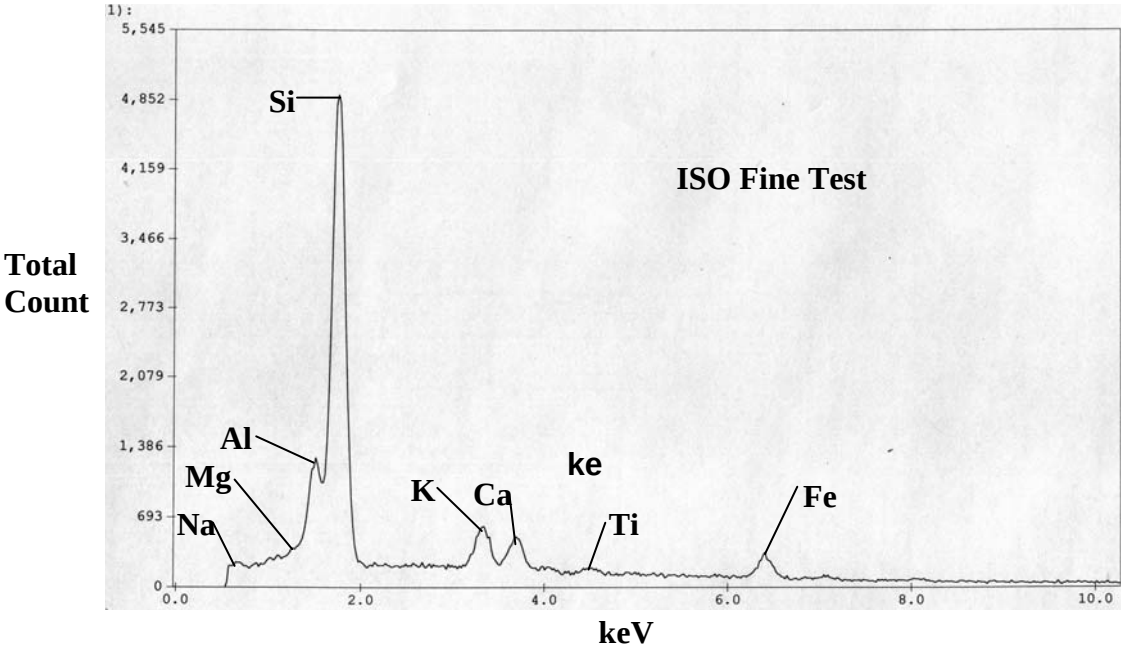

Figure 1.10. The molecular content of the test dusts indicates that the samples are crushed granite.

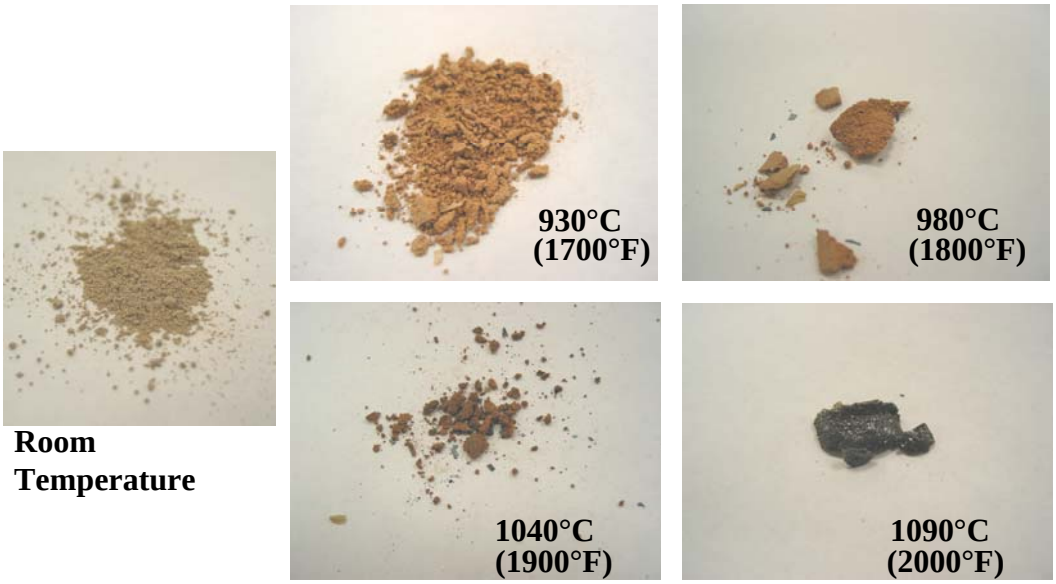

Figure 1.11. Dusts similar in composition to those found in arid regions melt at moderate temperatures.

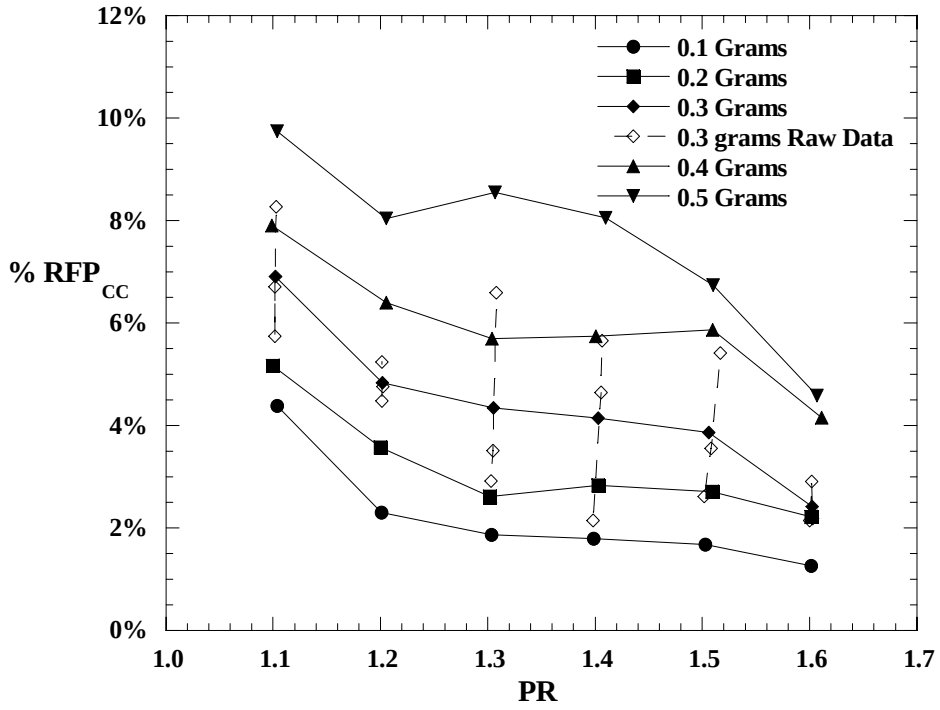

Figure 1.12. Increasing sand amount increases %RFP for a given pressure ratio (ISO Fine, 36-hole coupon).

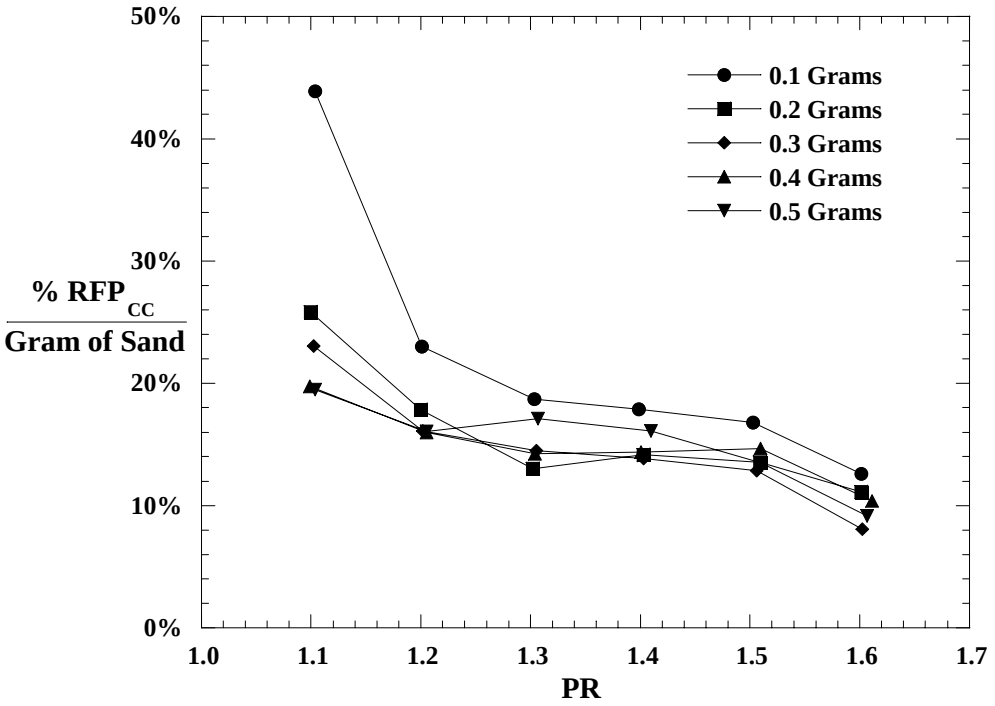

Figure 1.13. The %RFP has a nearly linear dependence on the sand amount (ISO Fine, 36-hole coupon).

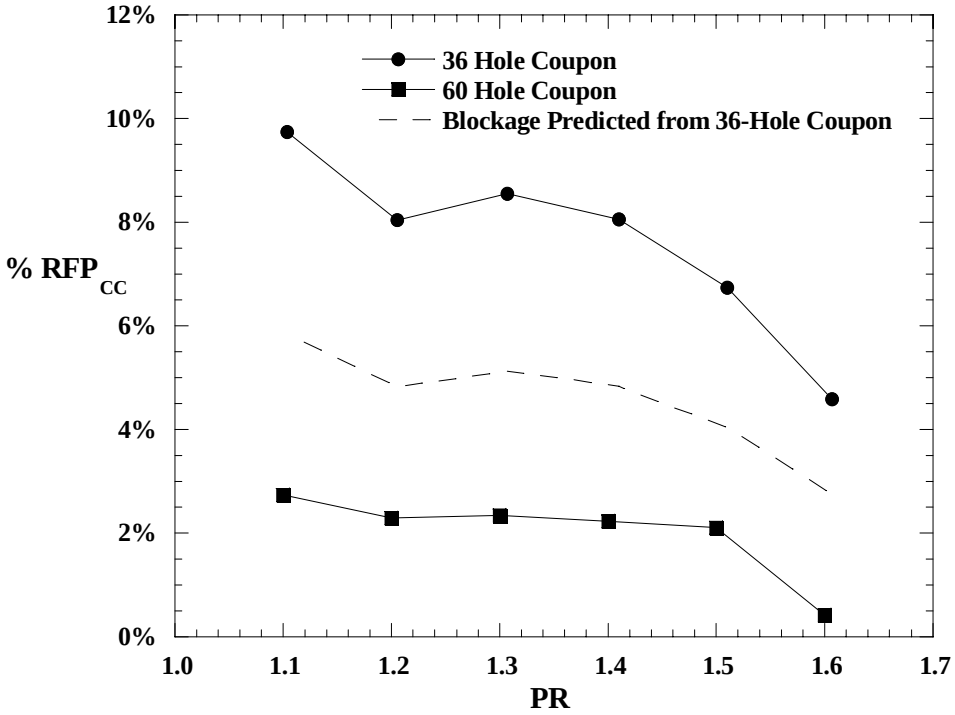

Figure 1.14. The number of coolant holes has a non-linear effect on the %RFP (0.5 g, ISO Fine test dust).

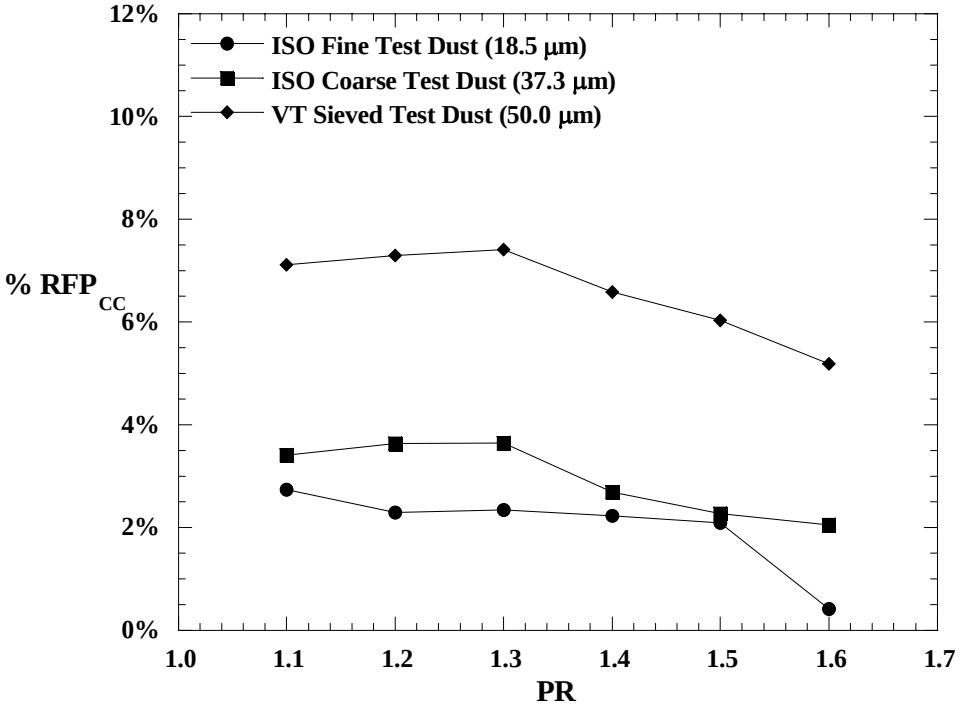

Figure 1.15. Increasing the average particle size results in increasing blockage (0.5 g, 60 hole coupon).

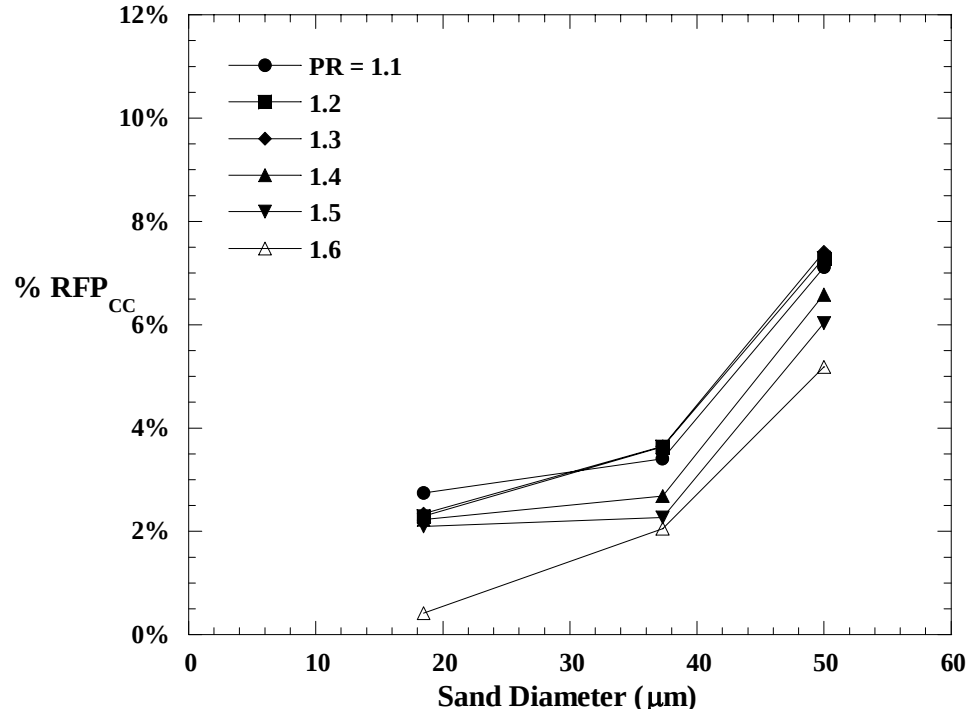

Figure 1.16. The increase of %RFP is not linear with increasing average sand diameter (0.5 g, 60 hole coupon).

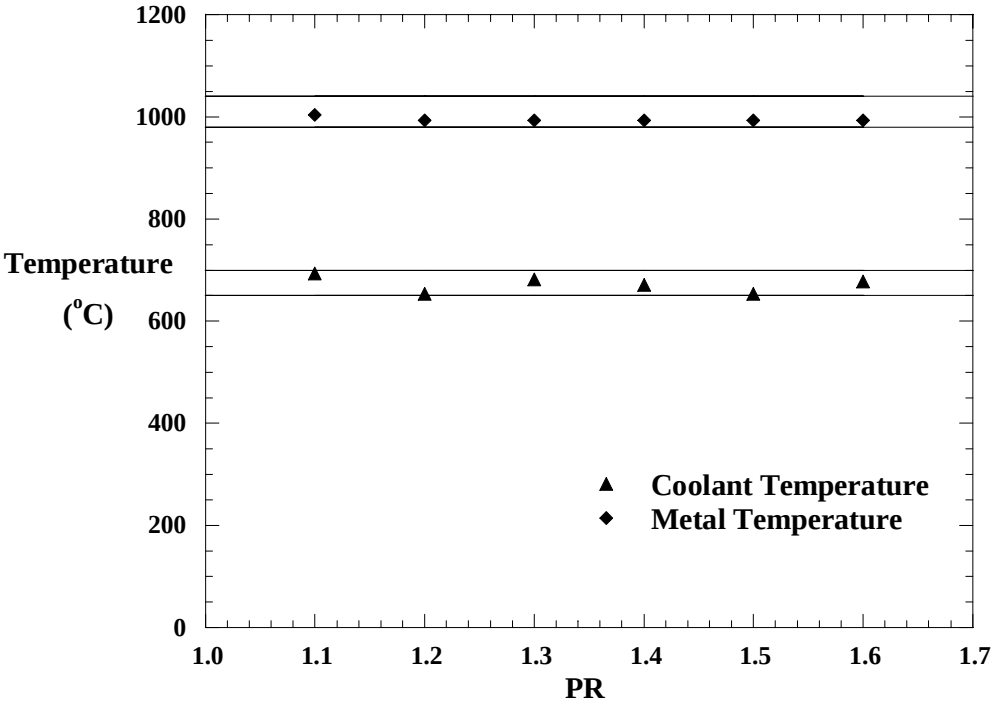

Figure 1.17. The temperature ranges were met for all pressure ratios, however, there were minor variations between tests (60 hole coupon).

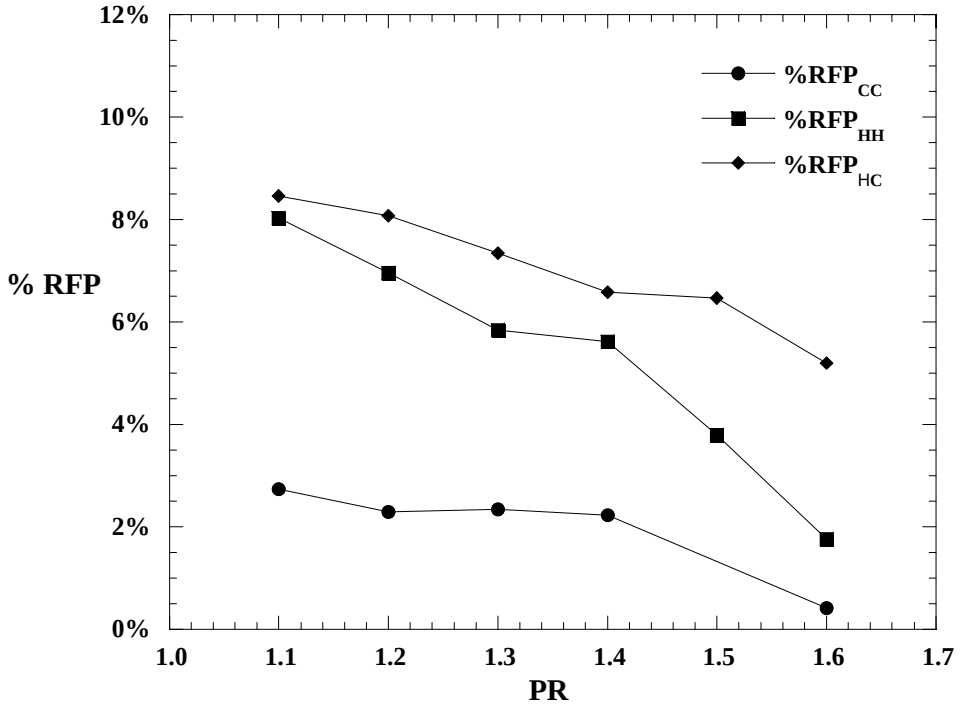

Figure 1.18. Operating at engine metal temperatures results in higher %RFP (0.5 grams iso fine 60 hole coupon).

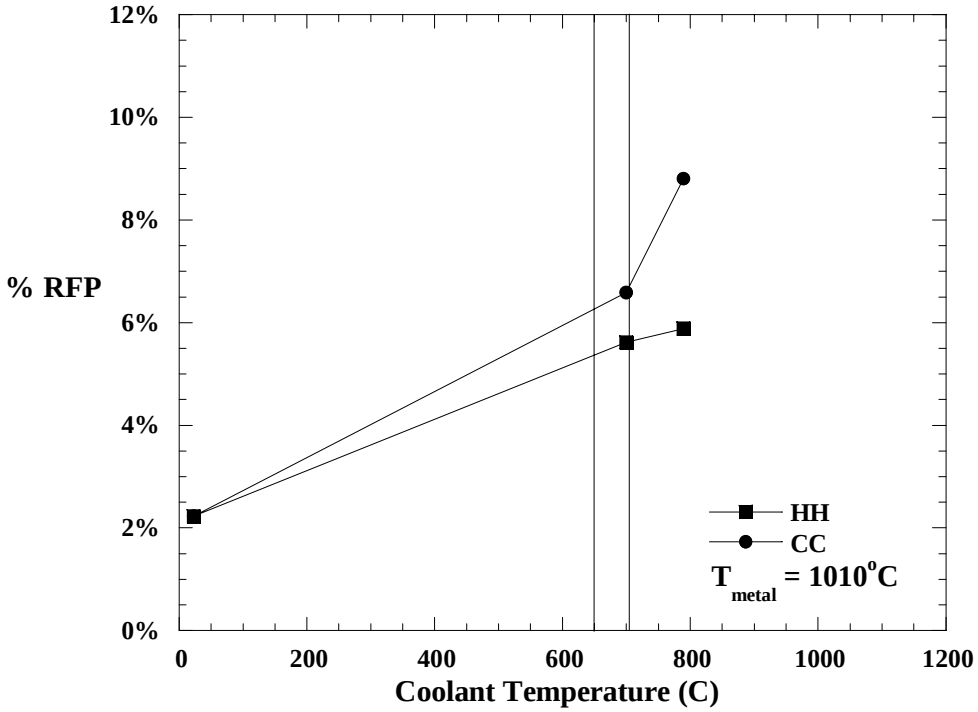

Figure 1.19. Operating at higher coolant temperatures increases %RFP (0.5 grams, ISO Fine 60-hole coupon, T_{metal} = 1010°C).

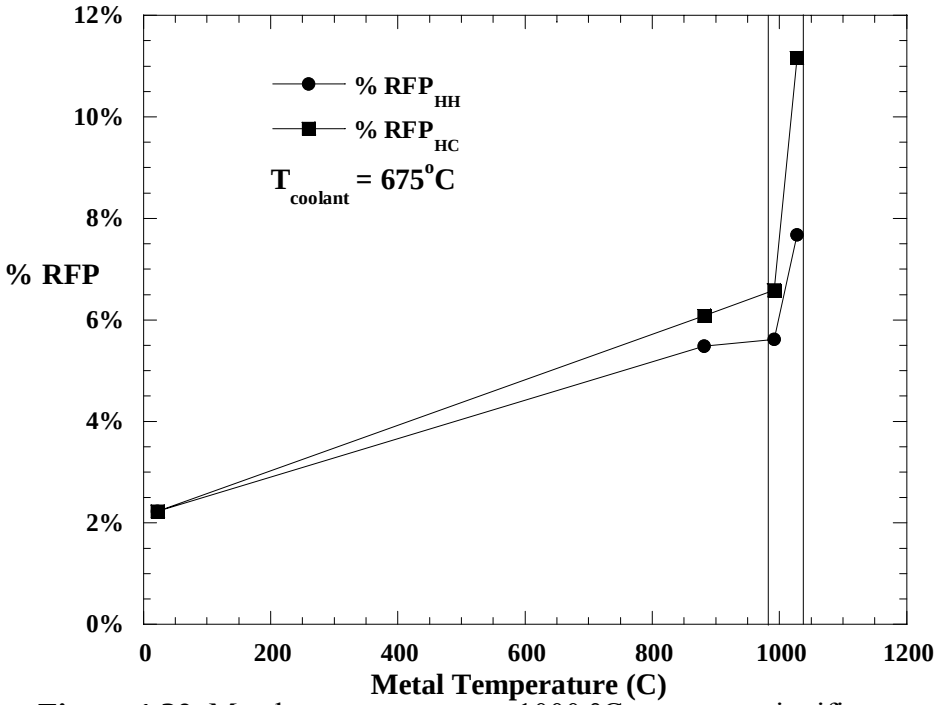

Figure 1.20. Metal temperature over 1000 °C can cause significant enhancement of %RFP (0.5 g ISO Fine, 60-hole coupon, $T_{coolant}$ = 675°C).

Part II. Turbine Blade Results:

Blockage from Sand Ingestion in a Turbine Airfoil with Film-Cooling Holes*

ABSTRACT

Gas turbine engines for propulsion are operated in environments where sand ingestion is sometimes inevitable. This is important because turbine blades are one of the hottest components in the engine, and require internal convective cooling as well as external film-cooling to maintain a low, uniform metal temperature. Sand ingestion into these cooling passages can block critical areas and cause the metal temperature to increase, reducing part life.

This study provided a methodology to test a particular component for its sand blocking characteristics. Sand was injected into three different blades at room temperature including the F-100-229-full, F-100-229-TE, and the F-119 with a trailing edge microcircuit. Sand was also injected and into two different blades at engine metal and coolant temperatures including the F-100-229-TE, and the F-119 with a trailing edge microcircuit.

It was shown that increasing the pressure ratio or mass flow, or decreasing the sand amount injected into a blade would result in lower blockage. It was also shown that above a threshold, the metal and coolant temperature significantly enhanced the blockage. In tests where the metal and coolant temperature were at the design specifications for the F-119 blade, extensive internal melting of the sand resulted in the permanent blockage of two different F-100-229-TE blades. It was also determined that when the F-119 blade was injected with the same amount of sand as the F-100-229-TE blade, it resulted in an average of 2.5 times more blockage.

* To be submitted to Pratt & Whitney as a final contract report.

INTRODUCTION

Propulsive turbine engines operate under harsh conditions including high operating temperatures and ingestion of sand during take-offs and landings particularly in the Middle East. There is a constant drive to increase the turbine inlet temperature to improve engine power output. However, at the same time it is important not to decrease component life. To maintain the component life of these advanced parts, it is necessary to maintain a low, uniform metal temperature throughout the component. Maintaining a low, uniform metal temperature with such high temperature gasses requires complex cooling schemes. The inside of a typical turbine blade includes impingement cooling, ribs in serpentine passages, and pin fins as illustrated in Figure 2.1. The turbine blade external cooling includes showerhead film-cooling, fan-shaped film-cooling holes, tip film-cooling holes, and other film-cooling techniques, as shown in Figure 2.2.

In recent years, a new technology called microcircuits has been introduced that combines film-cooling and internal convective cooling. A microcircuit is a thin passage that exists in the skin of a turbine component, as shown in Figure 2.3. There are several key differences between components with microcircuits and more typical turbine components. The first major difference is that the microcircuit passages are typically smaller, about 0.010 – 0.012 inches (250-300 μm). This is significant considering the sand diameters will range between 0.00016 inches and 0.0091 inches (0.1-230 μm), as illustrated in Figure 2.4. The other major difference between traditional cooling passages and microcircuits is that the metal temperature surrounding the coolant passage is much higher because the passages have less conductive thermal resistance.

It is known that sand ingestion causes a service life reduction in turbine components such as in the field run F-100-229 first stage turbine blade, shown in Figure 2.5, and in the field run V2500 turbine blade, pictured in Figure 2.6. Both of these blades were exposed to sand during in flight engine operation and show sand deposition on the blade surface, as well as at the exit of film-cooling holes. It is also known from testing a Pratt & Whitney F-100-229-full turbine blade that had been under actual flight operation, that significant flow blockage (5-10% RFF_{CC}) has occurred from sand adhering to the internal passages. The question becomes whether sand ingestion is more severe in new cooling schemes, such as microcircuits.

The previous section provided a test methodology and results from a test coupon. While the results from the coupon tests are informative, they do not provide enough information for a comprehensive predictive model for new cooling designs. The major difference between the tests conducted with the test coupon, discussed in the primary portion of this thesis, and tests on turbine blades is the geometry. The coupon had no internal cooling features and consisted of an array of simple laser drilled film-cooling holes. The F-100-229 first stage turbine blades tested consisted of impingement plates, ribbed channels, pin fins, tip cooling holes, fan-shaped film-cooling holes, a leading edge showerhead, and a pressure-side cutaway trailing edge. In addition, the flow passed through four internal channels for the airfoil rather than a plenum cavity as in the coupon. Although each of the channels experiences the same supply pressure, each of the channels has a different flow rate and velocity based on the number of cooling holes and the passage obstructions. The mass flow rates for the 60-hole coupon discussed in the primary portion of this thesis are very similar to the flow rates for the F-100-229-TE blade. Therefore, the geometric differences are the reason that the blocking characteristics of the 60-hole coupon and the F-100-229-TE blade, shown in Figure 2.7, are so different. The blockage for the F-100-229-TE blade is significantly more than the blockage of the 60-hole coupon at the same pressure ratio and sand amount. These differences make it necessary to test actual blades rather than use only results from the coupon.

This section the thesis will cover several topics not addressed in the primary portion of the thesis. The specific objectives for this study will be discussed, followed by a detailed description of the turbine blades that were tested in this portion of the thesis. The test parameters for this portion of the thesis, which are different from those in the primary portion of this thesis are then reviewed. Next, a review of the modified test facility required to test these turbine is discussed, followed by the details of the sand used exclusively for the turbine blades. Finally, the results and conclusions are given.

NOMENCLATURE

%RFF	percent reduction in flow function
D	characteristic diameter
FF	flow function
$\dot{m}$	mass flow
P	pressure
PR	pressure ratio
R	gas constant for air
CFM	standard cubic feet per minute
T	temperature
V	average cooling hole velocity
TE	turbine blade with all holes welded except for the trailing edge
full	turbine blade with no alteration or welding to cooling holes

Greek

Φ	effectiveness
ρ	coolant density
μ	coolant viscosity

Subscripts

0C	total property of the coolant
∞	freestream conditions
CC	cold test – cold baseline
HH	hot test – hot baseline
HC	hot test – cold baseline
metal	property on the surface of the metal
0	Initial property prior to sand injection
0LFE	Total property just prior to the laminar flow element
LFE	Property just prior to the laminar flow element

There were two main objectives that this study was to accomplish. The first objective was to establish a methodology by which turbine components could be tested for sand blockage performance. This methodology was to be used on single components without the rest of the engine. The goal was to simulate the blockage quantified by the flow function (to be defined in a later section) of a field run part by injecting a particular sand amount into a new unused blade. Determining the amount of sand needed to simulate the blockage of a field run part was completed under cold conditions for the F-100-229-Full and F-100-229-TE blades and then those same sand amounts were injected under heated conditions for the F-100-229-TE blade to determine the temperature dependence.

The second objective was to compare a new cooling technology, specifically a microcircuit trailing edge design, to an existing cooling technology, specifically internal and film cooling. This was done by first establishing the amount of sand necessary to simulate a field run F-100-229-TE blade by injecting differing sand amounts into a new F-100-229-TE blade under cold conditions. Again, these sand amounts (one amount for each pressure ratio) were tested under heated conditions on the F-100-229-TE to establish effects of temperature. Finally, these sand amounts were used to test the microcircuit trailing edge design in an F-119 blade under cold and heated conditions. The relative blocking performance between the F-100-229-TE blade and the F-119 blade provided insight into the blocking characteristics of the traditional trailing edge cooling scheme relative to the microcircuit trailing edge cooling scheme.

Blade Descriptions

Several turbine blades were provided by Pratt & Whitney for the tests conducted. The turbine blades provided consisted of seven F-100-229 first stage turbine blades (2 full blades and 5 trailing edge only blades) and one F-119 first stage turbine blade that contained a trailing edge microcircuit design. The field run, first stage F-100-229-full turbine blade shown in Figure 2.8a was in service for a typical component life cycle, and had been subjected to sand ingestion. The surface was roughened from both erosion due to sand impacts and from sand deposition. The leading edge was eroded due to melting from the hot mainstream gases. Many of the film-cooling holes had sand particles in the

diffusion portion of the hole. The trailing edge also had a significant amount of sand deposited into the pressure-side cutaway.

The first stage F-100-229-full turbine blade pictured in Figure 2.8b was identical to the blade pictured in Figure 2.8a except that it had not been operated in an engine. The first stage F-100-229-TE turbine blade pictured in Figure 2.8c was a field run blade similar to Figure 2.8a, except that all of the film cooling holes had been welded shut with the exception of the trailing edge. The F-100-229-TE first stage turbine blade pictured in Figure 2.8d was identical to the blade pictured in Figure 2.8c, except that it had not been operated in an engine. The first stage F-119 turbine blade with a trailing edge microcircuit is shown in Figure 2.8e. This blade has no external features except for the trailing edge microcircuit. Table 2.1 details the serial numbers and the status of each blade provided by Pratt & Whitney.

Test Parameters

To be consistent with standards at Pratt & Whitney, a dimensional form of the flow parameter called the flow function was used. The flow function removes the diameter from the definition of flow parameter. Also, it removes the gas constant R from the equation for simplicity. Therefore, an overall blade averaged flow function was used for these studies, shown in equation 2.1.

$$FF = \frac{\dot{m}\sqrt{T_{0C}}}{P_{0C}} = f(P_{0C} / P_{\infty}, \text{geometry}, T_{0C}) \left[\frac{\text{lb}\sqrt{\text{R}}}{\text{psi}} \right] \tag{2.1}$$

Pratt & Whitney defines the flow function with the pressure downstream of the turbine blade for their cold tests, which is P_{atm} in our testing setup. They also define flow function as the total coolant supply pressure directly upstream of the turbine blade for their heated design, called P_{0C}. The flow function used in this thesis is defined by using the total coolant supply pressure directly upstream of the turbine blade, called P_{0C}. The definition used in this thesis for flow function also uses the measured mass flow of coolant air through the turbine blade, and total coolant supply temperature directly upstream of the turbine blade. The measurement locations for these parameters are shown in Figure 2.9.

The pressure ratio, shown in equation 2.2, is defined as the total coolant pressure upstream of the turbine blade, called P_{0C}, divided by the static pressure downstream of the turbine blade, which was P_{atm} for our testing. For the heated tests, there was no differential between the atmospheric pressure outside the kiln, and the pressure inside the kiln.

$$PR = \frac{P_{0C}}{P_{\infty}} = \frac{P_{0C}}{P_{atm}} \tag{2.2}$$

The baseline flow functions tested by Pratt & Whitney for the F-100-229-full (new and field run) are very close (to within better than 1.0% at each pressure ratio) to the values determined by Virginia Tech, as shown in Figure 2.10. The F-100-229-TE (new and field run) flow function curves also compare very well (to within better than 0.9% at each pressure ratio) to the values determined by Pratt & Whitney, as shown in Figure 2.11. The baseline flow function for each blade was curve fit so that it could be approximated for all pressure ratios. The curve fit of each of these blades was necessary because when sand was introduced into the blade the blockage not only reduced the flow function but also increased the pressure ratio. In addition, because flow function is a function of temperature, another baseline curve was determined and curve fit at engine metal and coolant temperatures for the F-100-229-TE and F-119 blades, as shown in Figure 2.12. These differences are due to changes in viscosity as well as slight cooling-hole expansion that occurs due to heating. The curve fit for all of the baseline heated and unheated flow functions follow the form of equation 2.3 and coefficients for each curve are shown in Table 2.2.

$$FF_0 = C1 \times PR^3 + C2 \times PR^2 + C3 \times PR^2 + C4 \tag{2.3}$$

In this study we are primarily interested in the percent reduction in flow function (%RFF). The percent reduction is a useful way to describe how the flow function changes because of sand blockage. Since either baseline values at cold or heated conditions could be used, it is important to note which baseline is being used for comparison. The percent reduction in flow function, shown in equation 2.4, can be defined several different ways, as will be shown in this thesis.

$$\%RFF = \frac{FF_0 - FF}{FF_0} \tag{2.4}$$

One method is to compare the percent reduction in flow function under cold conditions whereby the cold baseline is used as a reference and only a cold (room temperature) test is conducted. The value for the percent reduction in flow function $\%RFF_{CC}$ (cold sand test – cold baseline) can then be used to estimate the reduction of part life for a given sand flow. Under cold conditions, FF_0 is the baseline flow function at cold conditions and FF is the flow function after sand has clogged the holes.

There are two methods to apply equation 2.4 for heated conditions, illustrated in Figure 2.13. The first method, which will be called $\%RFF_{HH}$ (heated sand test – heated baseline), defines FF_0 as the baseline flow function at heated conditions, and FF as the value of flow function at heated conditions just after the sand is released. The second method, which will be called $\%RFF_{HC}$ (heated test – cold baseline), defines FF_0 as the cold baseline curve fit for that blade, and defines FF as the resulting value after sand has been injected into a heated blade and then the blade returned to room temperature.

TESTING FACILITY AND METHODOLOGY

The main components of the test rig were divided into five basic systems including the coolant supply, sand delivery, kiln, double-pass heat exchanger, and the instrumentation as shown in Figure 2.9. The Virginia Tech Physical Plant provided a constant source of high-pressure air that was used as the coolant as indicated in Figure 2.14. The high-pressure air was routed through a precision pressure-regulating valve with a sensitivity of 0.005 psi (34 Pa) and a maximum flow rate of 10 cfm (0.28 standard cubic meters per min) such that a constant coolant pressure was maintained. Downstream of the pressure regulator, the coolant entered a laminar flow element to measure the coolant mass flow supplied to the blade. The laminar flow element had a maximum flow rate of 40 cfm (1.1 SCMM) and an accuracy of ±0.86% of the actual reading. After the flow exited the laminar flow element, it was routed with standard pipe into a plenum. The plenum was located just upstream of a 0.375 inch thick base plate with a hole milled through it to match the size of the blade root. The base plate was welded to the plenum, and sealed to the blade with a brazing compound manufactured by Pratt and Whitney called Turbofix. The plate had a hole drilled into the side to allow the sand to be introduced via the gravity feed port, as shown in Figure 2.14.

The sand delivery system consisted of a gravity feed port, a valve, and the plate through which the sand-air mixture was delivered to the blade. A ball valve was placed on top of the gravity feed port located far enough outside the kiln so that sand could be safely added while the kiln was heating the blade. The gravity feed port was located as close as possible to the blade to minimize deposits in the coolant supply tube prior to entering the blade. The location chosen was after the plenum, approximately 0.2 inches (0.5 cm) upstream of the blade, as shown in Figure 2.9. Sand amounts were measured to within 0.001 grams of the target value with a Mettler PM200 scale with and accuracy of ± 0.001 grams.

Coolant and metal temperatures are important parameters in the sand blockage and flow function, these temperatures were matched to realistic engine operating conditions. To match the metal and coolant temperatures to the ranges required in the tests, a ceramic kiln with four heater elements was used. The kiln, shown in Figure 2.15, was supplied with 23,500 BTU/h (6.9 kW) of power, to ensure it could raise the temperature inside the kiln to over 2000°F (1090°C) during testing. The kiln had several ports so that different parts of the test rig could protrude through the 3 inch (7.6 cm) firebrick to the outside air. A programmable electronic controller was used to ramp up and to maintain the kiln temperature within ±10°F (± 5°C).

Coolant air traveled through a tube (Inconel 625) and a plenum (stainless steel) before it reached the blade so its temperature depended on the kiln temperature, the heat transfer coefficient inside the supply tube and plenum, and the total plenum surface area exposed to the high kiln air temperature. Without a method of control, the coolant temperature varied significantly based on the mass flow and the exposed plenum surface area. To control the temperature of the coolant, a double-pass heat exchanger was constructed out of steel around the coolant supply tube and plenum, as illustrated in Figure 2.14. The dimensions of the heat exchanger and plenum are shown in Figure 2.16. The heat exchanger was designed so that compressed air could be supplied to it and vented to atmosphere, outside of the kiln to reduce the load on the kiln. With the extra control of the heat exchanger, all of the coolant temperatures and metal temperatures were matched for all pressure ratios and temperature ranges required in this series of tests.

To maintain coolant temperatures while operating lower flow blades such as the F-119, an additional feature was added so that liquid nitrogen could be added to both the coolant air, and the heat exchanger air. This system contained a mixing tube prior to the main coolant flow or heat exchanger flow, as shown in Figure 2.17. The mixing chamber was designed to ensure that no liquid nitrogen entered into the test system, only gaseous nitrogen. The liquid nitrogen mixing chambers were used to protect the instrumentation, and to limit the possibility of thermal shock breaking the welds in the plenum.

Each seal on the plenum and heat exchanger was welded to maintain a hermetic seal during the heated tests. The individual turbine blades could not be sealed easily by welding because they are single crystal. The single crystal has a different coefficient of expansion than metals of similar composition. Therefore, when a weld was attempted, it was very difficult to keep it from cracking during cooling. This cracking presented a problem during heated tests, because the weld could crack during cool down. The blades were sealed with a Pratt & Whitney braze called Turbofix. The high temperatures obtained in the kiln make for a very harsh environment. Corrosion was evident all over the welds and the heat exchanger. Therefore, the welds were consistently checked for cracks and leaks so that they could be patched and a hermetic seal could be maintained.

Instrumentation

A combination of pressure transducers and thermocouples were used to measure several key parameters throughout the test rig including the coolant temperature, pressure ratio, coolant mass flow, and metal temperature of the blade. The thermocouple and pressure probes used to measure the temperature and pressure inside the blade were fed through the coolant supply tube, as shown in Figure 2.9, to protect them from the high kiln temperature. The coolant temperature was monitored with a type K nickel-chrome sheathed thermocouple probe inserted in the flow with the measurement end centered in the plenum. Due to the relatively large area ratio of the plenum to the inlet area of the blade (33:1) and the relatively low velocity, the inside of the plenum the local static pressure could be used as the total pressure measurement. As such, the orientation of the pressure probe was irrelevant, and a simple static pressure probe was fabricated with small gage 0.0625 inch (1.6 mm) diameter Inconel 625 tubing. The tube was inserted

through the coolant supply tube to protect it from the high kiln temperatures and centered in the blade. There was a 5% blockage from the pressure probe in the coolant supply tube.

The metal temperature was unable to be directly measured at heated testing conditions because a thermocouple was unable to be directly mounted onto the blade. As such, the metal temperature was calculated through an effectiveness parameter. Effectiveness is defined in equation 2.5 and is a dimensionless ratio that relates the known temperatures of the kiln air (T_∞) and coolant air (T_{oc}) with the temperature of the metal for different Reynolds numbers.

$$\phi = \frac{T_\infty - T_{metal}}{T_\infty - T_{oc}} \tag{2.5}$$

Effectiveness tests were conducted at temperatures where thermocouples could be attached to the blade. These effectiveness values were then used for the higher temperature tests to deduce the metal temperatures. Effectiveness tests were conducted for a range of Reynolds numbers, defined in equation 2.6, where $\dot{m}$ is the mass flow of coolant through the blade, D is the metering area of the F-100-229 as dictated by Pratt and Whitney (0.040 in^2), and μ is the viscosity of the coolant air.

$$Re = \frac{\rho VD}{\mu} = \frac{4\dot{m}}{D\mu} \tag{2.6}$$

Thermocouples were mounted in two locations along the trailing edge of the F-100-229-TE and the F-119 blades, spaced 0.4 inches (1 cm) away from the ends of the trailing edge and 0.2 inches (0.5 cm) from the trailing edge, as shown in Figure 2.9. The kiln air temperature was also monitored with a type K thermocouple located directly above the blade (away from the cooling). The coolant air was measured with the coolant thermocouple inside the plenum. The blades were tested at two different kiln temperatures (500°F and 1000°F) and several different Reynolds numbers. The metal temperatures measured on the blade surface were within 10°F of each other at all test conditions. Since the difference in temperature between the two thermocouples did not produce a significant difference in the effectiveness, the thermocouple closest to the blade root was used for effectiveness measurements. The results confirmed that the effectiveness was a function of Reynolds number and independent of temperature, as

shown in Figure 2.18 for the F-100-229-TE and Figure 2.19 for the F-119 blade. The effectiveness levels are higher than the coupon because of the additional internal cooling features in the turbine blades. The locations were chosen because they were easily repeatable, and they resulted in determining the blade temperature in the same manner. The dependence on Reynolds number in conjunction with the independence on temperature allowed the effectiveness to be used at all kiln temperatures (T_∞) to deduce the metal temperature of the blade (T_{metal}).

Sand Introduction

The method of sand introduction was important because it was determined that the blade had different blocking characteristics based on the release method. For simplicity and repeatability, a slug flow was used to test the blockage characteristics of the turbine blades. Two methods of creating a slug flow were tested. The first was using an eductor upstream of the blade, and the second was using a gravity feed directly in front of the blade. The results of injecting 0.2 grams of Arizona road dust at room temperature using both sand introduction methods on the F-100-229-full blade are shown in Figure 2.20. Overall, the gravity feed port resulted in a higher $\%RFF_{CC}$ than the eductor for all pressure ratios given the same sand amount. This increased blockage was contributed to the smaller supply tube surface area between the injection location and the blade in the gravity feed design. This reduced surface area reduced the amount of sand that could adhere to the inlet tube before it reached the blade. The gravity feed port was chosen because more of the sand injected into the system entered the blade. The gravity feed sand delivery system was used for all blade tests.

The gravity feed port was operated by placing a measured sand amount inside an airtight section of pipe connected by a valve to a thin base plate directly in front of the turbine blade, as shown in Figure 2.14. When the valve was opened, the sand was released into the opening in the base plate and the coolant air swept the sand into the blade. For a room temperature test, there was a step decrease in flow rate and step increase in pressure ratio, shown in Figure 2.21. After the sand blocked the hole, the flow function and pressure ratio remained at a steady state value. The steady state values of pressure ratio and flow function were then used to deduce the percent flow reduction

(%RFF_{CC}). This %RFF_{CC} was then compared to the %RFF_{CC} between the new and field run blade, shown in Figure 2.22. The closer the values of RFF_{CC} were the better the sand amount simulated the field run part.

As a part of the testing methodology, the moisture content of the sand was minimized. The first reason is that the humidity in the laboratory could not be controlled, and therefore daily variations would have affected the sand adhesion characteristics, as was shown to happen through preliminary testing. The differences in dried and undried sand can be seen by observing the conglomerations evident in Figure 2.23. The second reason to minimize humidity in the sand is that desert regions where sand ingestion is common have very low humidity. The sand was kept in an oven maintained at 400°F (200°C) for at least 4 hours prior to testing to maintain the sand at consistent, low moisture levels.

Prior to all tests, the turbine blades were cleaned until the original baseline flow function / pressure ratio relationship was verified. The turbine blade was cleaned using a combination of compressed air and compressed water when necessary. For cold sand ingestion tests, the baseline flow function was measured at the target pressure ratio, and then dried sand was injected into the system through the gravity feed port. After a few seconds, the system stabilized and remained blocked indefinitely, as was previously indicated. The final flow function and pressure ratio were measured for this steady state condition.

For the heated testing procedures, initially the room temperature baseline flow function / pressure ratio was verified. Then the kiln was turned on and allowed to ramp up to the target temperature with the turbine blade present having its appropriate coolant airflow. After the coolant and metal temperatures were steady and within the desired ranges, dried sand was added to the gravity feed port and injected into the system. The %RFF_{HH} was calculated by taking the flow function just after sand injection and comparing it to the heated baseline flow function for the same ending pressure ratio. The turbine blade was then cooled down to room temperature and another measurement was made at the original pressure ratio and compared to the cold baseline in order to get a %RFF_{HC}.

SAND CHARACTERIZATION

The sand selected by Pratt and Whitney, called Arizona road dust, had similar properties as sand found in desert and arid regions. While sand occurring naturally may have some variation in properties, the sand that was used for testing was chosen because of its consistency. This consistency eliminated sand variation as a possible variable. The sand used in all tests with actual turbine blades was the Arizona road dust. The parameters that were considered important were size distribution, chemical composition, and sand grain density.

Sand diameter is important because in conjunction with sand grain density, it dictates how well the sand will follow streamlines in curved or obstructed passages. The higher the surface area a particle has, the more drag it will have and it will tend to be accelerated by the flow easier. The mean diameter of the Arizona road dust was 0.000933 inches (23.7 μm). The size distribution of the Arizona road dust is shown in Figure 2.24.

The sand grain density is important because it pertains to how well the particles follow the streamlines, and to how much momentum a given particle will have on impact. Small dense particles will not follow streamlines very well. However, large light particles will follow streamlines better. In addition, the small dense particles will tend to impact with more momentum onto the surface increasing the probability that they will rebound and follow the flow rather than sticking. The sand grain density was measured with a pycnometer, with a maximum standard deviation of 0.00018 oz. (0.0051 g). The density for the Arizona road dust, shown in Figure 2.24, is similar to the density of sand used in the primary part of this thesis.

The sand chemical composition was quantified because at the high temperatures that gas turbines operate, it is possible to melt the sand. The composition was qualitatively analyzed with an SEM EDAX system. The raw power spectrum showing the individual element concentrations is shown in Figure 2.25. The analysis for the Arizona road dust was not noticeably different from the other sands tested for the public coupon tests. Since the power spectrums were nearly identical, it can be assumed that the chemical composition is similar to the manufacturer's specifications for the sand tested in the primary portion of this thesis. The manufacturer specifies that the sands tested previously contained different phases of quartz (SiO_2) up to approximately 68-76%,

aluminum oxide (Al_2O_3) between 10-15%, with traces of iron oxide (Fe_2O_3), sodium silicate (Na_2O), lime (CaO), magnesium oxide (MgO), titanium dioxide (TiO_2), and potassium oxide (K_2O), in descending concentration.

The melting point is another parameter that is important for tests where the metal temperature and coolant temperature are at engine conditions. It is known that particle size and chemistry affects the melting point of sand. Figure 2.26 shows Arizona road dust samples after being held at a certain temperature for 30 minutes. The same important conclusion must be drawn as in the primary section of this thesis. If sand is ingested while the engine parts are at or near these high temperatures 1900-2000°F (980-1090°C) severe blocking problems will occur. It is important to note that the F-119 turbine blade with a trailing-edge microcircuit is designed to operate with internal metal temperatures in the middle of this critical temperature range (1800-1900°F).

Assuming that radiation is dominant and assuming a metal temperature of 1850°F, it can be shown that a particle entering a blade at 1200°F can heat up to temperatures where melting occurs within about 0.01 s. By calculating a mean coolant velocity from the known flow properties, and assuming the coolant air takes the minimum path length out of the turbine blade, an estimated residence time was calculated. The estimated residence time for an air molecule through the blade is between 0.0019 s for a pressure ratio of 1.1 and 0.0011 s for a pressure ratio of 1.6. It was also noted that residence time for a particle will be much larger than the residence time of an air molecule through the cooling passages. This is because the particle will impact and reflect off many surfaces, impeding its progress towards the cooling-hole exit. In addition, some coolant air will travel at least twice as much distance through the serpentine passages. Lastly, the maximum relative convective velocity of the particle will be somewhat less than the air, since there will be some viscous loss in the momentum transfer to the particle resulting in a slip velocity.

SAMPLE CALCULATION OF NECESSARY PARAMETERS

This section presents calculations for tests after sand injection under heated conditions for both the F-100-229-TE turbine blade and the F-119 turbine blade. The conditions for the F-100-229-TE test are with a PR=1.4, heated test, 0.41 grams of sand

injected into the blade, and the $\%RFP_{HH}$ is used. The F-119 example below is from a PR=1.4 test, with 0.41 grams of sand injected into the blade with the same $\%RFP_{HH}$ used. There are additional numbers for the post sand tests located in tables numbered 2.9-2.89.

$$\rho_{LFE} = \frac{P_{0LFE}}{RT_{0LFE}}$$

Variable	Units	F-100-229-TE	F-119	Description
ρ_{LFE}	lb/ft^3	0.1005	0.0968	Density before LFE
P_{0LFE}	lb/ft^2	2866.2	2783.0	Total pressure before LFE
R	ft/R	53.33	53.33	
T_{0LFE}	R	534.6	538.2	Total temperature before LFE

$$\mu = b\left(\frac{T_{0LFE}^{1.5}}{T_{0LFE} + S}\right)1x10^{7}$$

Variable	Units	F-100-229-TE	F-119
μ_{LFE}	micropoise	183.2	184.3
b	$\frac{\text{micropoise}}{R^{1/2}}$	1.09E-06	1.09E-06
S	R	198.72	198.72
T_{0LFE}	R	534.6	538.2

$$Q = \left(\frac{dP_{LFE}}{\mu}\right)\left(A_0 + A_1\left(\frac{\rho \bullet dP_{LFE}}{\mu}\right) + A_2\left(\frac{\rho \bullet dP_{LFE}}{\mu}\right)^2\right)$$

Variable	Units	F-100-229-TE	F-119
Volume flow (Q)	CFM	0.6643	0.2006
dP_{LFE}	inH_2O	0.1285	0.0390
μ_{LFE}	micropoise	183.2	184.3
ρ_{LFE}	lb/ft^3	0.1005	0.0969
A_0	$\frac{ft^3\text{- micropoise}}{min - inH_2O}$	948.975	948.975
A_1	$\frac{ft^6\text{- micropoise}^2}{lb - min - inH_2O^2}$	-4773100	-4773100
A_2	$\frac{ft^9\text{- micropoise}^3}{lb^2 - min - inH_2O^3}$	8.04E+10	8.04E+10

$$\dot{m} = V * \rho$$

Variable	Units	F-100-229-TE	F-119
mdot	lb/s	0.00111	0.00032
Volume flow	ft^3/s	0.0111	0.0033
ρ	lb/ft^3	0.1005	0.0969

$$FF = \frac{\dot{m}\sqrt{T_{0C}}}{P_{0C}}$$

Variable	Units	F-100-229-TE	F-119
FF	$\frac{lb\ R^{1/2}}{s\ psi}$	0.00216	0.00060
$\dot{m}$	lb/s	0.00111	0.00032
T_{0C}	R	1424	1316
P_{0C}	psia	19.49	19.32

$$\%RFF = 1 - \frac{FF}{FF_0}$$

Variable	Units	F-100-229-TE	F-119
%RFF	%	23	31
FF	$\frac{lb\ R^{1/2}}{s\ psi}$	0.00216	0.00060
FF_0	$\frac{lb\ R^{1/2}}{s\ psi}$	0.00280	0.00088

$$PR = \frac{P_{0C}}{P_{atm}}$$

Variable	Units	F-100-229-TE	F-119
PR		1.41	1.40
P_{0C}	psia	19.49	19.32
P_{atm}	psia	13.78	13.79

$$Re_D = \frac{4\dot{m}}{\pi D \mu}$$

Variable	Units	F-100-229-TE	F-119
Re_D		982.6	985.9
mdot	lb/s	0.00112436	0.00106
D	ft	0.075	0.075
M	lb/ft-s	1.92E-05	1.84E-05

$$\phi = C_1 Re_D^2 + C_2 Re_D + C_3$$

Variable	F-100-229-TE	F-119
Φ	0.31	0.22
Re_D	982.6	985.9
C_1	0	-1.9157E-09
C_2	0.00003819	0.000049103
C_3	0.26892	0.17373

$$T_{metal} = T_\infty - \phi(T_\infty - T_{0C})$$

	Units	F-100-229-TE	F-119
T_{metal}	F	1659.2	1421.6
T_∞	F	1965.2	1583.6
φ		0.31	0.22
T_{0C}	F	964.4	950

UNCERTAINTY ESTIMATES

An uncertainty analysis was performed on several key parameters using the partial derivative method, and the results of the analysis are shown in Table 2.3. The uncertainty of the pressure ratio was calculated to be 1.1 ± 0.003 and 1.6 ± 0.006. The uncertainty of the flow function was calculated to be between 1.14% for a pressure ratio of 1.6 and 9.48% for a pressure ratio of 1.1 dominated by the bias uncertainty of the

laminar flow element differential pressure transducer. The uncertainty of the %RFF was a maximum under the heated conditions for the F-119 blade at a pressure ratio or 1.1 where the measurement was 8.9 ± 3.4. Under heated conditions, the uncertainty of the metal temperature through the effectiveness method was a maximum at a pressure ratio of 1.1 was calculated to be 1412 ± 13.3°F for the F-119 blade, and 1660 ± 5.4°F for the F-100-229-TE blade. The uncertainty in the sand measured for each test was estimated to be 0.5 ± 0.001g.

A repeatability study was conducted to determine how many identical cases were required to achieve a reasonable confidence interval on the experimental average %RFF. To determine how many tests were required a series of 25 cases with matching pressure ratio and sand amount were conducted at room temperature using the F-100-229 full blade. A 95% confidence interval was calculated from the standard deviation of the averages from each sample size of five samples. It was found that the ideal balance between a small confidence interval and a large number of tests was to conduct three tests at each pressure ratio and sand combination. An example of the raw data points that were used to make up the averaged $\%RFF_{CC}$ measurement are shown in Figure 2.28 for a sand amount of 0.300g at different pressure ratios. This resulted in a confidence interval of 6.9%.

DISCUSSION OF RESULTS

As previously discussed, there were two main objectives to this study. The first objective was to establish a methodology for testing actual turbine components, which included determining sand amounts required to simulate field operated turbine blades with new turbine blades. The second objective was to use those determined sand amounts to evaluate the effects of blade temperature on cooling-hole blockage and to evaluate blockages for a new cooling scheme, namely microcircuits in the trailing edge. Many tests were conducted under heated and unheated conditions with varying pressure ratios, sand amounts, metal temperatures, and coolant temperatures, as detailed in Table 2.4.

Baseline Experimental Results

Baseline results were previously shown in this report in which the purpose was to compare our testing methods with data taken by Pratt & Whitney for new and field operated blades. As such, only a brief discussion will be given in this part of the report regarding the data shown in Figures 2.10 and 2.11.

Tests without sand were conducted on new and field run F-100-229-full and on new and field run F-100-229-TE (test numbers 1-5 in Table 2.4). These tests were conducted at room temperature and at elevated temperatures to establish the baseline flow function vs pressure ratio curve. The baseline flow function vs pressure ratio curve was used in two ways. First, the data for the flow function was used to ensure that the blades were clean prior to testing with sand. Secondly, the flow function vs pressure ratio curve fit was compared to the flow function after sand injection to determine the %RFF at the final pressure ratio.

Figure 2.10 shows the data for the new and field run F-100-229-full blades tested at room temperature while Figure 2.11 shows the data for the new and field run F-100-229-TE blades tested at room temperature. Figures 2.10 and 2.11 indicate that for both the new and field run blades, as the pressure ratio increases, the flow function increases. The increase in flow function with pressure ratio indicates that the mass flow through the blade is not a linear function of total coolant pressure, $P_{0C,}$ which is to be expected based on a simple inviscid analysis.

A curve fit was calculated for both the new and field run components so that $\%RFP_{CC}$ could be calculated at the resulting pressure ratio after sand injection. The curve fit for all of the F-100-229 blades is in the form of equation 2.3. The coefficients for the baseline curve fits for the F-100-229 blades are in Table 2.2. It is important to note that the $\%RFF_{CC}$ between the new and field run F-100-229-full blade, and between the F-100-229-TE new and field run blade, is not constant for all pressure ratios as illustrated in Figure 2.22. The $\%RFF_{CC}$ for the F-100-229-full blade increases from 6% at a pressure ratio of 1.1 to 7.5% at a pressure ratio of 1.6. For the F-100-229-TE blade, the $\%RFF_{CC}$ increased from 5% at a pressure ratio of 1.1 to 9.5% at a pressure ratio of 1.6, as detailed in Table 2.5. This $\%RFF_{CC}$ between the new and field run components was used during

room temperature sand tests to determine how much sand was required to simulate a field run blade by injecting sand into a new blade.

The F-100-229-TE blade was also tested at elevated temperatures to determine a baseline flow function vs pressure ratio curve. This baseline curve was again used to ensure that the flow function was matched at heated conditions just prior to sand injection, and to determine the $\%RFF_{HH}$ after the sand injection. The coolant and metal temperatures used in the baseline test are shown in Table 2.6. The metal temperature ranges chosen for the heated test were intended to represent the metal temperature of a typical F-100-229 blade in field operation, 1650°F ±50°F. The coolant temperature was also chosen to match the range experienced in a field operating F-100-229 blade, 900°F ±50°F.

Figure 2.12 shows the heated baseline flow function vs pressure ratio curve for the F-100-229-TE. Figure 2.12 shows that the heated flow function is significantly less than the room temperature flow function at the same pressure ratio. The lower flow function for the heated blade is due to the increased viscosity of air at those temperatures. The viscosity ratio from room temperature tests (70°F) to the coolant temperature during the heated tests (900°F) is 1.9. This increase from viscosity changes in flow function is in addition to an increase in flow area from thermal expansion of the blade.

Room Temperature Experimental Results

Cold tests, which are tests conducted at room temperature with no external heating or cooling, were completed to determine the basic characteristics of sand blocking without considering temperature. These tests were conducted to determine how much sand was necessary to match the flow function of a field run blade using a new blade. These tests were conducted with a wide range of sand amounts to produce a sand blockage map. This map indicates for a specific pressure ratio and sand amount, how much the flow function will be reduced under cold conditions ($\%RFF_{CC}$). These tests were conducted on the F-100-229-full and the F-100-229-TE and are numbered 6 and 7 in Table 2.4.

The sand injection maps at room temperature for the F-100-229-full blade are shown in Figure 2.27. Many different sand amounts ranging from 1.0 to 3.5 grams were

injected into this component so that the best match of $\%RFF_{CC}$ could be made between the field run and new F-100-229-full blade. Ultimately, the sand amounts that produced sand blockage ($\%RFF_{CC}$) most similar to the F-100-229-full field run part were chosen and are shown in Table 2.7. While the amounts chosen do not perfectly reproduce the target $\%RFF_{CC}$, the results indicate that given time and iteration on the sand amounts, an appropriate amount for each pressure ratio could be found. The sand amounts chosen range from 1.0 grams at a pressure ratio of 1.1 to 3.5 grams at a pressure ratio of 1.5. Testing at an initial pressure ratio of 1.6 was not done since the resulting pressure ratio after sand injection would be well outside the actual operation range as reported by Pratt and Whitney for this particular blade.

The sand injection maps at room temperature for the F-100-229-TE blade are shown in Figure 2.28. The sand amounts chosen to test on the F-100-229-TE are less than the ones chosen for the F-100-229-full blade due to the lower mass flow and the smaller exit area for the F-100-229-TE blade. The sand amounts tested ranged from 0.035 to 0.5 grams and were injected to determine which amounts resulted in the best simulation of $\%RFF_{CC}$ between the field run and new F-100-229-TE blade. The sand amounts that produced sand blockage ($\%RFF_{CC}$) most similar to the F-100-229-TE field run blade are shown in Table 2.6. The sand amounts chosen range from 0.035 grams at a pressure ratio of 1.1 to 0.425 grams at a pressure ratio of 1.6.

Heated Experimental Results

Heated tests, or tests run with elevated metal and coolant temperature, were conducted on the F-100-229-TE to determine whether temperature had any affect on sand blockage of film-cooling holes. The tests were conducted at metal temperatures representative of the F-119 blade initially, and then at lower metal temperatures more representative of the F-100-229 blade to minimize the possibility of damaging the turbine blades being tested. The sand amounts, discussed in the previous section that best simulated the field run flow function reduction at room temperatures were used. After sand was injected, the reduced flow function was compared to the heated baseline flow function to determine the $\%RFF_{HH}$, and compared to the cold baseline flow function after the part had cooled to determine the $\%RFF_{HC}$. These tests, numbered 8, 9, and 10 in

Table 2.4 represent three of the four F-100-229-TE turbine blades given by Pratt and Whitney.

The first heated test of an F-100-229-TE blade, test number 8 in Table 2.4, was conducted at a pressure ratio of 1.6, a metal temperature of 1960°F, and a coolant temperature of 1830°F. The metal temperature in this test was set to a value as hot as possible in hopes of matching the expected metal temperature of the F-119 blade. For this test, however, the coolant temperature was unknown, and more than likely exceeded that found in an engine. The coolant temperature in this initial test was not controlled by the double pass heat exchanger, and it was only after these results were acquired a heat exchanger was determined necessary. The lack of control of the coolant temperature means that the coolant temperature was dictated by the exposed plenum metal area, the kiln temperature, and the convection to the coolant flow. This test, number 8 in Table 2.4, resulted in permanently clogging the blade passages. It is important to note that the blade was damaged because the sand melted and adhered to the inside of the blade and it was not possible to remove the sand.

The next set of heated tests, test 9 in Table 2.4, was conducted on a new F-100-229-TE blade supplied by Pratt and Whitney at a slightly lower metal temperature than before (1830°F) and with a much lower coolant temperature of 1280°F (controlled by using the double-pass heat exchanger). The metal temperature and coolant temperature for this test were selected to match the metal temperature and coolant temperature expected in the F-119 blade under field operation. The first and second heated tests, shown in Figure 2.29, resulted in permanent blockage from the sand. The first test was conducted at a pressure ratio of 1.6, a metal temperature of 1830°F, with 0.425 grams of Arizona road dust injected after steady temperatures had been reached. This resulted in a $\%RFF_{HC}$ of over 50%, which was much higher than had been recorded at room temperature, which was nominally 10%. This permanent blockage was determined to be due to sand melting.

It was determined from previous tests that the metal and coolant temperatures were too high despite the fact that these temperatures were representative of the metal and coolant temperatures expected in the F-119 turbine blade. All subsequent heated tests, number 10 in Table 2.4, were conducted at temperatures more representative of the

F-100-229 blade being tested. Metal temperatures for all heated tests were 1650°F ±50°F, and coolant temperatures were 900°F ±50°F.

Test number 10 in Table 2.4 was conducted to determine the effect of temperature on sand blocking at appropriate temperatures for the F-100-229-TE blade. The actual temperatures for each pressure ratio are illustrated in Figure 2.30, and in Table 2.6. The sand amounts, discussed previously that produced the appropriate $\%RFF_{CC}$, were used under heated conditions, shown in Table 2.6. Figure 2.31 shows that under these heated conditions the $\%RFF_{HH}$ and $\%RFF_{HC}$ were much higher than at room temperature for the same sand amount, also shown in Table 2.6. For a pressure ratio of 1.1 the $\%RFF_{CC}$ was 4.0% the $\%RFF_{HH}$ was 19.3% and the $\%RFF_{HC}$ was 58.7%. For a pressure ratio of 1.6 the $\%RFF_{CC}$ was 10.2% the $\%RFF_{HH}$ was 30.7% and the $\%RFF_{HC}$ was 69.1%.

This much higher $\%RFF_{HH}$ and $\%RFF_{HC}$ for the heated test was most likely due to partial adherence of the sand onto the blade surface. In addition, the difference in the $\%RFF_{HH}$ and the $\%RFP_{HC}$ was most likely due to subsequent conglomeration of the sand after the blade had begun to cool. The reason for these high blockages was that after the sand began to block passages, the flow to the blade was reduced, causing a sudden increase in blade metal temperature. The increase in blade metal temperature happened even though the kiln was almost immediately turned off after the $\%RFF_{HH}$ measurement. The increase in blade metal temperature happened because of the flow reduction due to blockage. The blockage caused an decrease in the heat transfer inside the blade because of the reduction in coolant air.

F-119 Experimental Results

The test results reported up to this point provided the background for the methodology and provided a baseline set of data so that comparisons to new blades could be made. As was described previously, the second objective was to evaluate the sand blockage for a new cooling technology, namely a microcircuit. The F-119 turbine blade with a trailing edge microcircuit was evaluated to determine its relative sand blocking performance to existing turbine blade designs. The F-100-229-TE blade was chosen to compare to because it was a trailing edge only blade and had a mass flow closer to the F-119 blade than the F-100-229-full blade. For comparison, similar tests with the same sand

amounts, were conducted on the F-119 blade as on the F-100-229-TE blade. It is important to note that the F119 blade was a particularly expensive part and as such lower temperatures were tested to ensure that no sand would melt in the part for heated tests.

A room temperature and heated baseline flow function vs pressure ratio curve for the F119 microcircuit was established, shown in Figure 2.11, from which the $\%RFF_{CC}$ and $\%RFF_{HC}$ could be calculated. A heated baseline test, at metal and coolant temperatures indicated in Table 2.8 and shown in Figure 2.32, was conducted so that a $\%RFF_{HH}$ could be calculated. The room temperature and heated flow function was curve fit so that the flow function could be estimated at any pressure ratio. The curve fit followed the form shown in equation 2.3, with coefficients shown in Table 2.2.

Tests at room temperature and elevated temperature were conducted with the same sand amounts chosen in the F-100-229-TE tests, shown in Table 2.8 The results from the room temperature and heated tests are shown in Figure 2.33. The $\%RFF_{CC}$ ranged from 12.0% at a pressure ratio of 1.1 to 28.1% at a pressure ratio of 1.6. For the same sand amounts at each pressure ratio, the $\%RFF_{CC}$ for the F-100-229-TE blade ranged from 4.0% at a pressure ratio of 1.1 to 10.2% at a pressure ratio of 1.6. These higher values for the F119 microcircuit compared to the F-100-229-TE blade was an average of 2.5 times the blockage at a given pressure ratio. The increased blockage of the F-119 blade is because of two differences between the blades. The mass flow rate for the F-119 blade was lower, resulting in less airflow to force the same amount of sand through the blade. The internal geometries for both the blades were also very different. The F-119 blade had a trailing edge microcircuit, with features much smaller than the F-100-229-TE blade.

The heated F-119 tests were conducted at the same coolant temperature range as the F-100-229-TE blade of 900°F ±50°F, however, metal temperatures were determined from a maximum kiln setting of 1500°F. The metal temperature was reduced from the tests with the F-100-229-TE blade in order to minimize the possibility of permanent blockage from sand melting. As such, the metal temperatures ranged from 1400-1430°F, as shown in Figure 2.32. The sand amounts injected are listed in Table 2.8, along with the metal and coolant temperatures for each pressure ratio. The $\%RFP_{HH}$ results for the F-119 blade ranged from 10.4% at a pressure ratio of 1.1 to 28.0% at a pressure ratio of 1.6. The

$\%RFP_{HC}$ results for the F-119 blade ranged from 8.9% at a pressure ratio of 1.1 to 29.1% at a pressure ratio of 1.6. The $\%RFP_{HH}$ and $\%RFP_{HC}$ results for the F-119 blade are nearly the same, unlike the F-100-229-TE blade. The similarities between these two measurements are because of the lower metal temperature at which the F-119 blade was tested, which was about 250°F below the metal temperature the F-100-229-TE blade. The metal temperature in the F-119 blade was not hot enough to initialize melting when sand reduced the mass flow to the blade. Thus, the blockage mechanism for the heated tests was the same as the room temperature tests. The lack of melting in the sand is the same reason that the $\%RFP_{HH}$ and $\%RFP_{HC}$ results for the F-119 blade are closer to the $\%RFP_{CC}$ value of the F-119 blade than they are in the F-100-229-TE blade.

SUMMARY

This section has outlined a new testing methodology by which turbine components or simulated turbine components can be tested to evaluate their sand blockage performance. Understanding these effects is important because gas turbine engines used in propulsive applications are being put into scenarios where ingestion of sand is likely.

The first objective of this thesis was to establish a methodology to test turbine components for their relative sand ingestion performance. The methodology chosen was to inject new turbine blades with sand in a slug fashion to determine the sand amounts that best simulated the reduction in the flow function between a new and field run turbine blade. The difference between the flow function for a new part and the flow function after the sand injection at room temperature was described as a percent reduction in flow function ($\%RFF_{CC}$). The same sand amounts found to best simulate the field run blade at room temperature were injected at heated conditions to determine whether there was an effect of metal temperature. The percent reduction in flow function was evaluated at heated conditions compared to a heated baseline ($\%RFF_{HH}$), and compared to a room temperature baseline after the heated part was returned to room temperature ($\%RFF_{HC}$).

The second objective was to use the methodology we established to compare the blocking performance of two different turbine blades. The two blades selected were the typically used F-100-229-TE and the new F-119 turbine blade with a trailing edge

microcircuit. These blades were selected because a direct comparison of trailing edge cooling schemes was desired. One major difference between the blades was that the F-119 turbine blade has a lower baseline flow function than the F-100-229-TE, as would be expected with a microcircuit design whereby the passages are smaller for the F119 than the F-100-229-TE.

The methodology used in testing worked well to simulate the field run blades with new blades. By using different sand amounts a particular %RFF could be measured, and hence, a certain amount of sand corresponded to a specific %RFF. In addition, simple trends were present throughout the testing and were evident in each of the blades tested at all temperatures. It was determined that more sand for a given pressure ratio will result in more blockage, although the trend is nonlinear. It was also shown that increasing the pressure ratio for a given sand amount would result in less flow blockage. Temperature also plays a major role in determining the sand blockage. It was shown in the F-100-229-TE tests that at a metal temperature of 1800°F, permanent damage could be sustained if sand is ingested. This damage results from sand adhering to the metal surface, and a subsequent local metal temperature increase due to the decrease in coolant flow. The increase in metal temperature causes the sand to melt to the interior metal surfaces causing permanent damage.

It was shown on the F-100-229-TE blade that operating at metal temperatures around 1650°F caused the blockage resulting from sand injection to increase dramatically after the blocking began despite the fact that the kiln was turned off and the part began to cool down. This reduction is likely from the sand forming larger conglomerations after it had adhered to the metal surface. This temperature range does not result in permanent blockage, however, and the sand can be removed. The removal process for the sand ingested at a metal temperature of 1650°F is much more difficult than at room temperature, indicating that if left untreated, the damage would accumulate.

The testing of the F-119 turbine blade was successful and provided information that was used to compare the sand blockage to a part currently in field use. The percent reduction in flow function of the F-119 turbine blade was about 2.5 times higher on average than the F-100-229-TE for the same sand amounts at cold conditions. The higher blockage in the F-119 blade was because of the difference in mass flow and differences

in the passage geometry and pedestal arrangements. For heated conditions, the F-100-229-TE blade was run at higher metal temperatures than the F-119 blade. This higher metal temperature caused the particles of sand to agglomerate. This agglomeration resulted in a much higher reduction in flow function for the F-100-229-TE than for the F119 blade. The metal temperatures for the F-119 blade were below the melting point of the sand, eliminating the effect of melting from the tests. The results from the heated F-119 tests were nearly identical to the results from the room temperature tests, as would be expected since there is no melting. It is important to note that the metal and coolant temperatures for the F-119 tests were significantly lower than the metal temperatures at which the blade was designed to operate. The F-119 blade was tested at a coolant temperature of 900°F and a metal temperature of 1400°F, while the design coolant temperature is 1200°F and the metal temperature would be 1850°F. The combination of higher metal temperatures and more susceptibility to sand blockage could result in a more severe consequence of sand ingestion in field operation for the F119 than conventional blade designs.

It was also noted from testing the F-119 turbine blade at metal temperatures of about 1400°F that little to no difference was measured between the heated and room temperature tests. This was most likely because the metal temperature was below the minimum melting temperature of the sand constituents. This result shows that sand ingestion into the turbine cooling passages will not cause permanent damage with the metal temperature of around 1400°F. The metal temperature for microcircuits is inherently higher than traditional passages, and hence, microcircuits are much more susceptible to permanent sand blockage than traditional cooling passages.

It was found that it is very important to maintain a low metal temperature when sand ingestion occurs or when sand is present in the cooling system. If the turbine is to be operated with metal temperatures exceeding 1500°F, then the turbine must be cleared of all sand to avoid permanent turbine damage. It was also shown that increasing the pressure ratio, decreasing the sand amount, or increasing the mass flow of coolant air results in reduced blockage. The F-119 turbine blade was successfully tested using the methodology described in this thesis, and it was determined that the F-119 turbine blade has an average of 2.5 times more blockage for the same amount of sand. Although it was

not tested, it is apparent that the F-119 turbine blade, when operated within its design metal temperature, would result in permanent damage if sand were to be ingested into the coolant stream.

CONCLUSIONS

Gas turbine engines for propulsion operate in environments where sand ingestion is inevitable. Sand ingested into an engine will flow through the mainstream and through the coolant supply system. The coolant supply system takes relatively low temperature air from the compressor and directs it into the turbine for convective and film-cooling. This convective cooling draws heat away from the blades and other hot section components. Then the coolant air is directed over the surface of the component to provide a protective sheath of cool air called film-cooling. Sand ingestion into the coolant supply will cause blockage and a subsequent reduction in coolant flow. The component will heat up due to the lack of coolant flow and subsequently reduce its part life.

This thesis was divided into two sections, a study on film-cooling holes and a study on turbine blades. The study on film-cooling holes was intended to identify the major factors in sand blocking on a simple array of film-cooling holes at room temperature and at engine temperatures. The study on turbine blades was conducted to establish a testing methodology that could be used to test actual turbine components at room temperature and at engine temperatures. This methodology was then used to compare the blocking characteristics of two different cooling schemes at room temperature and at engine temperatures.

Part I: Public Coupon Results

The first section of this thesis focused on testing coupons with an array of laser drilled film-cooling holes. Several factors were found to control the sand blocking in room temperature tests. It was shown that increasing the pressure ratio, or increased mass flow through an array of holes, resulted in a lower sand blockage. The increased flow reduced blockage because as the pressure ratio is increased the velocity and mass flow of the coolant air would increase. The higher velocity air prevented more sand from adhering to the coolant hole walls. It was also found that as the sand amount increased, the blockage increased. This increased blockage with increased sand amounts was

because with more sand in the flow, there was more available to adhere to the cooling hole walls. Also, with larger sand diameters, more blockage occurred. The increased blockage from a larger sand diameters was because a large sand grain blocks more flow area than a small particle. An increased number of cooling holes had the same effect as increasing the pressure ratio or mass flow. With an increased number of cooling holes the mass flow through the inlet tube was higher. The higher mass flow caused the sand to enter into the coupon at a high velocity and to impact the back wall of the coupon. When the sand impacted the back wall of the coupon, it was knocked out of the flow before it entered into the coolant holes, thus resulting in less blockage.

Metal and coolant temperature were the most important parameters studied in this series of tests. The metal and coolant temperatures tested were representative of the those expected in the F-119 turbine blade. Sand blockage at these temperatures was significantly higher that what was measured at room temperature due to sand melting. When the sand adhered to the surface, it reduced the coolant flow causing an increase in metal temperature. The metal temperature then exceeded the melting point of the sand causing any subsequent particles that contacted that surface to adhere and melt.

To determine if the metal temperature or the coolant temperature was the driving parameter, a temperature variation study was conducted. The first tests held a constant metal temperature and the coolant temperature was increased. When the coolant temperature was increased, only a slight increase in blocking was found. With a constant coolant temperature and an increased metal temperature, significantly more blockage occurred relative to the nominal heated test case. This test indicated that sand blockage is significantly increased above a metal temperature of 1000°C (1830°F).

The tests from section one indicated that there were several important factors to sand blocking. Decreasing the flow rate or pressure ratio, increasing the sand amount or average sand diameter, decreasing the flow area, and increasing the metal temperature all contributed to increased blockage. The most significant finding of this series of tests, however, was that a higher metal temperature causes significantly more blockage.

Part II: Turbine Blade Results

The second part of this thesis focused on testing a methodology by which the relative blocking of turbine blades could be evaluated. In this section, three types of blades were tested including the F-100-229-full, F-100-229-TE, and the F-119 blade with a trailing edge microcircuit.

The first task was to evaluate the blocking performance of the F-100-229-full and F-100-229-TE at room temperature. To evaluate the turbine blades, the flow rate of a new blade was compared to a field run blade, one for each blade type. The intention was to determine the appropriate sand amount necessary to simulate the flow rate of the field run part with the new part. Both blades indicated increased blockage for lower pressure ratios and for larger sand amounts. In addition, because the F-100-229-full blade had a significantly higher flow area, it required much more sand to simulate its field run blade than the F-100-229-TE blade.

The F-100-229-TE was also tested at elevated temperatures to determine what differences could be expected between the cold tests and turbine operation. The initial tests indicated permanent hole blocking occurred because the sand melted and adhered to the internal walls primarily due to elevated and uncontrolled coolant temperatures. Later tests with a new F-100-229-TE blade was run at temperatures intended to match the metal and coolant temperatures in the F-119 blade. This test at a metal temperature of 1850°F and a coolant temperature of 1250°F also resulted in permanent blocking of the blade due to sand melting. Finally tests were conducted at temperatures intended to match the design point of the F-100-229 blade. The metal temperature for this test was 1650°F, and the coolant temperature was 900°F. At the F-100-229 metal temperatures, results indicated significantly higher blockage compared to the room temperature tests. However, after the blade had cooled down, it was possible to clean the blade and restore it to its original flow benchmark. The same blockage trends determined at room temperature were valid under heated conditions; only the levels of the resulting blockage was higher.

The second goal of this section was to compare the blocking characteristics of two blades. The F-119 with a trailing edge microcircuit has little field operation time if any, and therefore, it was desirable to determine how it would react to sand ingestion levels

similar to what a typical F-100-229 blade experiences. Since only the trailing edge of the F-119 blade was opened for cooling exhaust, it was determined that the best comparison would come from the F-100-229-TE blade since it had a similar configuration.

The F-119 blade was tested at room temperature and at elevated temperatures. The heated tests were run at the same coolant temperature as the F-100-229-TE tests (900°F), however a lower metal temperature was used to avoid damaging an extremely expensive part (1400°F). The metal temperatures on the F-119 blade were on average 250°F lower than the F-100-229-TE blade. The results from the room temperature and heated test for the F-119 blade resulted in nearly the same results. The matching of results at room temperature and elevated temperature indicates that below a threshold, temperature is no longer a factor on blockage. The F-119 blade sustained blockage on the average 2.5 times greater than the F-100-229-TE blade. This blockage is expected to be higher at engine operating temperatures because the F-119 blade is designed to operate at higher metal temperatures causing sand to melt and permanently damage the blades.

This thesis has shown the development of a testing methodology used to determine how well a coolant system responds to sand ingestion. It is known that sand ingestion can cause damage to turbine components and subsequently reduce component life. A methodology has been developed by which basic cooling schemes and other simulated components can be tested for blocking characteristics. A second methodology has been developed for testing actual turbine components in a controlled manner to determine which parameters are most important in sand blocking. These tests can also be used to compare several similar turbine component designs to determine which will be less susceptible to damage from sand ingestion.

Recommendations for Future Work

The results from this thesis represent a first attempt at simulating and measuring the impact of sand ingestion. The results were obtained from testing actual turbine components and test coupons under controlled conditions. These controlled conditions represented take-off and landing scenarios found during the operation of turbine engines. The sand injection methods, as well as the sand type, were determined by comparing with field operated turbine components. Future research should focus two fronts. First, more

research should be done to understand what geometric features enhance or reduce blockage. Second, there should be additional effort put into evaluating the effect of rotation and other sand types.

Different turbine components should be analyzed for their susceptibility to sand ingestion. When sand ingestion occurs, it affects the entire engine and therefore all of the hot section components should be tested for susceptibility to sand ingestion. This includes testing the basic geometric features of the component, such as internal cooling channel sizes, rib configurations, cooling hole diameters and placements. Comparisons of these basic tests should be made to actual turbine components. The results from this testing may include ways to reduce the sand blocking, or to limit its impact on cooling performance. In addition, heat transfer studies should be performed on these components so that the severity of the blockage in terms of component life can be estimated.

To better understand how sand blocks turbine blades, rotational effects and additional sand diameters should be tested. Turbine blades rotate at high speeds, and therefore the Coriolis force should be taken into account. This force will cause the sand particles to collect near the tip region of the blade, avoiding the cooling holes near the root of the blade. Natural sand and other dust particulate vary in size, composition, and moisture content. These properties may have an effect on the adhesion properties and should be investigated. Another area that may provide useful information is using a steady flow of sand to produce a blockage. This steady flow of sand may better simulate ingestion scenarios such as aircraft flying through dust storms. Further research must also be done to determine what rates of sand ingestion are typical in actual engine operation.

While this is not a comprehensive list of possible research directions, additional research in these areas may provide insights into the mechanisms of sand blockage. In addition, further study in sand blocking may shed light on methods that could be used to reduce blockage associated with sand ingestion.

Table 2.1. Turbine Components Provided by Pratt & Whitney

Part #	Serial #	Field Run	Pratt Test Data	Description	Status	Figure
P4087101	SKLBDU2734	Yes	Yes	F-100-Full (Field run)	OK	A7.a
P4086701	SKLBEU0265	No	Yes	F-100-Full (New)	OK	A7.b
P4787101	SKLBDU4477	Yes	Yes	F-100-TE (Field run)	OK	A7.c
P4086701	SKLBGW1708	No	Yes	F-100-TE (New)	Clogged	A7.d
P4086901	SKLBJA6113	No	Yes	F-100-TE (New)	Clogged	A7.d
P4086901	SKLBJ44117	No	Yes	F-100-TE (New)	OK	A7.d
P4086901	SKLBJA6513	No	Yes	F-100-TE (New)	OK	A7.d
		No	No	Microcircuit TE	OK	A7.e

Table 2.2. Coefficients for the Baseline Blade Curve Fits

Blade	Status	Temperature	C1	C2	C3	C4
F-100-229-Full	New	Room	0.053004	-0.239556	0.366674	-0.176562
F-100-229-Full	Field Run	Room	0.036022	-0.169701	0.270524	-0.133158
F-100-229-TE	New	Room	0.015974	-0.075655	0.119970	-0.059317
F-100-229-TE	Field Run	Room	0.015202	-0.070911	0.110820	-0.054092
F-119	New	Room	0.006694	-0.033600	0.056949	-0.029286
F-100-229-TE	New	Heated	0.002587	-0.015390	0.031096	-0.017703
F-119	New	Heated	0.007638	-0.032140	0.045778	-0.021263

Table 2.3. Uncertainties of Testing Parameters

	F-100-229-Full		F-100-229-TE				F-119			
	Room		Room		Heated		Room		Heated	
PR	1.1	1.6	1.1	1.6	1.1	1.6	1.1	1.6	1.1	1.6
Tmetal (K)	-	-	-	-	1660 ± 5.4		-	-	1412 ± 13.3	1400 ± 9.7
PR	1.1 ± 0.003	1.6 ± 0.006	1.1 ± 0.003	1.6 ± 0.006	1.1 ± 0.003	1.6 ± 0.006	1.1 ± 0.003	1.6 ± 0.006	1.1 ± 0.003	1.6 ± 0.006
Mass flow	1.20%	1.06%	2.93%	1.69%	8.20%	3.26%	5.15%	3.49%	9.42%	9.47%
FP	1.33%	1.14%	2.99%	1.74%	8.22%	3.28%	5.17%	3.53%	9.42%	9.48%
%RFP	4.7 ± 0.48%	2.0 ± 0.032	2.0 ± 0.88	4.8 ± 0.51	19.3 ± 2.04	30.7 ± 1.23	12.0 ± 0.83%	28.1 ± 1.22%	8.9 ± 3.40%	29.1 ± 3.38%
effectiveness	-	-	-	-	0.28 ± 0.002	0.33 ± 0.002	-	-	0.19 ± 0.004	0.26 ± 0.003
Sand amount	5 ± 0.001 g									
Tcoolant	1°C									

Table 2.4. Turbine Blade Test Matrix

Test #	Blade	SN	Condition	Hot/Cold	PRs	Tmetal (°F)	Tcoolant (°F)	Sand Amts (g)	Figure	Description
1	F-100-229-Full	SKLBEU0265	New	Cold	1.1-1.6	-	-	None	2.10	Baseline
2	F-100-229-Full	SKLBDU2734	Field Run	Cold	1.1-1.6	-	-	None	2.10	Baseline
3	F-100-229-TE	SKLBGW1708	New	Cold	1.1-1.6	-	-	None	2.11	Baseline
4	F-100-229-TE	SKLBDU4477	Field Run	Cold	1.1-1.6	-	-	None	2.11	Baseline
5	F-100-229-TE	SKLBGW1708	New	Heated	1.1-1.6	-	-	None	2.12	Baseline
6	F-100-229-Full	SKLBEU0265	New	Cold	1.1-1.6	-	-	1.000 - 3.500	2.27	Sand Performance Map
7	F-100-229-TE	SKLBGW1708	New	Cold	1.1-1.6	-	-	0.035 - 0.500	2.28	Sand Performance Map
8	F-100-229-TE	SKLBGW1708	New (clogged)	Heated	1.6	1960	1830	0.035 - 0.500	-	Metal temperatures to match F-119
9	F-100-229-TE	SKLBJA6113	New (Clogged)	Heated	1.6	1830	1280	0.035 - 0.500	2.29	Metal and coolant temps to match F-119
10	F-100-229-TE	SKLBJ44117	New	Heated	1.1-1.6	1600-1700	850-950	0.035 - 0.500	2.31	Metal and Coolant temps to match F-100
11	F-119	-	New	Cold	1.1-1.6	-	-	None	2.11	Baseline
12	F-119	-	New	Heated	1.1-1.6	-	-	None	2.12	Baseline
13	F-119	-	New	Cold	1.1-1.6	-	-	0.150 - 0.425	2.33	Sand Performance Comparison
14	F-119	-	New	Heated	1.1-1.6	1400-1500	850-950	0.150 - 0.425	2.33	Metal and coolant temps low (min damage)

Table 2.5. Baseline FP and Target $\%RFP_{CC}$

	Baseline FP				$\%RFP_{CC}$	
	F-100-229-Full		F-100-229-TE		F-100-229	
PR	New	Field Run	New	Field Run	Full	TE
1.1	0.007434	0.006981	0.002350	0.002234	6.09%	4.95%
1.2	0.010113	0.009475	0.003308	0.003078	6.31%	6.95%
1.3	0.011648	0.010869	0.003876	0.003532	6.69%	8.89%
1.4	0.012649	0.011742	0.004185	0.003774	7.17%	9.83%
1.5	0.013389	0.012368	0.004330	0.003901	7.63%	9.90%
1.6	0.013907	0.012807	0.004384	0.003953	7.91%	9.82%

Table 2.6. Sand Amounts and Temperatures for F-100-229-TE Tests

PR	Sand needed to mimic Field	$\%RFF_{CC}$ Target	$\%RFF_{CC}$ Tested	Coolant Temperature (°F)	Metal Temperature (°F)	$\%RFF_{HH}$ Tested	$\%RFF_{HC}$ Tested
Target	**N/A**	**-**	**-**	**900± 50**	**1650 ± 50**	**-**	**-**
1.1	0.035	4.95	3.99	900	1650	19.3	58.67
1.2	0.15	6.95	9.28	900	1650	26.35	57.56
1.3	0.3	8.89	9.26	930	1650	30.79	59.64
1.4	0.41	9.83	10.1	930	1640	25.44	64.84
1.5	0.425	9.9	11.27	-	-	-	-
1.6	0.425	9.82	10.23	900	1600	30.68	69.08

Table 2.7. Sand Amounts and Temperatures for F-100-229-full Tests

PR	Sand needed to mimic Field Run part (g)	$\%RFF_{CC}$ Target	$\%RFF_{CC}$ Tested
1.1	1.000	6.09	4.71
1.2	2.000	6.31	4.06
1.3	2.500	6.69	6.59
1.4	3.000	7.17	5.48
1.5	3.000	7.63	5.72
1.6	3.000	7.91	

Table 2.8. Sand Amounts and Temperatures for F-100-229-TE Tests

PR	Sand needed to mimic Field	$\%RFF_{CC}$ Tested	Coolant Temperature (°F)	Metal Temperature (°F)	$\%RFF_{HH}$ Tested	$\%RFF_{HC}$ Tested
Target	**N/A**	**-**	**900± 50**	**1400 ± 50**	**-**	**-**
1.1	0.035	3.99	903	1400	10.42	8.88
1.2	0.15	9.28	897	1407	17.01	16.92
1.3	0.3	9.26	897	1414	18.44	21.42
1.4	0.41	10.1	892	1430	25.80	25.93
1.5	0.425	11.27	-	-	-	-
1.6	0.425	10.23	897	1400	28.05	29.13

F-100-229-FULL %RFP$_{CC}$ TESTS IN FIGURE 2.27

Table 2.9. F-100-229-full, %RFP$_{CC}$, Arizona Test Dust, 1.0 Gram, PR 1.1

Run #	P_{atm} psia	P_{OC} psia	PR -	Toc R	mdot lb/s	FP lb $T^{0.5}$ / psia	FP_0 lb $T^{0.5}$ / psia	%RFP
1	13.72	15.21	1.11	529.3	0.00485	0.00733	0.00772	5.02%
2	13.70	15.18	1.11	529.3	0.00482	0.00730	0.00772	5.46%
3	13.70	15.13	1.10	529.3	0.00482	0.00733	0.00761	3.65%
Average	13.71	15.18	1.11	529.3	0.00483	0.00732	0.00768	4.71%

Table 2.10. F-100-229-full, %RFP$_{CC}$, Arizona Test Dust, 1.0 Gram, PR 1.2

Run #	P_{atm} psia	P_{OC} psia	PR -	Toc R	mdot lb/s	FP lb $T^{0.5}$ / psia	FP_0 lb $T^{0.5}$ / psia	%RFP
1	13.72	16.59	1.21	529.8	0.00724	0.01004	0.01022	1.80%
2	13.70	16.51	1.21	529.5	0.00721	0.01005	0.01016	1.07%
3	13.70	16.55	1.21	529.3	0.00717	0.00997	0.01021	2.36%
Average	13.71	16.55	1.21	529.5	0.00721	0.01002	0.01020	1.75%

Table 2.11. F-100-229-full, %RFP$_{CC}$, Arizona Test Dust, 1.0 Gram, PR 1.3

Run #	P_{atm} psia	P_{OC} psia	PR -	Toc R	mdot lb/s	FP lb $T^{0.5}$ / psia	FP_0 lb $T^{0.5}$ / psia	%RFP
1	13.72	17.93	1.31	529.6	0.00908	0.01165	0.01177	1.07%
2	13.70	17.94	1.31	529.1	0.00902	0.01157	0.01182	2.11%
3	13.70	17.91	1.31	528.9	0.00902	0.01158	0.01178	1.72%
Average	13.71	17.93	1.31	529.2	0.00904	0.01160	0.01179	1.63%

Table 2.12. F-100-229-full, %RFP$_{CC}$, Arizona Test Dust, 1.0 Gram, PR 1.4

Run #	P_{atm} psia	P_{OC} psia	PR -	Toc R	mdot lb/s	FP lb $T^{0.5}$ / psia	FP_0 lb $T^{0.5}$ / psia	%RFP
1	13.72	19.33	1.41	528.9	0.01057	0.01258	0.01275	1.35%
2	13.70	19.31	1.41	528.9	0.01054	0.01255	0.01276	1.67%
3	13.70	19.28	1.41	529.1	0.01045	0.01247	0.01274	2.14%
Average	13.71	19.31	1.41	528.9	0.01052	0.01253	0.01275	1.72%

Table 2.13. F-100-229-full, %RFP$_{CC}$, Arizona Test Dust, 1.0 Gram, PR 1.55

Run #	P_{atm} psia	P_{OC} psia	PR -	Toc R	mdot lb/s	FP lb $T^{0.5}$ / psia	FP_0 lb $T^{0.5}$ / psia	%RFP
1	13.77	21.53	1.56	532.4	0.01254	0.01344	0.01369	1.87%
2	13.77	21.52	1.56	531.8	0.01263	0.01353	0.01369	1.15%
3	13.77	21.73	1.58	532.4	0.01258	0.01336	0.01378	3.07%
Average	13.77	21.59	1.57	532.2	0.01258	0.01344	0.01372	2.03%

Table 2.14. F-100-229-full, $\%RFP_{CC}$, Arizona Test Dust, 1.5 Grams, PR 1.1

Run #	P_{atm} psia	P_{OC} psia	PR -	Toc R	mdot lb/s	FP lb $T^{0.5}$ / psia	FP_0 lb $T^{0.5}$ / psia	%RFP
1	13.70	15.35	1.12	529.5	0.00469	0.00703	0.00809	13.04%
2	13.72	15.36	1.12	529.4	0.00480	0.00719	0.00804	10.61%
3	13.70	15.30	1.12	529.4	0.00476	0.00716	0.00797	10.25%
Average	13.71	15.34	1.12	529.4	0.00475	0.00713	0.00803	11.30%

Table 2.15. F-100-229-full, $\%RFP_{CC}$, Arizona Test Dust, 1.5 Grams, PR 1.2

Run #	P_{atm} psia	P_{OC} psia	PR -	Toc R	mdot lb/s	FP lb $T^{0.5}$ / psia	FP_0 lb $T^{0.5}$ / psia	%RFP
1	13.72	16.63	1.21	529.7	0.00716	0.00991	0.01029	3.65%
2	13.70	16.63	1.21	529.3	0.00713	0.00986	0.01034	4.60%
3	13.70	16.61	1.21	529.1	0.00719	0.00995	0.01031	3.46%
Average	13.71	16.63	1.21	529.3	0.00716	0.00991	0.01031	3.90%

Table 2.16. F-100-229-full, $\%RFP_{CC}$, Arizona Test Dust, 1.5 Grams, PR 1.3

Run #	P_{atm} psia	P_{OC} psia	PR -	Toc R	mdot lb/s	FP lb $T^{0.5}$ / psia	FP_0 lb $T^{0.5}$ / psia	%RFP
1	13.72	17.99	1.31	529.0	0.00906	0.01158	0.01182	2.07%
2	13.70	18.00	1.31	528.8	0.00899	0.01149	0.01186	3.17%
3	13.70	18.00	1.31	528.8	0.00896	0.01145	0.01186	3.46%
Average	13.71	17.99	1.31	528.9	0.00900	0.01151	0.01185	2.90%

Table 2.17. F-100-229-full, $\%RFP_{CC}$, Arizona Test Dust, 1.5 Grams, PR 1.4

Run #	P_{atm} psia	P_{OC} psia	PR -	Toc R	mdot lb/s	FP lb $T^{0.5}$ / psia	FP_0 lb $T^{0.5}$ / psia	%RFP
1	13.70	19.40	1.42	528.9	0.01057	0.01254	0.01280	2.11%
2	13.70	19.29	1.41	528.8	0.01056	0.01259	0.01275	1.24%
3	13.72	19.40	1.41	528.7	0.01055	0.01250	0.01279	2.26%
Average	13.71	19.36	1.41	528.8	0.01056	0.01254	0.01278	1.87%

Table 2.18. F-100-229-full, $\%RFP_{CC}$, Arizona Test Dust, 2.0 Grams, PR 1.1

Run #	P_{atm} psia	P_{OC} psia	PR -	Toc R	mdot lb/s	FP lb $T^{0.5}$ / psia	FP_0 lb $T^{0.5}$ / psia	%RFP
1	13.62	15.18	1.11	528.4	0.00481	0.00728	0.00791	8.00%
2	13.62	15.45	1.13	528.3	0.00473	0.00703	0.00848	17.08%
3	13.62	15.47	1.14	529.2	0.00472	0.00701	0.00853	17.81%
Average	13.62	15.37	1.13	528.6	0.00475	0.00711	0.00831	14.29%

Table 2.19. F-100-229-full, $\%RFP_{CC}$, Arizona Test Dust, 2.0 Grams, PR 1.2

Run #	P_{atm} psia	P_{OC} psia	PR -	Toc R	mdot lb/s	FP lb $T^{0.5}$ / psia	FP_0 lb $T^{0.5}$ / psia	%RFP
1	13.70	16.67	1.22	528.8	0.00720	0.00994	0.01038	4.30%
2	13.70	16.61	1.21	528.6	0.00720	0.00996	0.01031	3.41%
3	13.70	16.68	1.22	528.5	0.00721	0.00993	0.01040	4.47%
Average	13.70	16.65	1.22	528.6	0.00720	0.00994	0.01036	4.06%

Table 2.20. F-100-229-full, $\%RFP_{CC}$, Arizona Test Dust, 2.0 Grams, PR 1.3

Run #	P_{atm} psia	P_{OC} psia	PR -	Toc R	mdot lb/s	FP lb $T^{0.5}$ / psia	FP_0 lb $T^{0.5}$ / psia	%RFP
1	13.70	18.00	1.31	529.1	0.00896	0.01145	0.01187	3.51%
2	13.70	18.08	1.32	529.1	0.00897	0.01141	0.01194	4.38%
3	13.70	18.04	1.32	529.1	0.00896	0.01143	0.01190	3.94%
Average	13.70	18.04	1.32	529.1	0.00896	0.01143	0.01190	3.95%

Table 2.21. F-100-229-full, $\%RFP_{CC}$, Arizona Test Dust, 2.0 Grams, PR 1.4

Run #	P_{atm} psia	P_{OC} psia	PR -	Toc R	mdot lb/s	FP lb $T^{0.5}$ / psia	FP_0 lb $T^{0.5}$ / psia	%RFP
1	13.70	19.36	1.41	529.2	0.01054	0.01252	0.01279	2.06%
2	13.70	19.45	1.42	528.9	0.01052	0.01244	0.01283	3.04%
3	13.70	19.44	1.42	529.0	0.01050	0.01243	0.01283	3.13%
Average	13.70	19.42	1.42	529.1	0.01052	0.01246	0.01282	2.74%

Table 2.22. F-100-229-full, $\%RFP_{CC}$, Arizona Test Dust, 2.5 Grams, PR 1.1

Run #	P_{atm} psia	P_{OC} psia	PR -	Toc R	mdot lb/s	FP lb $T^{0.5}$ / psia	FP_0 lb $T^{0.5}$ / psia	%RFP
1	13.70	15.94	1.16	529.7	0.00457	0.00659	0.00924	28.65%
2	13.70	15.90	1.16	529.5	0.00458	0.00663	0.00917	27.71%
3	13.70	15.90	1.16	529.5	0.00459	0.00664	0.00916	27.50%
Average	13.70	15.92	1.16	529.5	0.00458	0.00662	0.00919	27.95%

Table 2.23. F-100-229-full, $\%RFP_{CC}$, Arizona Test Dust, 2.5 Grams, PR 1.2

Run #	P_{atm} psia	P_{OC} psia	PR -	Toc R	mdot lb/s	FP lb $T^{0.5}$ / psia	FP_0 lb $T^{0.5}$ / psia	%RFP
1	13.72	17.17	1.25	529.7	0.00716	0.00959	0.01099	12.68%
2	13.70	17.07	1.25	529.4	0.00708	0.00954	0.01091	12.61%
3	13.70	16.85	1.23	529.2	0.00710	0.00969	0.01064	8.97%
Average	13.71	17.03	1.24	529.4	0.00711	0.00960	0.01085	11.42%

Table 2.24. F-100-229-full, $\%RFP_{CC}$, Arizona Test Dust, 2.5 Grams, PR 1.3

Run #	P_{atm} psia	P_{OC} psia	PR -	Toc R	mdot lb/s	FP lb $T^{0.5}$ / psia	FP_0 lb $T^{0.5}$ / psia	%RFP
1	13.72	18.18	1.32	529.3	0.00898	0.01137	0.01199	5.16%
2	13.70	18.32	1.34	529.3	0.00892	0.01120	0.01213	7.65%
3	13.70	18.34	1.34	529.4	0.00901	0.01130	0.01214	6.96%
Average	13.71	18.28	1.33	529.3	0.00897	0.01129	0.01209	6.59%

Table 2.25. F-100-229-full, $\%RFP_{CC}$, Arizona Test Dust, 2.5 Grams, PR 1.4

Run #	P_{atm} psia	P_{OC} psia	PR -	Toc R	mdot lb/s	FP lb $T^{0.5}$ / psia	FP_0 lb $T^{0.5}$ / psia	%RFP
1	13.72	19.76	1.44	529.6	0.01057	0.01231	0.01297	5.06%
2	13.70	19.48	1.42	529.5	0.01055	0.01246	0.01285	2.98%
3	13.70	19.52	1.43	529.4	0.01056	0.01245	0.01287	3.27%
Average	13.71	19.59	1.43	529.5	0.01056	0.01241	0.01290	3.77%

Table 2.26. F-100-229-full, $\%RFP_{CC}$, Arizona Test Dust, 2.5 Grams, PR 1.55

Run #	P_{atm} psia	P_{OC} psia	PR -	Toc R	mdot lb/s	FP lb $T^{0.5}$ / psia	FP_0 lb $T^{0.5}$ / psia	%RFP
1	13.72	21.71	1.58	532.7	0.01248	0.01326	0.01381	3.96%
2	13.72	21.71	1.58	532.7	0.01249	0.01328	0.01381	3.88%
3	13.72	21.75	1.59	534.5	0.01253	0.01332	0.01383	3.68%
Average	13.72	21.72	1.58	533.3	0.01250	0.01329	0.01382	3.84%

Table 2.27. F-100-229-full, $\%RFP_{CC}$, Arizona Test Dust, 3.0 Grams, PR 1.3

Run #	P_{atm} psia	P_{OC} psia	PR -	Toc R	mdot lb/s	FP lb $T^{0.5}$ / psia	FP_0 lb $T^{0.5}$ / psia	%RFP
1	13.68	19.15	1.40	531.3	0.00888	0.01069	0.01269	15.77%
2	13.68	18.68	1.37	530.9	0.00891	0.01099	0.01240	11.36%
3	13.68	18.77	1.37	531.0	0.00890	0.01093	0.01246	12.29%
Average	13.68	18.87	1.38	531.1	0.00890	0.01087	0.01252	13.14%

Table 2.28. F-100-229-full, $\%RFP_{CC}$, Arizona Test Dust, 3.0 Grams, PR 1.4

Run #	P_{atm} psia	P_{OC} psia	PR -	Toc R	mdot lb/s	FP lb $T^{0.5}$ / psia	FP_0 lb $T^{0.5}$ / psia	%RFP
1	13.68	19.98	1.46	531.0	0.01049	0.01210	0.01310	7.60%
2	13.68	19.93	1.46	530.8	0.01045	0.01208	0.01308	7.59%
3	13.68	20.07	1.47	531.4	0.01046	0.01201	0.01314	8.61%
Average	13.68	19.99	1.46	531.1	0.01047	0.01207	0.01311	7.93%

Table 2.29. F-100-229-full, %RFP_{CC}, Arizona Test Dust, 3.0 Grams, PR 1.5

Run #	P_{atm}	P_{OC}	PR	Toc	mdot	FP	FP_0	%RFP
	psia	psia	-	R	lb/s	lb $T^{0.5}$ / psia	lb $T^{0.5}$ / psia	
1	13.66	21.17	1.55	530.5	0.01193	0.01298	0.01361	4.66%
2	13.66	21.14	1.55	530.4	0.01184	0.01290	0.01360	5.16%
3	13.66	21.37	1.56	530.6	0.01187	0.01280	0.01370	6.61%
Average	13.66	21.23	1.55	530.5	0.01188	0.01289	0.01364	5.48%

Table 2.30. F-100-229-full, %RFP_{CC}, Arizona Test Dust, 3.0 Grams, PR 1.55

Run #	P_{atm}	P_{OC}	PR	Toc	mdot	FP	FP_0	%RFP
	psia	psia	-	R	lb/s	lb $T^{0.5}$ / psia	lb $T^{0.5}$ / psia	
1	13.77	22.06	1.60	531.3	0.01253	0.01309	0.01394	6.08%
2	13.77	22.02	1.60	530.6	0.01262	0.01321	0.01392	5.12%
3	13.77	22.02	1.60	531.1	0.01251	0.01309	0.01392	5.95%
Average	13.77	22.03	1.60	531.0	0.01256	0.01313	0.01393	5.72%

Table 2.31. F-100-229-full, %RFP_{CC}, Arizona Test Dust, 3.5 Grams, PR 1.3

Run #	P_{atm}	P_{OC}	PR	Toc	mdot	FP	FP_0	%RFP
	psia	psia	-	R	lb/s	lb $T^{0.5}$ / psia	lb $T^{0.5}$ / psia	
1	13.66	19.25	1.41	531.2	0.00885	0.01060	0.01276	16.95%
2	13.66	19.10	1.40	531.5	0.00884	0.01067	0.01268	15.79%
3	13.66	19.00	1.39	531.5	0.00884	0.01072	0.01262	15.03%
Average	13.66	19.12	1.40	531.4	0.00884	0.01066	0.01268	15.92%

Table 2.32. F-100-229-full, %RFP_{CC}, Arizona Test Dust, 3.5 Grams, PR 1.5

Run #	P_{atm}	P_{OC}	PR	Toc	mdot	FP	FP_0	%RFP
	psia	psia	-	R	lb/s	lb $T^{0.5}$ / psia	lb $T^{0.5}$ / psia	
1	13.66	22.51	1.65	531.6	0.01183	0.01211	0.01429	15.20%
2	13.66	21.91	1.60	531.5	0.01223	0.01286	0.01396	7.82%
3	13.66	22.06	1.62	531.4	0.01185	0.01238	0.01403	11.80%
Average	13.66	22.16	1.62	531.5	0.01197	0.01245	0.01409	11.60%

F-100-229-TE %RFP_{CC} TESTS IN FIGURE 2.28

Table 2.33. F-100-229-TE, %RFP_{CC}, Arizona Test Dust, 0.035 Grams, PR 1.1

Run #	P_{atm}	P_{OC}	PR	Toc	mdot	FP	FP_0	%RFP
	psia	psia	-	R	lb/s	lb $T^{0.5}$ / psia	lb $T^{0.5}$ / psia	
1	13.64	14.93	1.09	533.3	0.00147	0.00227	0.00239	5.01%
2	13.64	14.97	1.10	533.3	0.00153	0.00237	0.00242	2.25%
3	13.64	14.94	1.09	533.4	0.00148	0.00228	0.00240	4.71%
Average	13.64	14.95	1.10	533.3	0.00149	0.00231	0.00731	3.99%

Table 2.34. F-100-229-TE, $\%RFP_{CC}$, Arizona Test Dust, 0.040 Grams, PR 1.1

Run #	P_{atm} psia	P_{OC} psia	PR -	Toc R	mdot lb/s	FP lb $T^{0.5}$ / psia	FP_0 lb $T^{0.5}$ / psia	%RFP
1	13.79	15.13	1.10	534.9	0.00141	0.00216	0.00242	10.75%
2	13.79	15.21	1.10	535.1	0.00153	0.00233	0.00248	6.09%
3	13.79	15.23	1.10	534.7	0.00154	0.00234	0.00249	6.12%
Average	13.79	15.19	1.10	534.9	0.00149	0.00227	0.00749	7.65%

Table 2.35. F-100-229-TE, $\%RFP_{CC}$, Arizona Test Dust, 0.050 Grams, PR 1.1

Run #	P_{atm} psia	P_{OC} psia	PR -	Toc R	mdot lb/s	FP lb $T^{0.5}$ / psia	FP_0 lb $T^{0.5}$ / psia	%RFP
1	13.85	15.35	1.11	536.8	0.00153	0.00231	0.00253	8.72%
2	13.85	15.27	1.10	537.1	0.00149	0.00227	0.00247	8.37%
3	13.85	15.38	1.11	536.8	0.00150	0.00226	0.00256	11.49%
Average	13.85	15.33	1.11	536.9	0.00151	0.00228	0.00767	9.53%

Table 2.36. F-100-229-TE, $\%RFP_{CC}$, Arizona Test Dust, 0.050 Grams, PR 1.2

Run #	P_{atm} psia	P_{OC} psia	PR -	Toc R	mdot lb/s	FP lb $T^{0.5}$ / psia	FP_0 lb $T^{0.5}$ / psia	%RFP
1	13.85	16.60	1.20	536.9	0.00232	0.00324	0.00330	1.57%
2	13.85	16.57	1.20	536.6	0.00232	0.00325	0.00328	1.08%
3	13.85	16.56	1.20	536.6	0.00232	0.00324	0.00328	1.09%
Average	13.85	16.58	1.20	536.7	0.00232	0.00324	0.00999	1.25%

Table 2.37. F-100-229-TE, $\%RFP_{CC}$, Arizona Test Dust, 0.100 Grams, PR 1.1

Run #	P_{atm} psia	P_{OC} psia	PR -	Toc R	mdot lb/s	FP lb $T^{0.5}$ / psia	FP_0 lb $T^{0.5}$ / psia	%RFP
1	13.85	15.20	1.10	537.7	0.00132	0.00201	0.00242	16.99%
2	13.85	15.19	1.10	537.2	0.00141	0.00216	0.00241	10.64%
3	13.85	15.32	1.11	537.1	0.00145	0.00219	0.00251	12.89%
Average	13.85	15.23	1.10	537.3	0.00139	0.00212	0.00746	13.51%

Table 2.38. F-100-229-TE, $\%RFP_{CC}$, Arizona Test Dust, 0.100 Grams, PR 1.2

Run #	P_{atm} psia	P_{OC} psia	PR -	Toc R	mdot lb/s	FP lb $T^{0.5}$ / psia	FP_0 lb $T^{0.5}$ / psia	%RFP
1	13.85	16.69	1.21	536.6	0.00226	0.00313	0.00334	6.39%
2	13.85	16.61	1.20	536.9	0.00231	0.00323	0.00330	2.34%
3	13.85	16.66	1.20	536.8	0.00227	0.00315	0.00333	5.33%
Average	13.85	16.66	1.20	536.8	0.00228	0.00317	0.01011	4.69%

Table 2.39. F-100-229-TE, %RFP_{CC}, Arizona Test Dust, 0.150 Grams, PR 1.2

Run #	P_{atm} psia	P_{OC} psia	PR -	Toc R	mdot lb/s	FP lb $T^{0.5}$ / psia	FP_0 lb $T^{0.5}$ / psia	%RFP
1	13.64	16.59	1.22	532.2	0.00215	0.00299	0.00341	12.49%
2	13.64	16.35	1.20	532.4	0.00229	0.00323	0.00330	2.04%
3	13.64	16.62	1.22	532.7	0.00214	0.00297	0.00342	13.31%
Average	13.64	16.52	1.21	532.4	0.00219	0.00306	0.01027	9.28%

Table 2.40. F-100-229-TE, %RFP_{CC}, Arizona Test Dust, 0.200 Grams, PR 1.1

Run #	P_{atm} psia	P_{OC} psia	PR -	Toc R	mdot lb/s	FP lb $T^{0.5}$ / psia	FP_0 lb $T^{0.5}$ / psia	%RFP
1	13.85	15.50	1.12	536.4	0.00128	0.00192	0.00264	27.35%
2	13.85	15.38	1.11	536.6	0.00137	0.00207	0.00255	18.93%
3	13.85	15.35	1.11	536.7	0.00144	0.00217	0.00254	14.59%
Average	13.85	15.41	1.11	536.6	0.00137	0.00205	0.00785	20.29%

Table 2.41. F-100-229-TE, %RFP_{CC}, Arizona Test Dust, 0.200 Grams, PR 1.2

Run #	P_{atm} psia	P_{OC} psia	PR -	Toc R	mdot lb/s	FP lb $T^{0.5}$ / psia	FP_0 lb $T^{0.5}$ / psia	%RFP
1	13.85	16.87	1.22	536.4	0.00213	0.00292	0.00343	14.79%
2	13.85	16.95	1.22	536.2	0.00206	0.00282	0.00346	18.52%
3	13.85	16.58	1.20	536.3	0.00232	0.00325	0.00329	1.15%
Average	13.85	16.80	1.21	536.3	0.00217	0.00299	0.01031	11.49%

Table 2.42. F-100-229-TE, %RFP_{CC}, Arizona Test Dust, 0.200 Grams, PR 1.3

Run #	P_{atm} psia	P_{OC} psia	PR -	Toc R	mdot lb/s	FP lb $T^{0.5}$ / psia	FP_0 lb $T^{0.5}$ / psia	%RFP
1	13.85	18.08	1.31	536.5	0.00292	0.00374	0.00387	3.37%
2	13.85	18.30	1.32	536.3	0.00289	0.00365	0.00394	7.17%
3	13.85	18.42	1.33	536.3	0.00290	0.00365	0.00397	7.98%
Average	13.85	18.26	1.32	536.4	0.00290	0.00368	0.01192	6.17%

Table 2.43. F-100-229-TE, %RFP_{CC}, Arizona Test Dust, 0.200 Grams, PR 1.4

Run #	P_{atm} psia	P_{OC} psia	PR -	Toc R	mdot lb/s	FP lb $T^{0.5}$ / psia	FP_0 lb $T^{0.5}$ / psia	%RFP
1	13.85	19.43	1.40	535.2	0.00343	0.00409	0.00417	1.98%
2	13.85	19.40	1.40	535.9	0.00345	0.00412	0.00417	1.18%
3	13.85	19.68	1.42	535.8	0.00332	0.00390	0.00421	7.40%
Average	13.85	19.50	1.41	535.7	0.00340	0.00404	0.01275	3.52%

Table 2.44. F-100-229-TE, $\%RFP_{CC}$, Arizona Test Dust, 0.300 Grams, PR 1.1

Run #	P_{atm} psia	P_{OC} psia	PR -	Toc R	mdot lb/s	FP lb $T^{0.5}$ / psia	FP_0 lb $T^{0.5}$ / psia	%RFP
1	13.72	15.88	1.16	535.3	0.00138	0.00201	0.00299	32.62%
2	13.72	15.32	1.12	535.2	0.00143	0.00216	0.00262	17.68%
3	13.72	15.47	1.13	535.5	0.00146	0.00219	0.00273	19.67%
Average	13.72	15.56	1.13	535.3	0.00142	0.00212	0.00847	23.32%

Table 2.45. F-100-229-TE, $\%RFP_{CC}$, Arizona Test Dust, 0.300 Grams, PR 1.2

Run #	P_{atm} psia	P_{OC} psia	PR -	Toc R	mdot lb/s	FP lb $T^{0.5}$ / psia	FP_0 lb $T^{0.5}$ / psia	%RFP
1	13.72	16.62	1.21	535.9	0.00220	0.00306	0.00338	9.65%
2	13.86	16.84	1.21	536.4	0.00213	0.00293	0.00340	13.81%
3	13.86	17.15	1.24	536.3	0.00181	0.00245	0.00354	30.87%
Average	13.81	16.87	1.22	536.2	0.00205	0.00281	0.01047	18.11%

Table 2.46. F-100-229-TE, $\%RFP_{CC}$, Arizona Test Dust, 0.300 Grams, PR 1.3

Run #	P_{atm} psia	P_{OC} psia	PR -	Toc R	mdot lb/s	FP lb $T^{0.5}$ / psia	FP_0 lb $T^{0.5}$ / psia	%RFP
1	13.72	17.94	1.31	535.2	0.00287	0.00370	0.00389	4.79%
2	13.72	18.67	1.36	535.0	0.00296	0.00367	0.00407	9.80%
3	13.72	18.18	1.33	534.5	0.00270	0.00343	0.00395	13.20%
Average	13.72	18.27	1.33	534.9	0.00284	0.00360	0.01206	9.26%

Table 2.47. F-100-229-TE, $\%RFP_{CC}$, Arizona Test Dust, 0.300 Grams, PR 1.4

Run #	P_{atm} psia	P_{OC} psia	PR -	Toc R	mdot lb/s	FP lb $T^{0.5}$ / psia	FP_0 lb $T^{0.5}$ / psia	%RFP
1	13.86	19.54	1.41	536.1	0.00332	0.00393	0.00419	6.23%
2	13.86	19.49	1.41	536.2	0.00336	0.00399	0.00418	4.48%
3	13.72	22.17	1.62	531.2	0.00391	0.00406	0.00443	8.30%
Average	13.81	20.40	1.48	534.5	0.00353	0.00400	0.01319	6.34%

Table 2.48. F-100-229-TE, $\%RFP_{CC}$, Arizona Test Dust, 0.300 Grams, PR 1.5

Run #	P_{atm} psia	P_{OC} psia	PR -	Toc R	mdot lb/s	FP lb $T^{0.5}$ / psia	FP_0 lb $T^{0.5}$ / psia	%RFP
1	13.72	20.86	1.52	536.7	0.00368	0.00408	0.00435	6.17%
2	13.86	20.89	1.51	536.7	0.00373	0.00414	0.00434	4.60%
3	13.86	20.93	1.51	536.3	0.00372	0.00411	0.00434	5.25%
Average	13.81	20.89	1.51	536.5	0.00371	0.00411	0.01340	5.34%

Table 2.49. F-100-229-TE, $\%RFP_{CC}$, Arizona Test Dust, 0.300 Grams, PR 1.6

Run #	P_{atm} psia	P_{OC} psia	PR -	Toc R	mdot lb/s	FP lb $T^{0.5}$ / psia	FP_0 lb $T^{0.5}$ / psia	%RFP
1	13.72	21.95	1.60	535.3	0.00411	0.00433	0.00442	1.99%
2	13.86	22.54	1.63	536.9	0.00401	0.00412	0.00444	7.09%
3	13.86	22.51	1.62	536.8	0.00408	0.00420	0.00444	5.32%
Average	13.81	22.33	1.62	536.3	0.00407	0.00422	0.01404	4.80%

Table 2.50. F-100-229-TE, $\%RFP_{CC}$, Arizona Test Dust, 0.400 Grams, PR 1.2

Run #	P_{atm} psia	P_{OC} psia	PR -	Toc R	mdot lb/s	FP lb $T^{0.5}$ / psia	FP_0 lb $T^{0.5}$ / psia	%RFP
1	13.90	17.18	1.24	540.4	0.00196	0.00265	0.00353	24.92%
2	13.86	16.89	1.22	540.3	0.00204	0.00281	0.00343	17.98%
3	13.86	16.98	1.22	540.1	0.00198	0.00272	0.00347	21.70%
Average	13.88	17.02	1.23	540.3	0.00200	0.00273	0.01056	21.53%

Table 2.51. F-100-229-TE, $\%RFP_{CC}$, Arizona Test Dust, 0.400 Grams, PR 1.3

Run #	P_{atm} psia	P_{OC} psia	PR -	Toc R	mdot lb/s	FP lb $T^{0.5}$ / psia	FP_0 lb $T^{0.5}$ / psia	%RFP
1	13.90	18.34	1.32	540.5	0.00278	0.00352	0.00393	10.37%
2	13.86	18.35	1.32	540.6	0.00272	0.00345	0.00394	12.45%
3	13.86	18.40	1.33	540.5	0.00271	0.00342	0.00396	13.58%
Average	13.88	18.36	1.32	540.6	0.00274	0.00346	0.01197	12.13%

Table 2.52. F-100-229-TE, $\%RFP_{CC}$, Arizona Test Dust, 0.400 Grams, PR 1.4

Run #	P_{atm} psia	P_{OC} psia	PR -	Toc R	mdot lb/s	FP lb $T^{0.5}$ / psia	FP_0 lb $T^{0.5}$ / psia	%RFP
1	13.90	19.92	1.43	540.7	0.00324	0.00378	0.00423	10.74%
2	13.86	19.72	1.42	540.5	0.00331	0.00390	0.00422	7.40%
3	13.86	19.84	1.43	540.4	0.00326	0.00382	0.00423	9.81%
Average	13.88	19.83	1.43	540.5	0.00327	0.00383	0.01289	9.32%

Table 2.53. F-100-229-TE, $\%RFP_{CC}$, Arizona Test Dust, 0.400 Grams, PR 1.5

Run #	P_{atm} psia	P_{OC} psia	PR -	Toc R	mdot lb/s	FP lb $T^{0.5}$ / psia	FP_0 lb $T^{0.5}$ / psia	%RFP
1	13.90	21.05	1.51	537.3	0.00376	0.00414	0.00434	4.82%
2	13.86	21.30	1.54	537.6	0.00358	0.00390	0.00437	10.77%
3	13.86	21.05	1.52	537.7	0.00370	0.00407	0.00435	6.33%
Average	13.88	21.13	1.52	537.5	0.00368	0.00403	0.01346	7.31%

Table 2.54. F-100-229-TE, %RFP_{CC}, Arizona Test Dust, 0.400 Grams, PR 1.6

Run #	P_{atm} psia	P_{OC} psia	PR -	Toc R	mdot lb/s	FP lb $T^{0.5}$ / psia	FP_0 lb $T^{0.5}$ / psia	%RFP
1	13.90	22.83	1.64	536.5	0.00410	0.00416	0.00445	6.51%
2	13.86	22.46	1.62	536.7	0.00400	0.00413	0.00443	6.93%
3	13.86	22.61	1.63	537.0	0.00391	0.00401	0.00444	9.81%
Average	13.88	22.63	1.63	536.7	0.00400	0.00410	0.01415	7.75%

Table 2.55. F-100-229-TE, %RFP_{CC}, Arizona Test Dust, 0.410 Grams, PR 1.4

Run #	P_{atm} psia	P_{OC} psia	PR -	Toc R	mdot lb/s	FP lb $T^{0.5}$ / psia	FP_0 lb $T^{0.5}$ / psia	%RFP
1	13.64	19.52	1.43	532.0	0.00319	0.00377	0.00423	10.91%
2	13.64	19.43	1.42	532.4	0.00323	0.00383	0.00422	9.08%
3	13.64	19.49	1.43	532.5	0.00320	0.00379	0.00423	10.33%
Average	13.64	19.48	1.43	532.3	0.00321	0.00380	0.01289	10.11%

Table 2.56. F-100-229-TE, %RFP_{CC}, Arizona Test Dust, 0.450 Grams, PR 1.3

Run #	P_{atm} psia	P_{OC} psia	PR -	Toc R	mdot lb/s	FP lb $T^{0.5}$ / psia	FP_0 lb $T^{0.5}$ / psia	%RFP
1	13.85	18.78	1.36	536.7	0.00253	0.00312	0.00405	22.89%
2	13.85	18.55	1.34	536.7	0.00269	0.00336	0.00400	16.13%
3	13.85	18.60	1.34	536.8	0.00263	0.00328	0.00401	18.24%
Average	13.85	18.64	1.35	536.7	0.00262	0.00325	0.01221	19.09%

Table 2.57. F-100-229-TE, %RFP_{CC}, Arizona Test Dust, 0.450 Grams, PR 1.4

Run #	P_{atm} PSI	P_{OC} PSI	PR -	Toc R	mdot lb/s	FP lb $T^{0.5}$ / psia	FP_0 lb $T^{0.5}$ / psia	%RFP
1	13.97	20.26	1.45	535.5	0.00311	0.00355	0.00426	16.70%
2	13.97	20.07	1.44	535.3	0.00322	0.00371	0.00424	12.56%
3	13.85	19.82	1.43	537.3	0.00302	0.00353	0.00423	16.59%
Average	13.93	20.05	1.44	536.0	0.00311	0.00360	0.01296	15.28%

Table 2.58. F-100-229-TE, %RFP_{CC}, Arizona Test Dust, 0.450 Grams, PR 1.5

Run #	P_{atm} psia	P_{OC} psia	PR -	Toc R	mdot lb/s	FP lb $T^{0.5}$ / psia	FP_0 lb $T^{0.5}$ / psia	%RFP
1	13.97	21.50	1.54	534.9	0.00362	0.00389	0.00437	10.84%
2	13.97	21.82	1.56	535.2	0.00343	0.00364	0.00439	17.10%
3	13.97	21.98	1.57	535.2	0.00334	0.00352	0.00440	19.99%
Average	13.97	21.77	1.56	535.1	0.00346	0.00368	0.01366	15.98%

Table 2.59. F-100-229-TE, $\%RFP_{CC}$, Arizona Test Dust, 0.450 Grams, PR 1.6

Run #	P_{atm} psia	P_{OC} psia	PR -	Toc R	mdot lb/s	FP lb $T^{0.5}$ / psia	FP_0 lb $T^{0.5}$ / psia	%RFP
1	13.97	22.50	1.61	534.9	0.00410	0.00422	0.00443	4.67%
2	13.97	23.53	1.68	535.0	0.00353	0.00347	0.00449	22.82%
3	13.97	23.10	1.65	535.0	0.00380	0.00380	0.00446	14.71%
Average	13.97	23.04	1.65	535.0	0.00381	0.00382	0.01430	14.07%

Table 2.60. F-100-229-TE, $\%RFP_{CC}$, Arizona Test Dust, 0.500 Grams, PR 1.3

Run #	P_{atm} psia	P_{OC} psia	PR -	Toc R	mdot lb/s	FP lb $T^{0.5}$ / psia	FP_0 lb $T^{0.5}$ / psia	%RFP
1	13.71	18.79	1.37	535.5	0.00233	0.00287	0.00410	29.99%
2	13.71	18.80	1.37	535.4	0.00230	0.00284	0.00410	30.78%
3	13.71	18.42	1.34	535.4	0.00258	0.00325	0.00401	19.09%
Average	13.71	18.67	1.36	535.4	0.00241	0.00298	0.01236	26.62%

Table 2.61. F-100-229-TE, $\%RFP_{CC}$, Arizona Test Dust, 0.500 Grams, PR 1.4

Run #	P_{atm} psia	P_{OC} psia	PR -	Toc R	mdot lb/s	FP lb $T^{0.5}$ / psia	FP_0 lb $T^{0.5}$ / psia	%RFP
1	13.82	19.96	1.44	536.4	0.00306	0.00355	0.00425	16.56%
2	13.82	20.27	1.47	536.5	0.00290	0.00331	0.00429	22.78%
3	13.71	19.98	1.46	534.6	0.00302	0.00349	0.00427	18.32%
Average	13.78	20.07	1.46	535.9	0.00299	0.00345	0.01307	19.22%

Table 2.62. F-100-229-TE, $\%RFP_{CC}$, Arizona Test Dust, 0.500 Grams, PR 1.5

Run #	P_{atm} psia	P_{OC} psia	PR -	Toc R	mdot lb/s	FP lb $T^{0.5}$ / psia	FP_0 lb $T^{0.5}$ / psia	%RFP
1	13.82	21.26	1.54	535.1	0.00359	0.00391	0.00437	10.58%
2	13.82	21.94	1.59	535.6	0.00319	0.00337	0.00441	23.59%
3	13.72	21.83	1.59	536.2	0.00320	0.00340	0.00441	22.98%
Average	13.79	21.67	1.57	535.7	0.00333	0.00355	0.01375	19.05%

Table 2.63. F-100-229-TE, $\%RFP_{CC}$, Arizona Test Dust, 0.500 Grams, PR 1.6

Run #	P_{atm} psia	P_{OC} psia	PR -	Toc R	mdot lb/s	FP lb $T^{0.5}$ / psia	FP_0 lb $T^{0.5}$ / psia	%RFP
1	13.82	23.17	1.68	535.6	0.00358	0.00358	0.00448	20.15%
2	13.82	22.48	1.63	535.2	0.00403	0.00414	0.00444	6.65%
3	13.82	23.31	1.69	535.4	0.00349	0.00346	0.00449	22.98%
Average	13.82	22.99	1.66	535.4	0.00370	0.00372	0.01441	16.59%

F-100-229-TE HEATED TESTS IN FIGURE 2.31

Table 2.64. F-100-229-TE, $\%RFP_{HH}$, Arizona Test Dust, 0.035 Grams, PR 1.1

Run #	P_{atm} psia	P_{OC} psia	PR -	Toc R	mdot lb/s	FP lb $T^{0.5}$ / psia	FP_0 lb $T^{0.5}$ / psia	%RFP
1	13.82	23.17	1.68	535.6	0.00358	0.00358	0.00448	20.15%
2	13.82	22.48	1.63	535.2	0.00403	0.00414	0.00444	6.65%
3	13.82	23.31	1.69	535.4	0.00349	0.00346	0.00449	22.98%
Average	13.82	22.99	1.66	535.4	0.00370	0.00372	0.01441	16.59%

Table 2.65. F-100-229-TE, $\%RFP_{HH}$, Arizona Test Dust, 0.150 Grams, PR 1.2

Run #	P_{atm} psia	P_{OC} psia	PR -	Toc R	mdot lb/s	FP lb $T^{0.5}$ / psia	FP_0 lb $T^{0.5}$ / psia	%RFP
1	13.78	16.68	1.21	1427.7	0.00069	0.00156	0.00201	22.03%
2	13.78	16.43	1.19	1416.4	0.00065	0.00149	0.00191	22.09%
3	13.78	16.70	1.21	1459.9	0.00057	0.00131	0.00201	34.91%
Average	13.78	16.60	1.20	1434.7	0.00064	0.00145	0.01014	26.35%

Table 2.66. F-100-229-TE, $\%RFP_{HH}$, Arizona Test Dust, 0.300 Grams, PR 1.3

Run #	P_{atm} psia	P_{OC} psia	PR -	Toc R	mdot lb/s	FP lb $T^{0.5}$ / psia	FP_0 lb $T^{0.5}$ / psia	%RFP
1	13.78	18.06	1.31	1447.5	0.00085	0.00179	0.00246	27.43%
2	13.78	18.04	1.31	1391.7	0.00081	0.00167	0.00245	31.99%
3	13.78	18.09	1.31	1460.1	0.00078	0.00165	0.00247	32.97%
Average	13.78	18.06	1.31	1433.1	0.00081	0.00170	0.01182	30.79%

Table 2.67. F-100-229-TE, $\%RFP_{HH}$, Arizona Test Dust, 0.410 Grams, PR 1.4

Run #	P_{atm} psia	P_{OC} psia	PR -	Toc R	mdot lb/s	FP lb $T^{0.5}$ / psia	FP_0 lb $T^{0.5}$ / psia	%RFP
1	13.78	19.49	1.41	1424.4	0.00111	0.00216	0.00280	23.08%
2	13.78	19.45	1.41	1425.9	0.00104	0.00202	0.00280	27.73%
3	13.73	19.44	1.42	1481.7	0.00106	0.00209	0.00281	25.52%
Average	13.76	19.46	1.41	1444.0	0.00107	0.00209	0.01279	25.44%

Table 2.68. F-100-229-TE, $\%RFP_{HH}$, Arizona Test Dust, 0.425 Grams, PR 1.6

Run #	P_{atm} psia	P_{OC} psia	PR -	Toc R	mdot lb/s	FP lb $T^{0.5}$ / psia	FP_0 lb $T^{0.5}$ / psia	%RFP
1	13.63	22.27	1.63	1481.7	0.00128	0.00222	0.00332	33.22%
2	13.63	22.05	1.62	1385.6	0.00160	0.00270	0.00328	17.80%
3	13.78	22.66	1.64	1511.2	0.00115	0.00197	0.00334	41.02%
Average	13.68	22.33	1.63	1459.5	0.00134	0.00230	0.01416	30.68%

Table 2.69. F-100-229-TE, $\%RFP_{HC}$, Arizona Test Dust, 0.035 Grams, PR 1.1

Run #	P_{atm} psia	P_{OC} psia	PR -	Toc R	mdot lb/s	FP lb $T^{0.5}$ / psia	FP_0 lb $T^{0.5}$ / psia	%RFP
1	13.78	15.16	1.10	536.3	0.00040	0.00061	0.00245	74.93%
2	13.78	15.21	1.10	545.7	0.00086	0.00132	0.00248	46.70%
3	13.78	15.18	1.10	536.8	0.00074	0.00112	0.00246	54.39%
Average	13.78	15.18	1.10	539.6	0.00067	0.00102	0.00750	58.67%

Table 2.70. F-100-229-TE, $\%RFP_{HC}$, Arizona Test Dust, 0.150 Grams, PR 1.2

Run #	P_{atm} psia	P_{OC} psia	PR -	Toc R	mdot lb/s	FP lb $T^{0.5}$ / psia	FP_0 lb $T^{0.5}$ / psia	%RFP
1	13.78	16.52	1.20	540.2	0.00079	0.00111	0.00329	66.34%
2	13.78	16.50	1.20	536.1	0.00108	0.00151	0.00328	54.03%
3	13.78	16.52	1.20	542.5	0.00112	0.00157	0.00330	52.30%
Average	13.78	16.51	1.20	539.6	0.00099	0.00140	0.01000	57.56%

Table 2.71. F-100-229-TE, $\%RFP_{HC}$, Arizona Test Dust, 0.300 Grams, PR 1.3

Run #	P_{atm} psia	P_{OC} psia	PR -	Toc R	mdot lb/s	FP lb $T^{0.5}$ / psia	FP_0 lb $T^{0.5}$ / psia	%RFP
1	13.78	17.92	1.30	542.4	0.00158	0.00205	0.00385	46.83%
2	13.78	17.91	1.30	542.0	0.00119	0.00154	0.00385	59.89%
3	13.78	17.92	1.30	536.8	0.00083	0.00107	0.00385	72.22%
Average	13.78	17.92	1.30	540.4	0.00120	0.00155	0.01169	59.64%

Table 2.72. F-100-229-TE, $\%RFP_{HC}$, Arizona Test Dust, 0.410 Grams, PR 1.4

Run #	P_{atm} psia	P_{OC} psia	PR -	Toc R	mdot lb/s	FP lb $T^{0.5}$ / psia	FP_0 lb $T^{0.5}$ / psia	%RFP
1	13.78	19.30	1.40	536.3	0.00090	0.00108	0.00417	74.10%
2	13.78	19.30	1.40	537.2	0.00136	0.00164	0.00417	60.70%
3	13.73	19.22	1.40	537.9	0.00139	0.00168	0.00417	59.71%
Average	13.76	19.28	1.40	537.1	0.00122	0.00147	0.01269	64.84%

Table 2.73. F-100-229-TE, $\%RFP_{HC}$, Arizona Test Dust, 0.425 Grams, PR 1.6

Run #	P_{atm} psia	P_{OC} psia	PR -	Toc R	mdot lb/s	FP lb $T^{0.5}$ / psia	FP_0 lb $T^{0.5}$ / psia	%RFP
1	13.63	21.82	1.60	540.0	0.00169	0.00180	0.00442	59.19%
2	13.63	21.88	1.61	532.2	0.00143	0.00151	0.00442	65.87%
3	13.78	22.07	1.60	534.8	0.00075	0.00079	0.00442	82.18%
Average	13.68	21.92	1.60	535.7	0.00129	0.00136	0.01394	69.08%

F-119 ROOM TEMPERATURE AND HEATED TESTS IN FIGURE 2.33

Table 2.74. F-119, $\%RFP_{CC}$, Arizona Test Dust, 0.035 Grams, PR 1.1

Run #	P_{atm} psia	P_{OC} psia	PR -	Toc R	mdot lb/s	FP lb $T^{0.5}$ / psia	FP_0 lb $T^{0.5}$ / psia	%RFP
1	13.70	15.31	1.12	537.0	0.00092	0.00140	0.00161	13.13%
2	13.70	15.28	1.12	536.8	0.00093	0.00141	0.00160	12.04%
3	13.70	15.35	1.12	538.3	0.00096	0.00145	0.00163	10.91%
Average	13.70	15.31	1.12	537.3	0.00094	0.00142	0.00801	12.03%

Table 2.75. F-119, $\%RFP_{CC}$, Arizona Test Dust, 0.150 Grams, PR 1.2

Run #	P_{atm} psia	P_{OC} psia	PR -	Toc R	mdot lb/s	FP lb $T^{0.5}$ / psia	FP_0 lb $T^{0.5}$ / psia	%RFP
1	13.70	17.09	1.25	536.5	0.00137	0.00186	0.00226	17.85%
2	13.70	16.97	1.24	536.9	0.00136	0.00186	0.00222	16.45%
3	13.70	16.97	1.24	537.9	0.00142	0.00195	0.00222	12.41%
Average	13.70	17.01	1.24	537.1	0.00139	0.00189	0.01084	15.57%

Table 2.76. F-119, $\%RFP_{CC}$, Arizona Test Dust, 0.300 Grams, PR 1.3

Run #	P_{atm} psia	P_{OC} psia	PR -	Toc R	mdot lb/s	FP lb $T^{0.5}$ / psia	FP_0 lb $T^{0.5}$ / psia	%RFP
1	13.70	20.04	1.46	536.9	0.00166	0.00192	0.00288	33.48%
2	13.70	19.70	1.44	535.2	0.00170	0.00200	0.00283	29.40%
3	13.70	18.37	1.34	532.9	0.00181	0.00228	0.00259	11.87%
Average	13.70	19.37	1.41	535.0	0.00172	0.00206	0.01279	24.92%

Table 2.77. F-119, $\%RFP_{CC}$, Arizona Test Dust, 0.410 Grams, PR 1.4

Run #	P_{atm} psia	P_{OC} psia	PR -	Toc R	mdot lb/s	FP lb $T^{0.5}$ / psia	FP_0 lb $T^{0.5}$ / psia	%RFP
1	13.70	22.61	1.65	536.7	0.00219	0.00224	0.00310	27.77%
2	13.70	21.28	1.55	536.7	0.00203	0.00221	0.00302	26.69%
3	13.70	21.57	1.58	535.4	0.00202	0.00216	0.00304	28.84%
Average	13.70	21.82	1.59	536.3	0.00208	0.00221	0.01388	27.76%

Table 2.78. F-119, $\%RFP_{CC}$, Arizona Test Dust, 0.425 Grams, PR 1.6

Run #	P_{atm} psia	P_{OC} psia	PR -	Toc R	mdot lb/s	FP lb $T^{0.5}$ / psia	FP_0 lb $T^{0.5}$ / psia	%RFP
1	13.70	22.73	1.66	533.5	0.00220	0.00223	0.00311	28.11%
2	13.70	23.00	1.68	535.4	0.00228	0.00229	0.00312	26.50%
3	13.70	23.27	1.70	532.5	0.00222	0.00220	0.00312	29.70%
Average	13.70	23.00	1.68	533.8	0.00223	0.00224	0.01456	28.10%

Table 2.79. F-119, $\%RFP_{HH}$, Arizona Test Dust, 0.035 Grams, PR 1.1

Run #	P_{atm} psia	P_{OC} psia	PR -	Toc R	mdot lb/s	FP lb $T^{0.5}$ / psia	FP_0 lb $T^{0.5}$ / psia	%RFP
1	13.79	15.18	1.10	1310.7	0.00013	0.00032	0.00037	15.01%
2	13.72	15.11	1.10	1351.7	0.00014	0.00034	0.00038	8.33%
3	13.72	15.09	1.10	1366.7	0.00014	0.00034	0.00037	7.92%
Average	13.74	15.13	1.10	1343.0	0.00014	0.00033	0.00748	10.42%

Table 2.80. F-119, $\%RFP_{HH}$, Arizona Test Dust, 0.150 Grams, PR 1.2

Run #	P_{atm} psia	P_{OC} psia	PR -	Toc R	mdot lb/s	FP lb $T^{0.5}$ / psia	FP_0 lb $T^{0.5}$ / psia	%RFP
1	13.79	16.64	1.21	1365.0	0.00021	0.00047	0.00058	18.35%
2	13.79	16.64	1.21	1342.6	0.00023	0.00051	0.00058	11.71%
3	13.79	16.56	1.20	1343.5	0.00020	0.00045	0.00057	20.97%
Average	13.79	16.61	1.20	1350.4	0.00022	0.00048	0.01014	17.01%

Table 2.81. F-119, $\%RFP_{HH}$, Arizona Test Dust, 0.300 Grams, PR 1.3

Run #	P_{atm} psia	P_{OC} psia	PR -	Toc R	mdot lb/s	FP lb $T^{0.5}$ / psia	FP_0 lb $T^{0.5}$ / psia	%RFP
1	13.79	17.92	1.30	1370.1	0.00029	0.00060	0.00073	17.15%
2	13.79	17.96	1.30	1399.4	0.00029	0.00061	0.00073	16.46%
3	13.79	17.95	1.30	1373.7	0.00028	0.00057	0.00073	21.71%
Average	13.79	17.95	1.30	1381.1	0.00029	0.00059	0.01171	18.44%

Table 2.82. F-119, $\%RFP_{HH}$, Arizona Test Dust, 0.410 Grams, PR 1.4

Run #	P_{atm} psia	P_{OC} psia	PR -	Toc R	mdot lb/s	FP lb $T^{0.5}$ / psia	FP_0 lb $T^{0.5}$ / psia	%RFP
1	13.79	19.32	1.40	1315.7	0.00032	0.00061	0.00087	30.50%
2	13.79	19.05	1.38	1348.5	0.00034	0.00066	0.00085	22.29%
3	13.79	19.36	1.40	1346.6	0.00035	0.00066	0.00088	24.60%
Average	13.79	19.24	1.40	1336.9	0.00034	0.00064	0.01265	25.80%

Table 2.83. F-119, $\%RFP_{HH}$, Arizona Test Dust, 0.425 Grams, PR 1.6

Run #	P_{atm} psia	P_{OC} psia	PR -	Toc R	mdot lb/s	FP lb $T^{0.5}$ / psia	FP_0 lb $T^{0.5}$ / psia	%RFP
1	13.65	21.88	1.60	1381.8	0.00054	0.00092	0.00127	27.64%
2	13.65	21.87	1.60	1345.2	0.00048	0.00080	0.00127	37.03%
3	13.65	21.87	1.60	1378.2	0.00060	0.00102	0.00127	19.48%
Average	13.65	21.88	1.60	1368.4	0.00054	0.00091	0.01394	28.05%

Table 2.84. F-119, $\%RFP_{HC}$, Arizona Test Dust, 0.035 Grams, PR 1.1

Run #	P_{atm}	P_{OC}	PR	Toc	mdot	FP	FP_0	%RFP
	psia	psia	-	R	lb/s	lb $T^{0.5}$ / psia	lb $T^{0.5}$ / psia	
1	13.79	15.10	1.10	534.9	0.00028	0.00043	0.00051	14.88%
2	13.72	15.05	1.10	541.0	0.00031	0.00048	0.00051	5.56%
3	13.72	15.03	1.10	538.5	0.00031	0.00048	0.00051	6.21%
Average	13.74	15.06	1.10	538.1	0.00030	0.00046	0.00733	8.88%

Table 2.85. F-119, $\%RFP_{HC}$, Arizona Test Dust, 0.150 Grams, PR 1.2

Run #	P_{atm}	P_{OC}	PR	Toc	mdot	FP	FP_0	%RFP
	psia	psia	-	R	lb/s	lb $T^{0.5}$ / psia	lb $T^{0.5}$ / psia	
1	13.79	16.55	1.20	548.0	0.00042	0.00060	0.00069	13.06%
2	13.79	16.57	1.20	538.1	0.00039	0.00054	0.00069	21.51%
3	13.79	16.55	1.20	534.2	0.00041	0.00058	0.00069	16.19%
Average	13.79	16.56	1.20	540.1	0.00041	0.00057	0.01006	16.92%

Table 2.86. F-119, $\%RFP_{HC}$, Arizona Test Dust, 0.300 Grams, PR 1.3

Run #	P_{atm}	P_{OC}	PR	Toc	mdot	FP	FP_0	%RFP
	psia	psia	-	R	lb/s	lb $T^{0.5}$ / psia	lb $T^{0.5}$ / psia	
1	13.79	17.92	1.30	539.9	0.00054	0.00070	0.00086	17.92%
2	13.79	17.86	1.30	535.8	0.00053	0.00068	0.00085	19.44%
3	13.79	17.86	1.29	553.6	0.00047	0.00062	0.00085	26.90%
Average	13.79	17.88	1.30	543.1	0.00051	0.00067	0.01165	21.42%

Table 2.87. F-119, $\%RFP_{HC}$, Arizona Test Dust, 0.410 Grams, PR 1.4

Run #	P_{atm}	P_{OC}	PR	Toc	mdot	FP	FP_0	%RFP
	psia	psia	-	R	lb/s	lb $T^{0.5}$ / psia	lb $T^{0.5}$ / psia	
1	13.79	19.25	1.40	537.6	0.00058	0.00070	0.00102	31.46%
2	13.79	19.32	1.40	552.9	0.00065	0.00079	0.00103	23.04%
3	13.79	19.33	1.40	556.7	0.00064	0.00079	0.00103	23.30%
Average	13.79	19.30	1.40	549.1	0.00062	0.00076	0.01268	25.93%

Table 2.88. F-119, $\%RFP_{HC}$, Arizona Test Dust, 0.425 Grams, PR 1.6

Run #	P_{atm}	P_{OC}	PR	Toc	mdot	FP	FP_0	%RFP
	psia	psia	-	R	lb/s	lb $T^{0.5}$ / psia	lb $T^{0.5}$ / psia	
1	13.65	21.86	1.60	539.4	0.00101	0.00107	0.00141	24.52%
2	13.65	21.84	1.60	534.7	0.00083	0.00088	0.00141	37.49%
3	13.65	21.83	1.60	536.7	0.00099	0.00105	0.00141	25.37%
Average	13.65	21.85	1.60	536.9	0.00094	0.00100	0.01393	29.13%

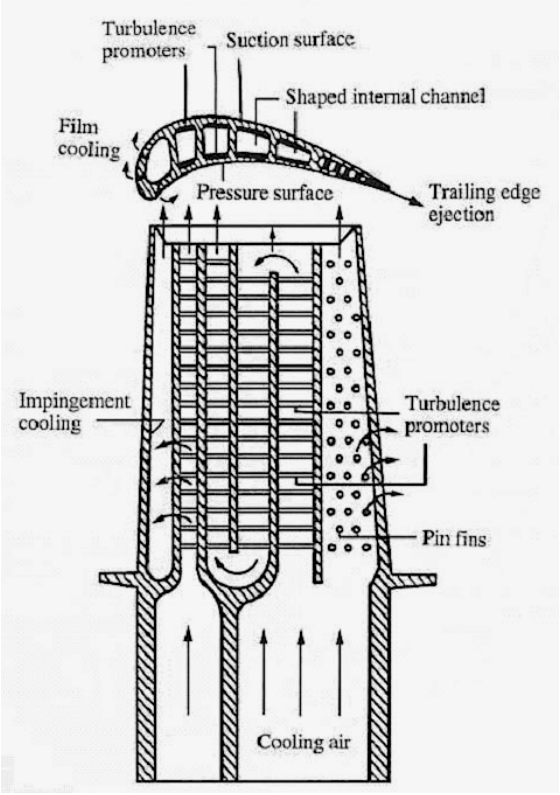

Figure 2.1. The typical turbine blade cooling scheme contains many complex cooling passages [Han et al, 1984].

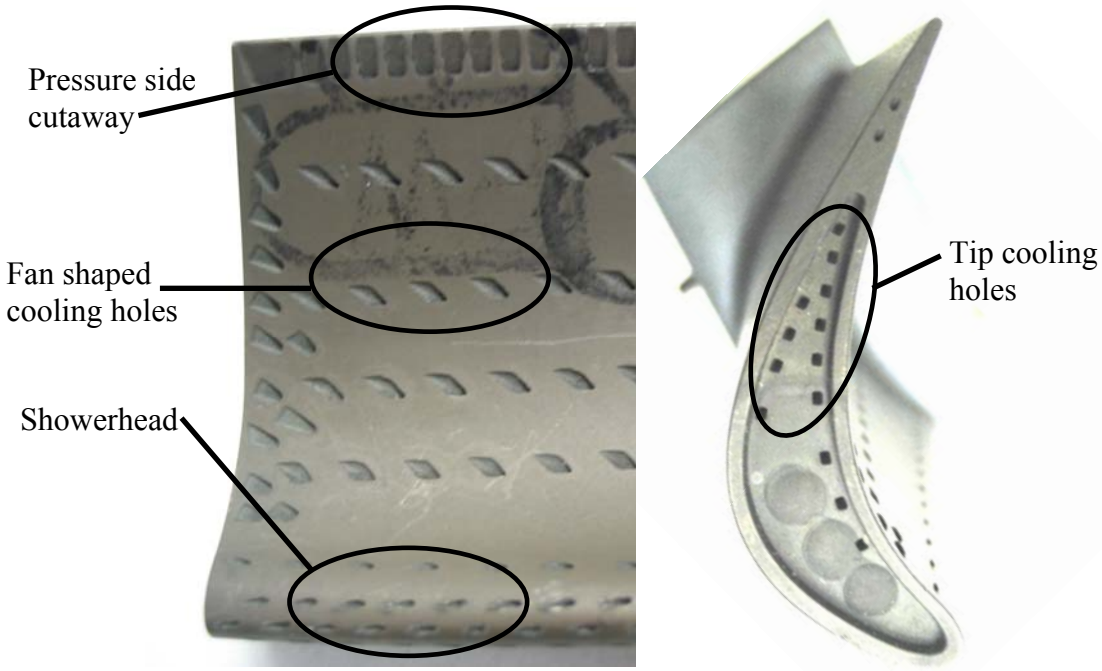

Figure 2.2. The film-cooling scheme of an F-100-229 first stage turbine blade contains many different features.

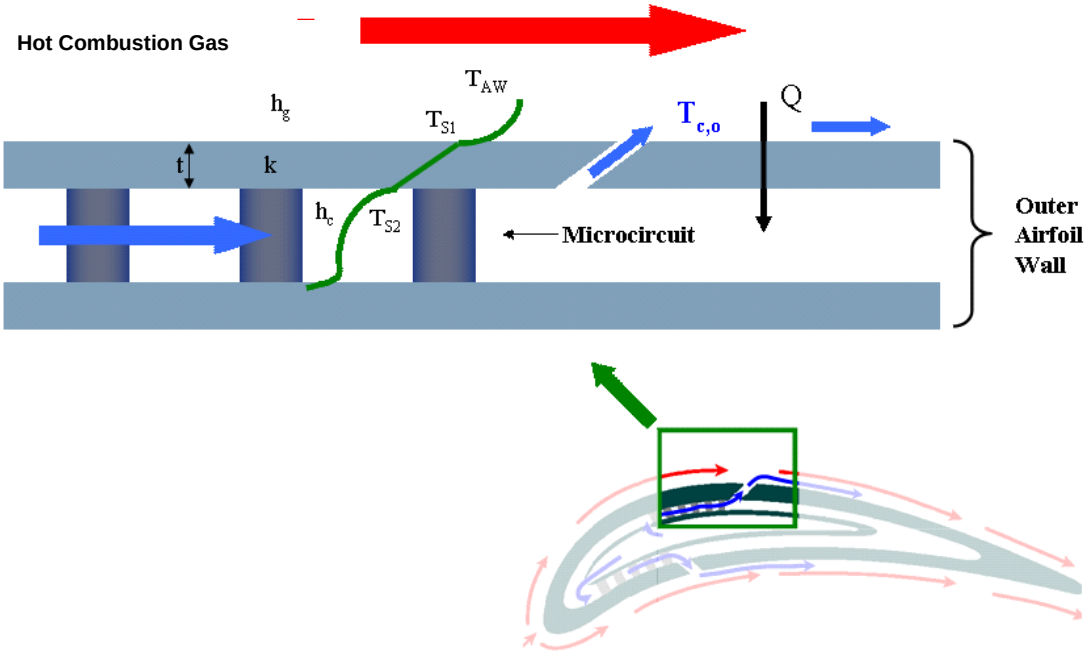

Figure 2.3. A microcircuit is constructed in the outer metal material, very close to the freestream. This causes the external metal temperature to be closer to the coolant temperature because of the lack of thermal resistance between the coolant and the freestream [Prausa, 2004].

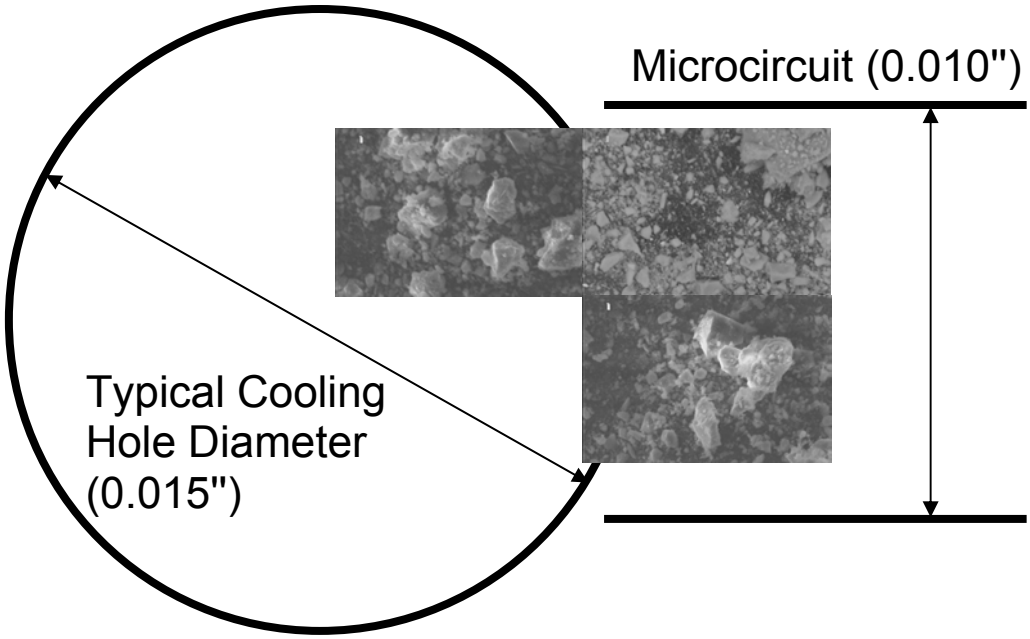

Figure 2.4. The size of the sand tested ranges from $4x10^{-6}$ inches to 0.010 inches, which is on the order of the hole size.

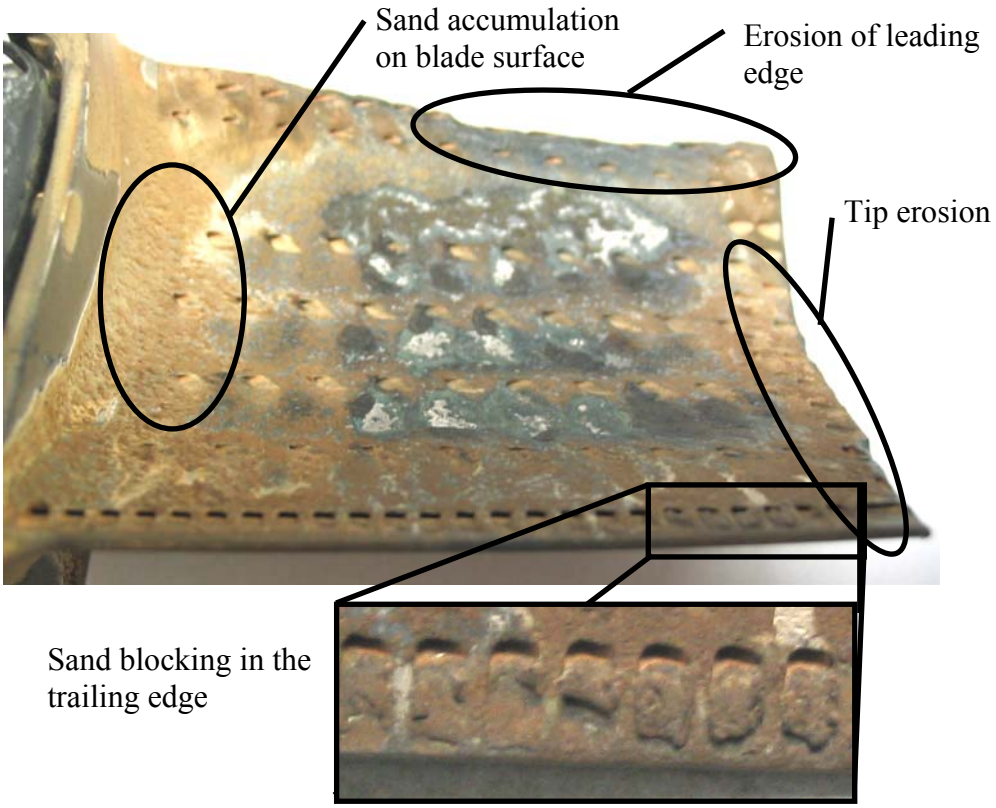

Figure 2.5. Sand ingestion can cause severe degradation of turbine blades by blocking film cooling holes (F-100-229).

Figure 2.6. Sand has accumulated and blocked cooling holes on a V2500 turbine blade.

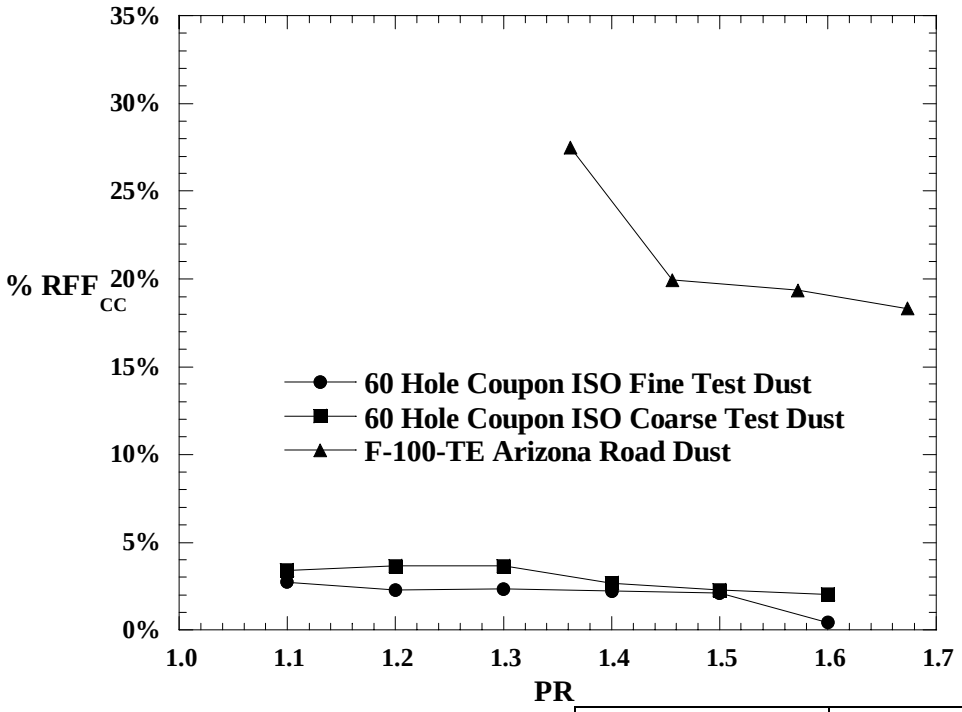

Figure 2.7. The same amount of sand causes more blockage in the F-100-TE than the coupon because of the internal features.

Part Tested	As shown
Temperature	Room Temperature
Sand Amount	0.5 grams

Figure 2.8. Turbine blades used in testing at Virginia Tech including, a) F-100-229-full field run blade, b) F-100-229-full new blade, c)F-100-229-TE field run blade, d) F-100-229-TE new blade, and e) F-119 microcircuit blade.

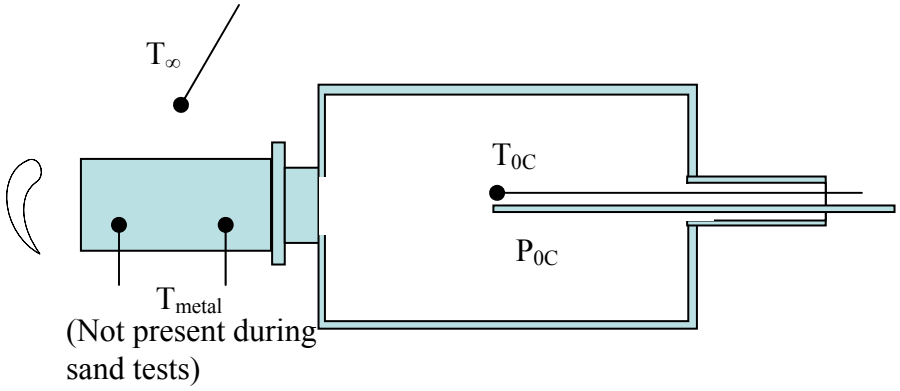

Figure 2.9. The thermocouple and static pressure tube were routed through the coolant air supply tube to protect them from the high kiln temperatures.

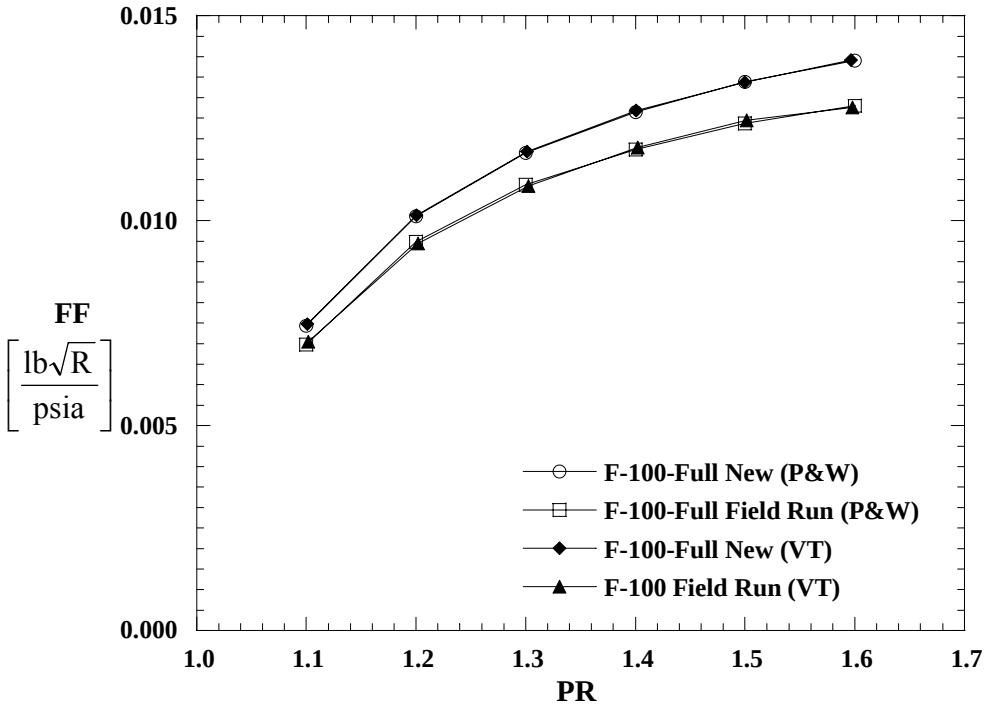

Figure 2.10. VT baseline flow parameters for the tested F-100-229-full new and field run parts are similar to the P&W values.

Part Tested	F-100-229-Full
Temperature	Cold
Sand Type/Amount	None

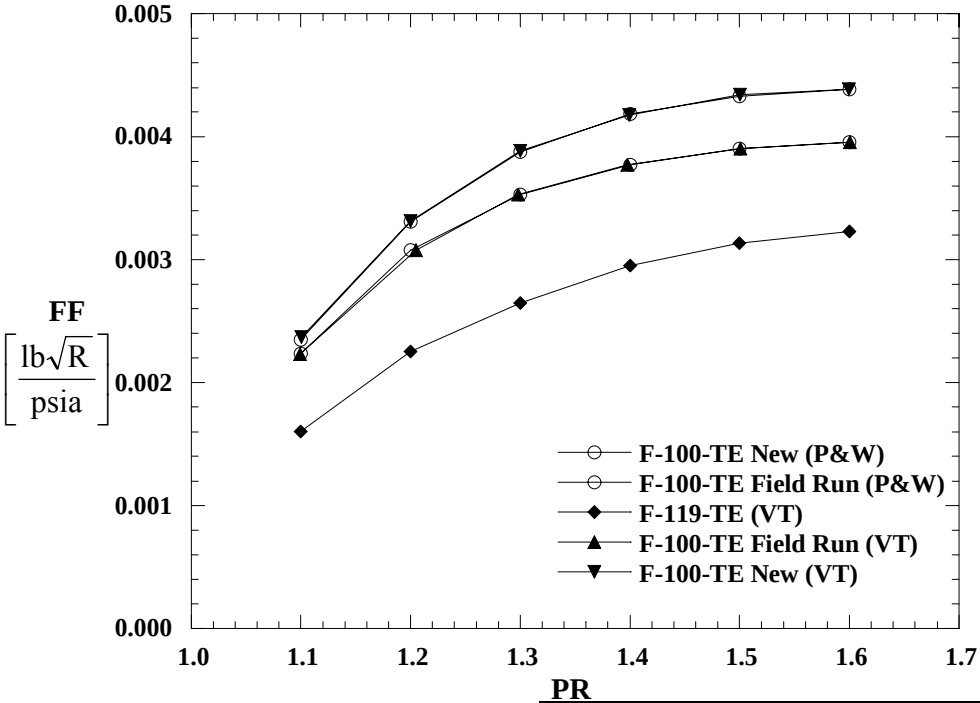

Figure 2.11. VT baseline flow parameters for the tested F-100-229-TE new and field run parts and the F-119 turbine blade.

Part Tested	Varies
Temperature	Cold
Sand Type/Amount	None

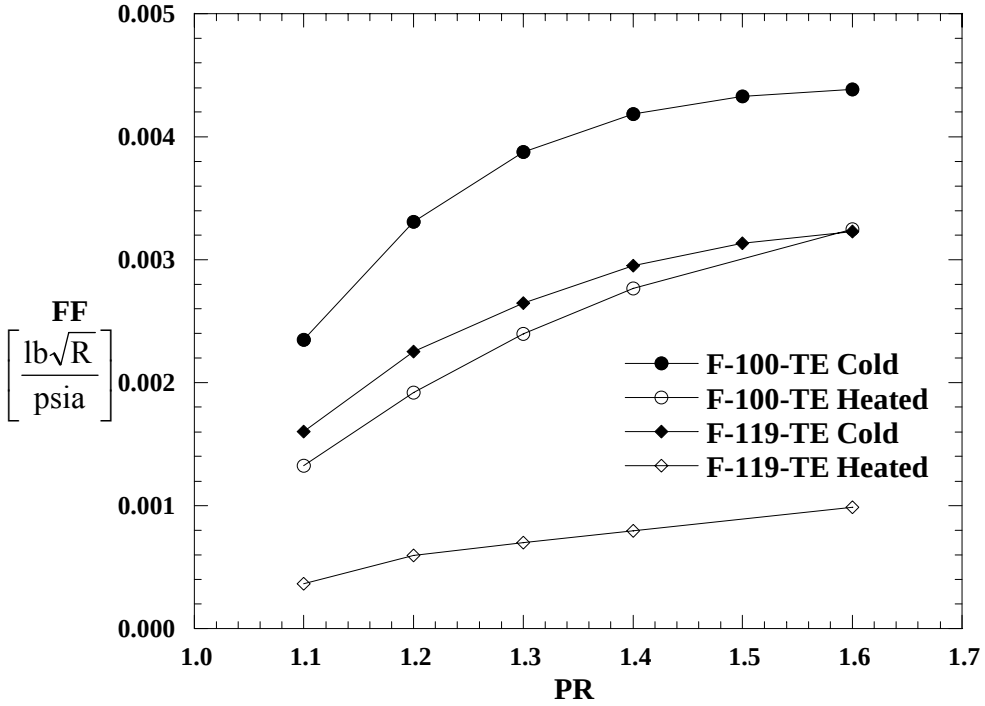

Figure 2.12. Flow parameter varies for heated tests on both the F-100-229-TE and the F-119 turbine blades.

Part Tested	Varies
Temperature	Table A5, A7
Sand Type/Amount	None

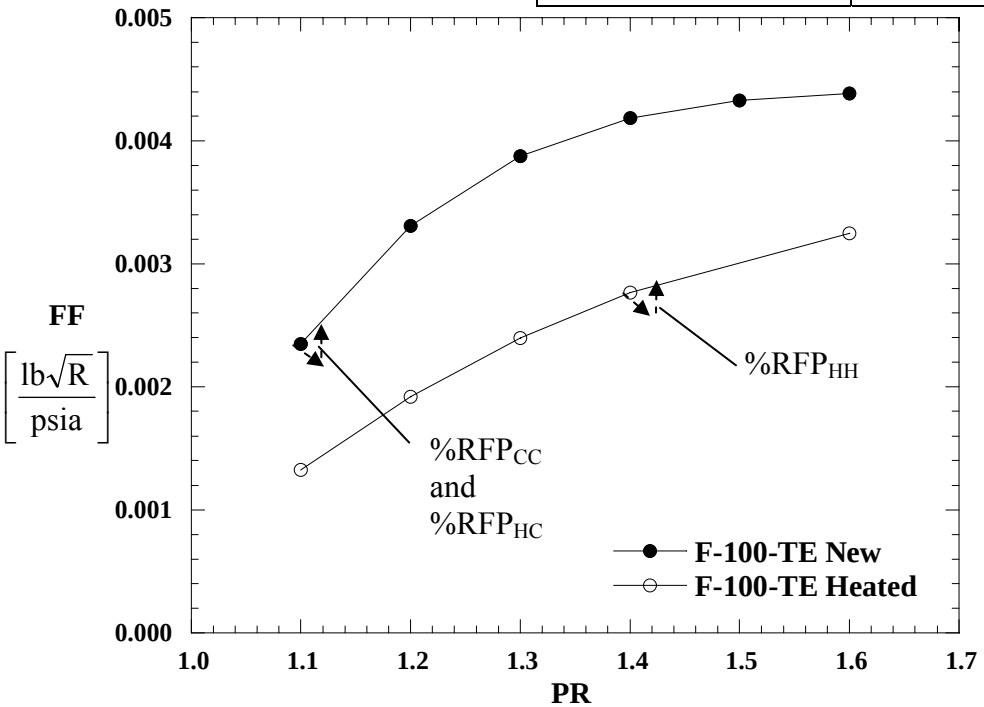

Figure 2.13. Flow parameters for cold and heated tests resulted in different flow parameters due to viscosity. This meant that there are two ways to measure %RFF for a heated test.

Part Tested	F-100-229-TE
Temperature	Cold and Heated (A5)
Sand Type/Amount	AZ road dust

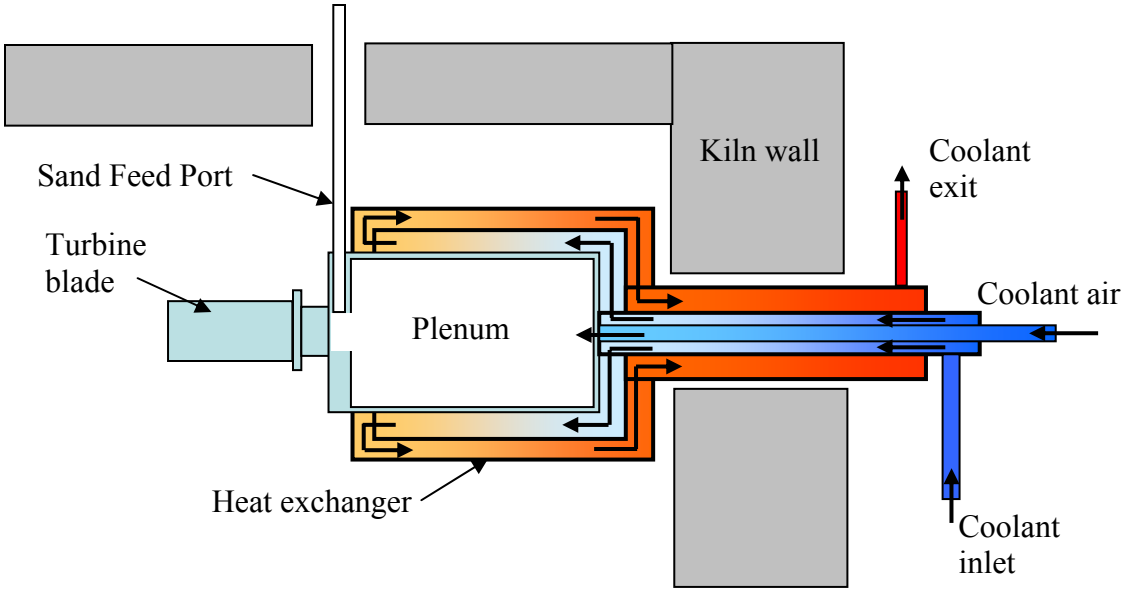

Figure 2.14. The heat exchanger maintains the coolant air within the required temperature range.

Figure 2.15. A ceramic kiln was used to simulate the metal and coolant temperatures reached in an actual turbine engine.

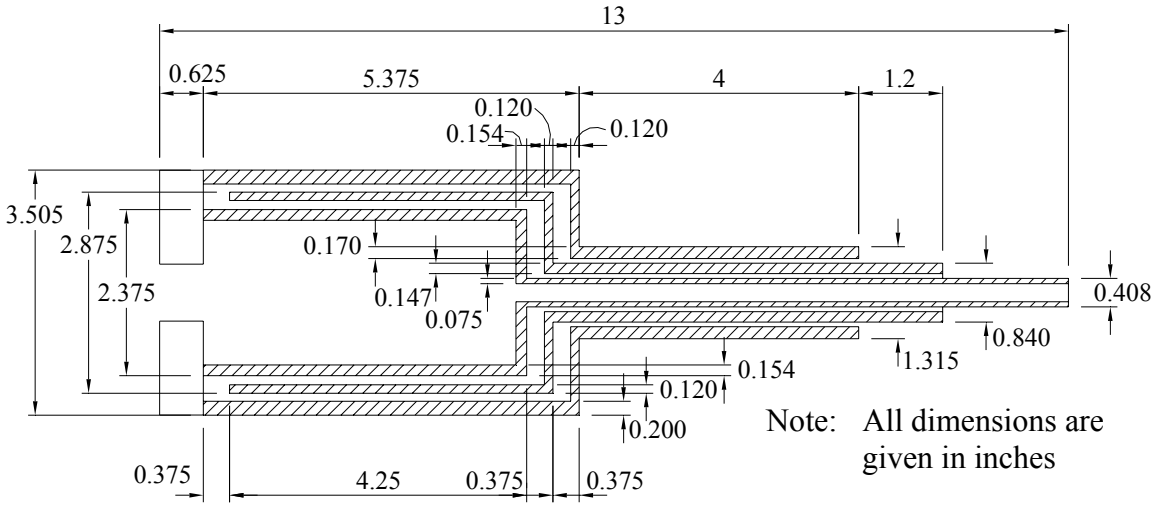

Figure 2.16. The dimensions for the heat exchanger were important so that the heat exchanger air would provide a fast moving protective sheath of air around the plenum.

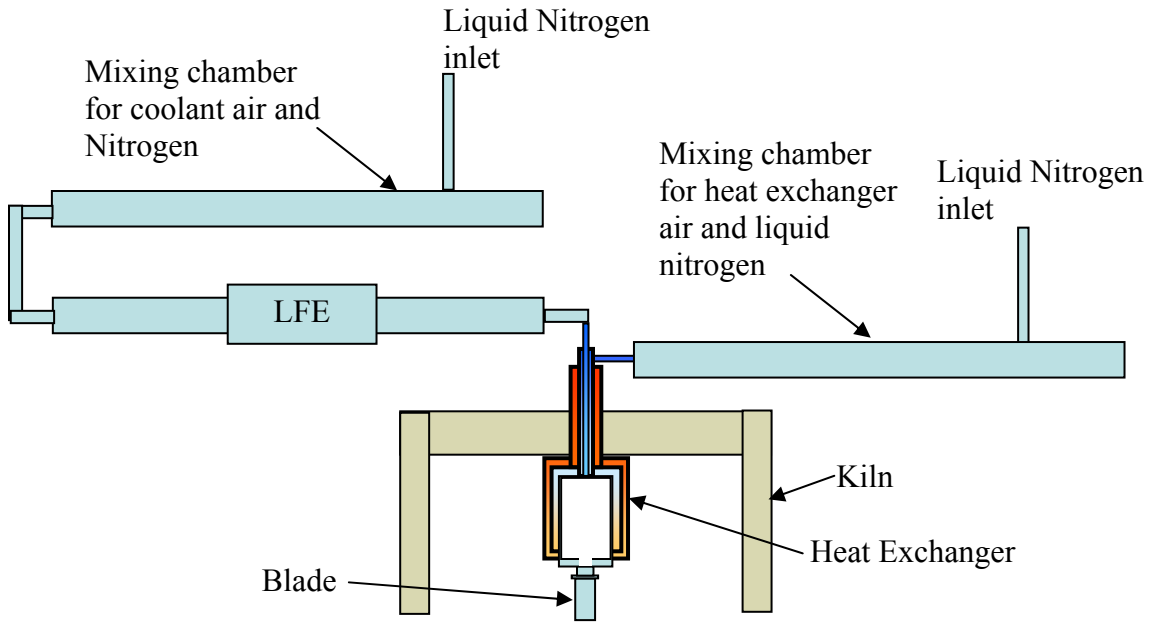

Figure 2.17. The heat exchanger system was modified so that liquid nitrogen could be used to further control the coolant temperature T_{0C}.

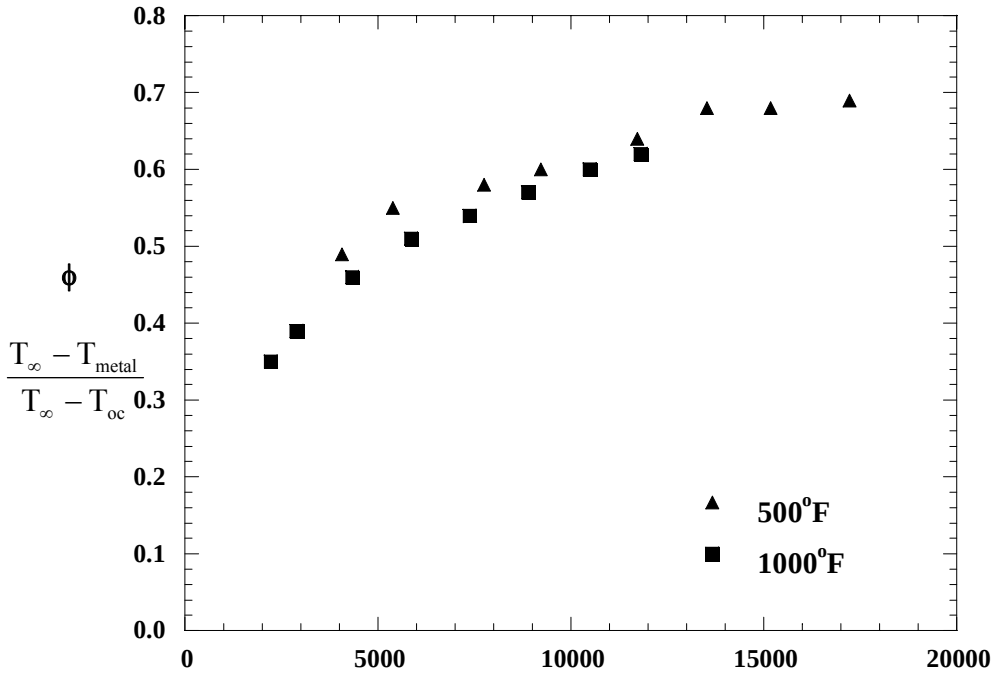

Figure 2.18. The effectiveness for the F-100-229-TE blade was determined to be a function of Reynolds number.

Part Tested	F-100-229-TE
Temperature	500°F, 1000°F
Sand Type/Amount	None

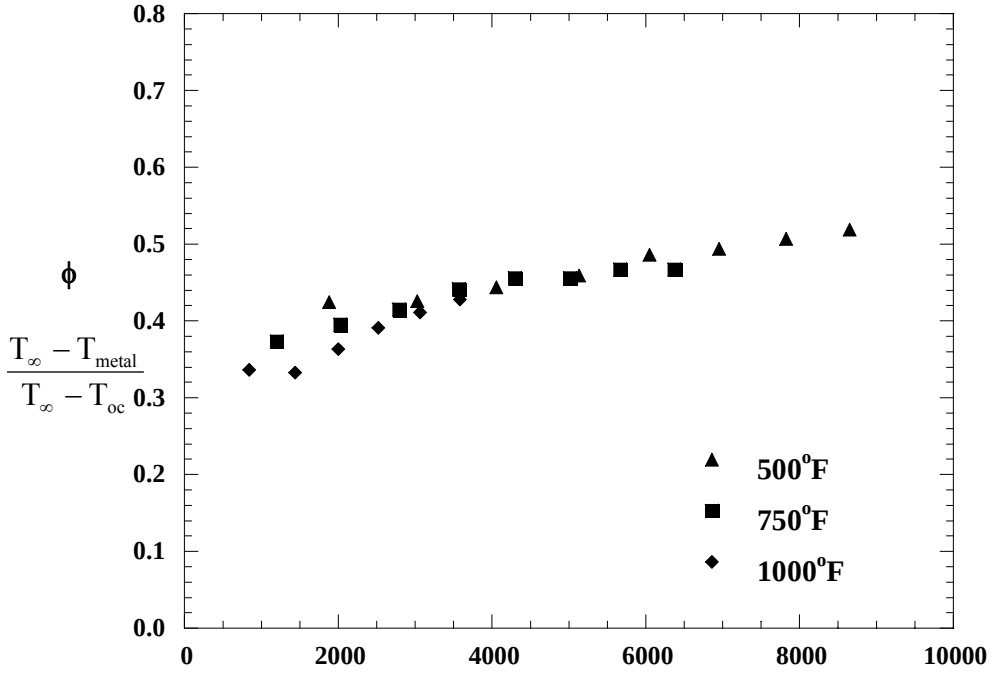

Figure 2.19. The effectiveness for the F-119 blade was determined to be a function of Reynolds number.

Part Tested	F-119
Temperature	500°F, 750°F 1000°F
Sand Type/Amount	None

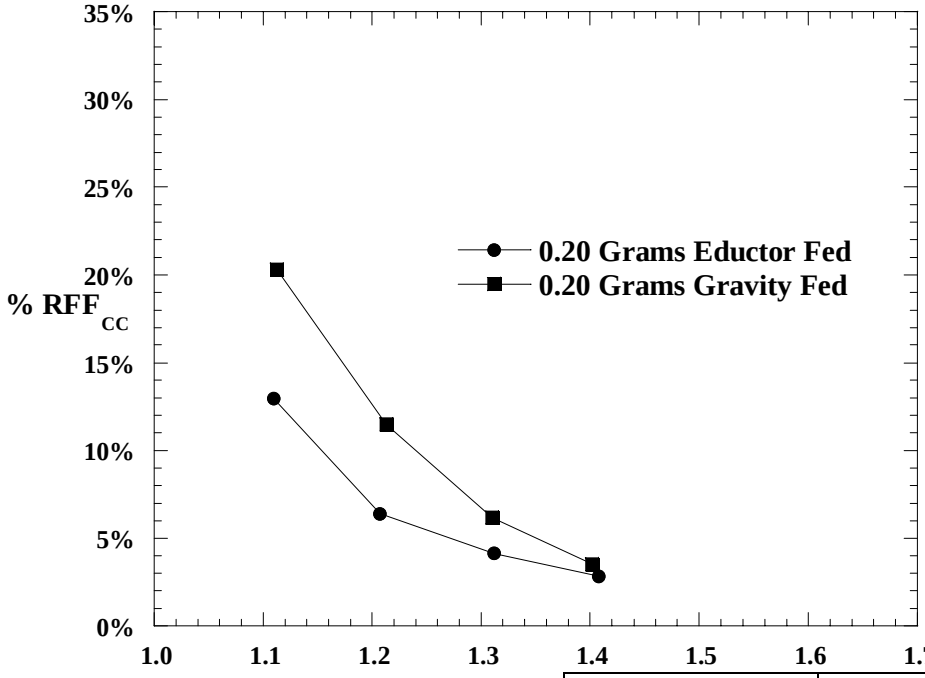

Part Tested	F-100-229-TE
Temperature	Cold
Sand Type/Amount	Arizona road dust, 0.20 grams

Figure 2.20. The method of sand introduction controls the sensitivity of the blade to sand ingestion.

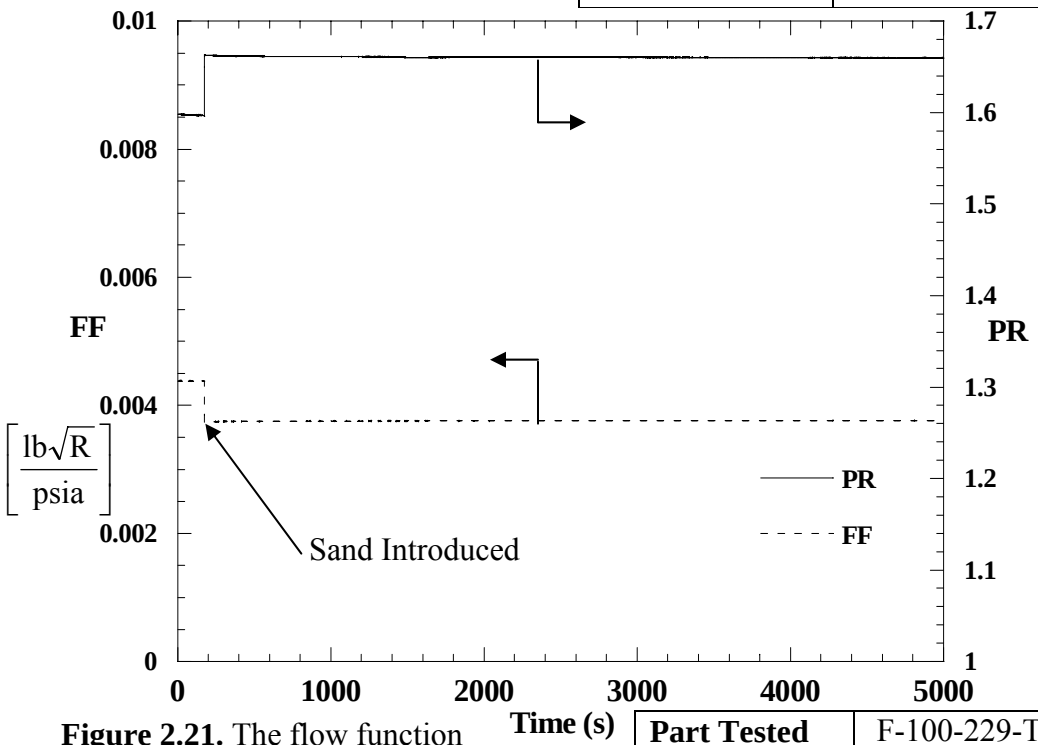

Part Tested	F-100-229-TE
PR / Temp	1.6, Cold
Sand Type/Amount	Arizona road dust, 0.50 grams

Figure 2.21. The flow function and pressure ratio stabilize a few seconds after sand is introduced in a cold test.

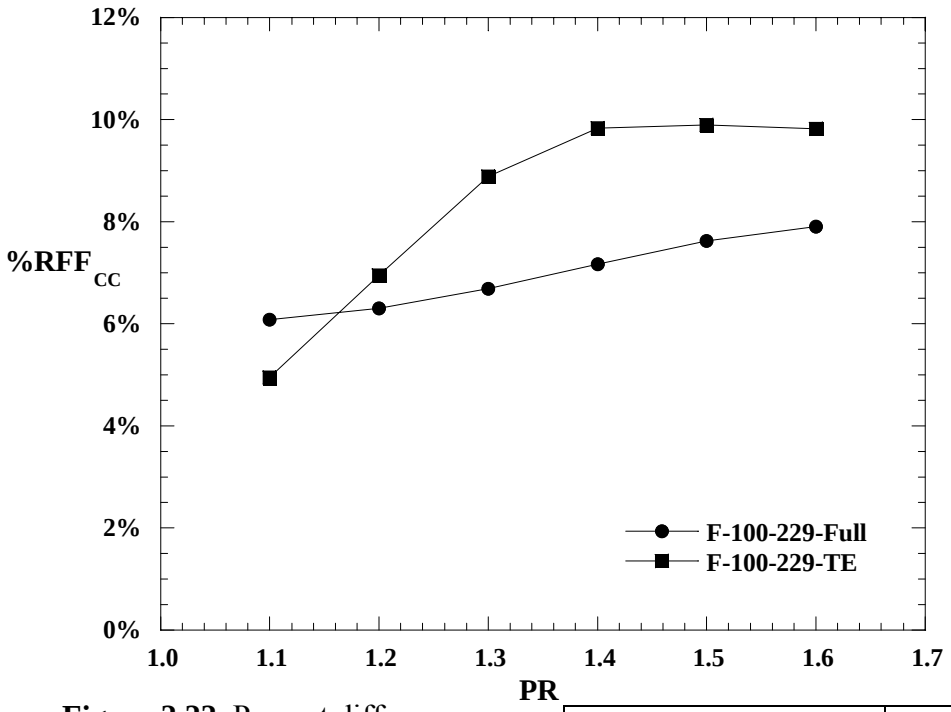

Figure 2.22. Percent differences in flow function between the new and field run turbine blades provided by Pratt and Whitney.

Part Tested	F-100-229-TE
Temperature	Cold
Sand Type/Amount	None

Undried Sand

Dried Sand

Figure 2.23. Drying the sand causes the mixture to be more uniform and reduces conglomerations.

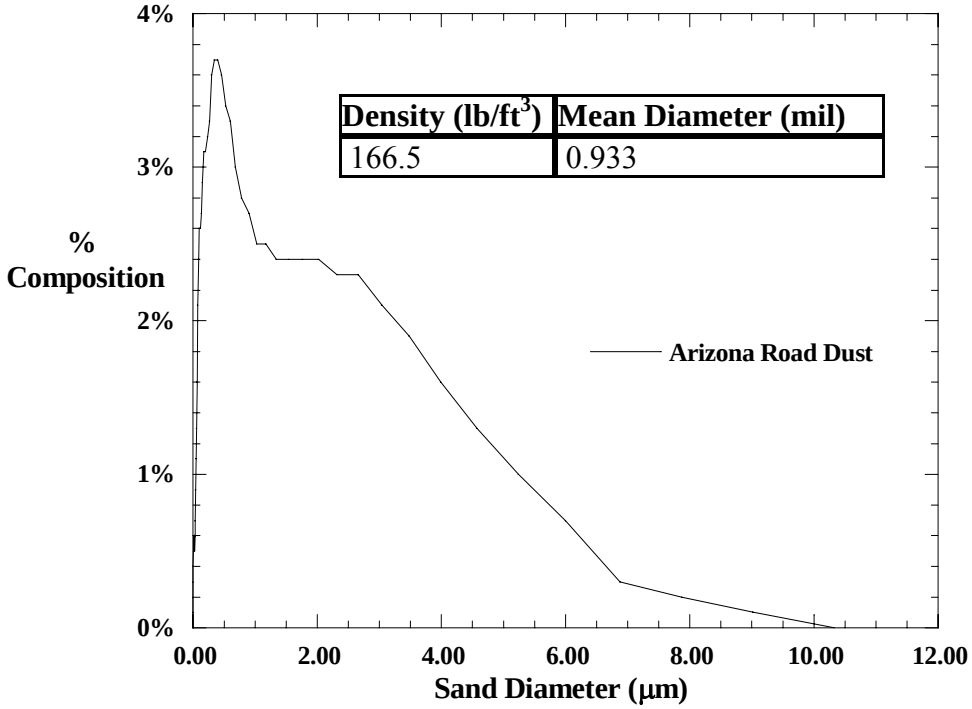

Figure 2.24. The size distribution of the Arizona road dust is similar to sand found in field run parts.

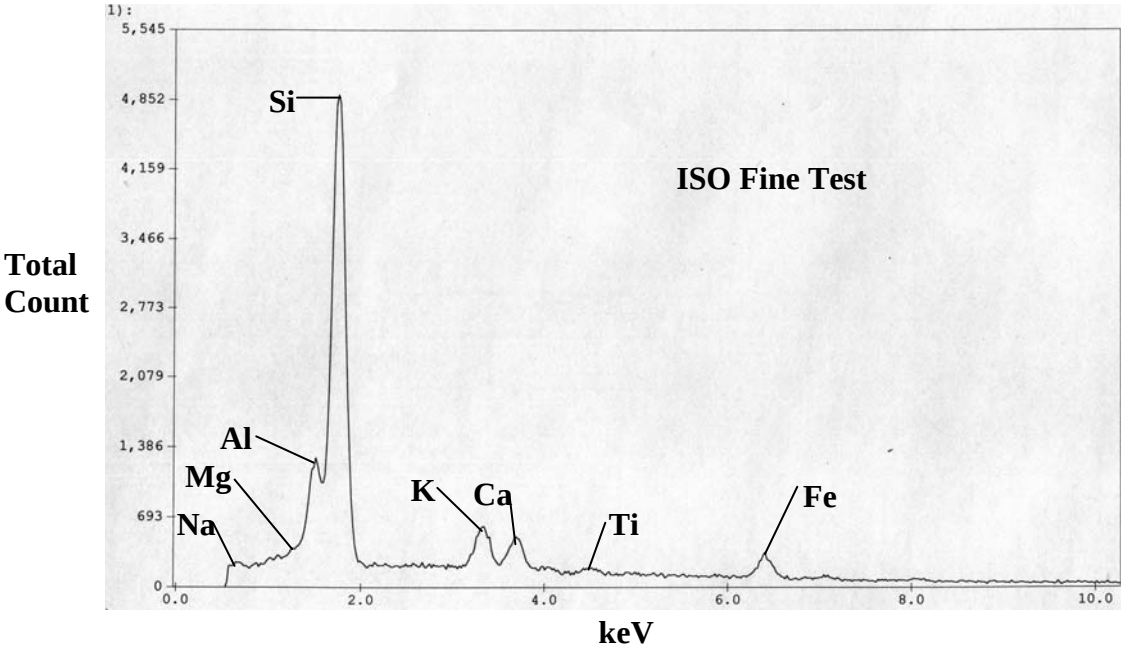

Figure 2.25. The molecular content of the test dusts indicates that the samples are crushed granite.

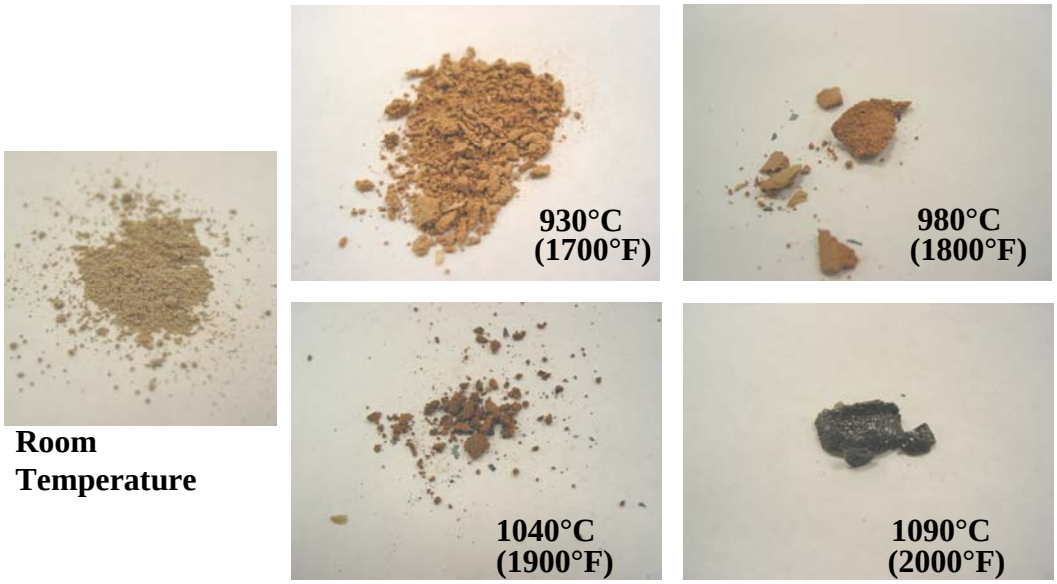

Figure 2.26. Arizona road dust melts at temperatures near the internal metal temperatures of the F-100-229 and F-119 turbine blades.

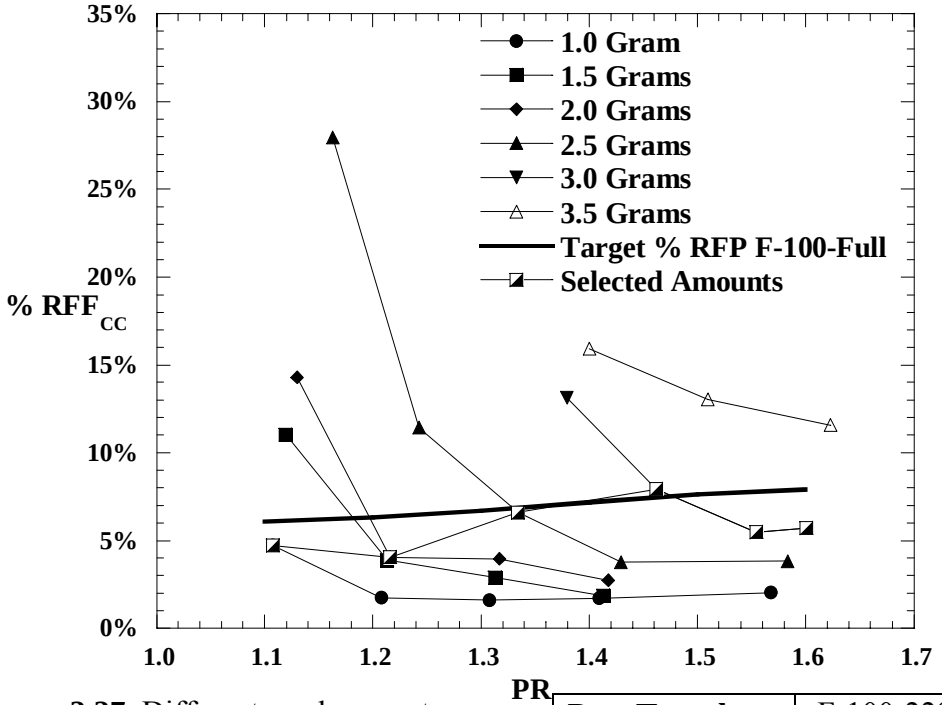

Figure 2.27. Different sand amounts were run at varying pressure ratios to approximate the $\%RFF_{CC}$ of the F-100-229-full field run blade.

Part Tested	F-100-229-full
Temperature	Cold
Sand Type	Arizona road dust

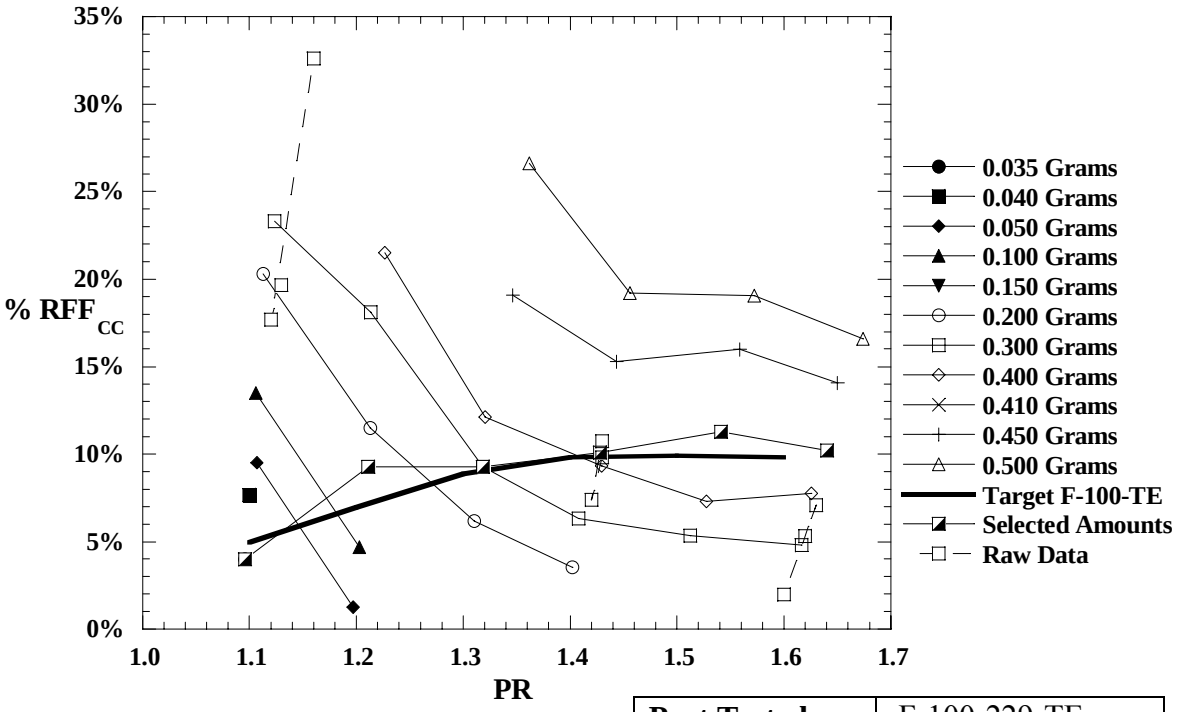

Figure 2.28. Many sand amounts were used to determine the correct amount needed to simulate the F-100-229-TE field run blade.

Part Tested	F-100-229-TE
Temperature	Room Temperature
Sand Type	Arizona road dust

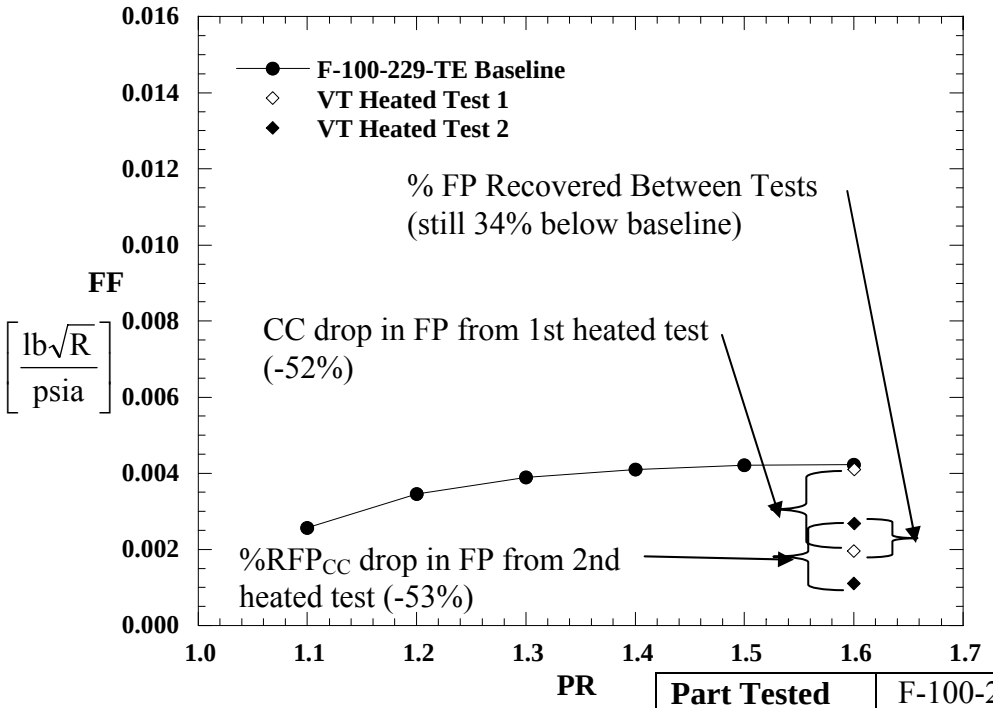

Figure 2.29. Sand blockage from the first and second F-100-229-TE was permanent because sand melted inside the blade during a heated test.

Part Tested	F-100-229-TE
Coolant Temp	1830°F
Metal Temp	1960°F
Sand Type/Amount	Arizona Road Dust, 0.425 grams

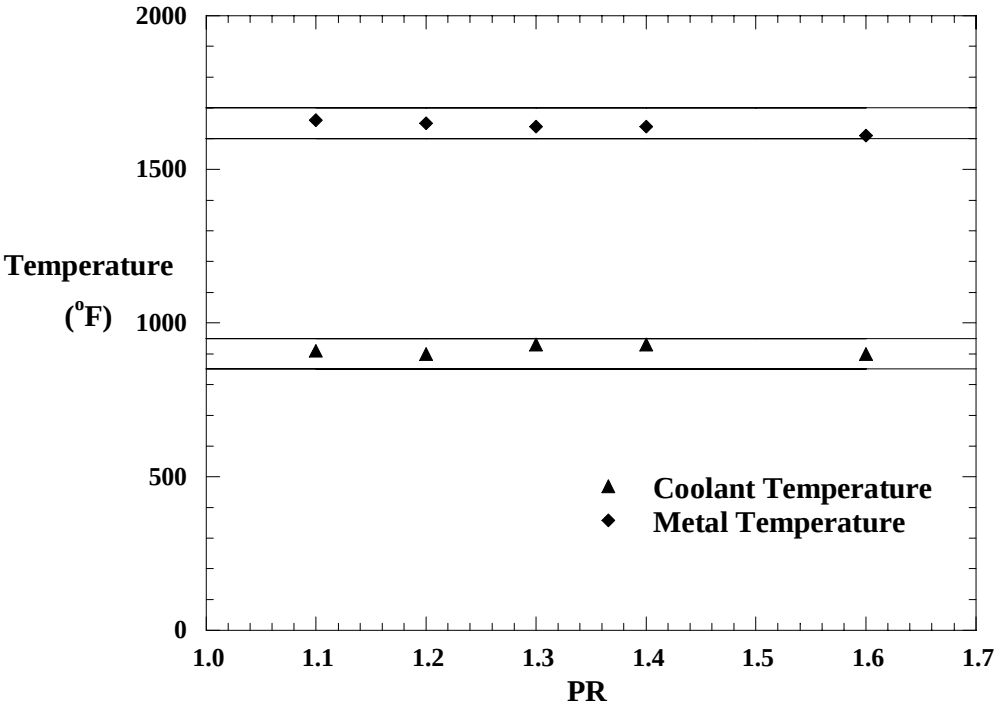

Figure 2.30. The F-100-229-TE metal and coolant temperatures were all within the limits provided by Pratt & Whitney for all pressure ratios (coolant 850-950°F, metal 1600-1700°F).

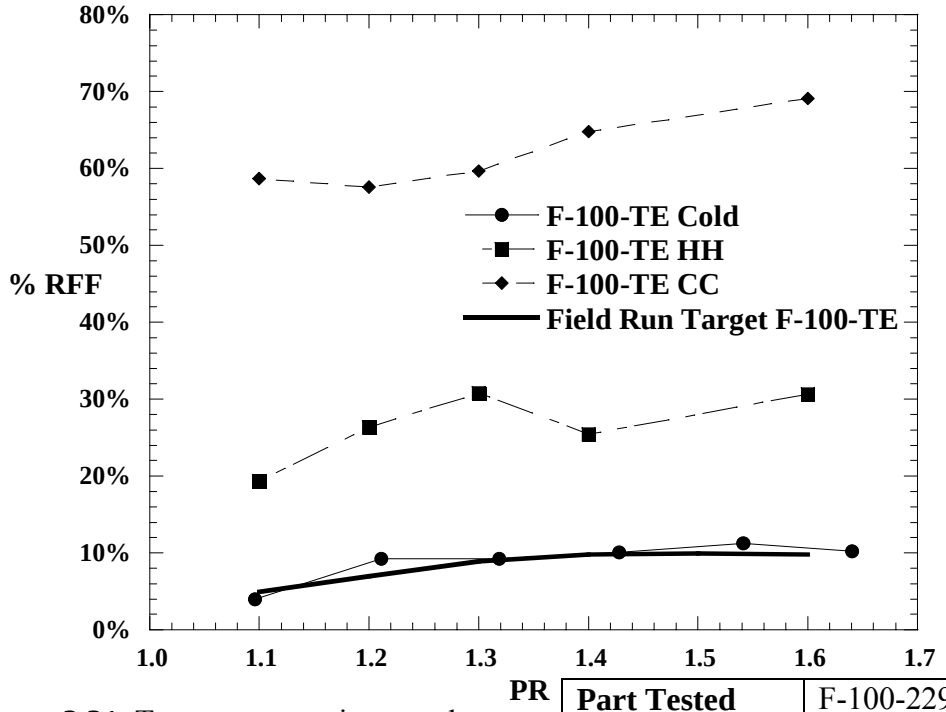

Figure 2.31. Tests run at engine metal temperatures caused a severe increase in %RFP compared to room temperature tests.

Part Tested	F-100-229-TE
Coolant Temp	Table A5
Metal Temp	Table A5
Sand Type	Arizona Road Dust

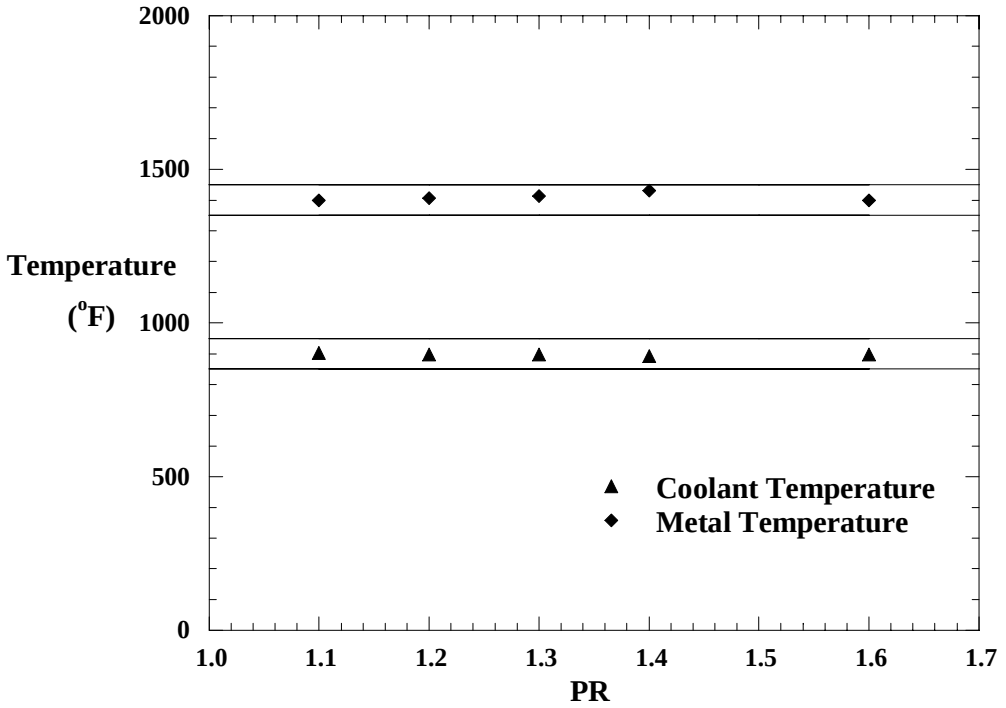

Figure 2.32. The F-119 metal and coolant temperatures were all within the limits provided by Pratt & Whitney for all pressure ratios (coolant 850-950°F, metal 1350-1450°F).

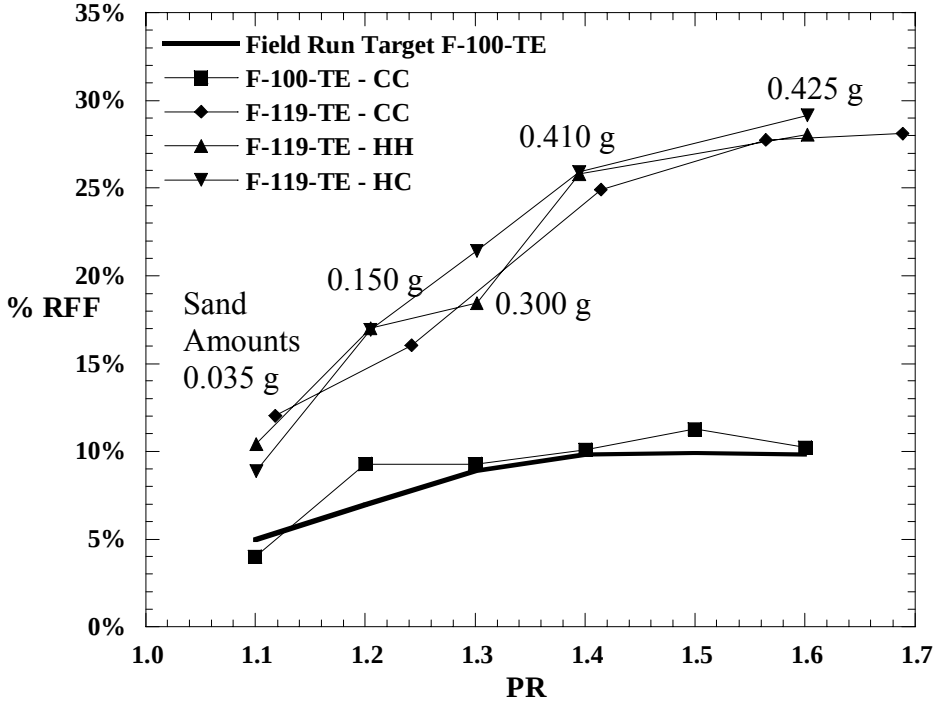

Figure 2.33. The heated tests run on the F-119 blade indicate similar blockage as seen at room temperature, indicating the lower metal temperatures did not cause sand melting.

Part Tested	F-119
Coolant Temp	Table A7
Metal Temp	Table A7
Sand Type	Arizona Road Dust